Cylinder Filling Control of Variable-Valve-Actuation equipped Internal Combustion Engines

Thomas Leroy

To cite this version:

Thomas Leroy. Cylinder Filling Control of Variable-Valve-Actuation equipped Internal Combustion Engines. Engineering Sciences [physics]. École Nationale Supérieure des Mines de Paris, 2010. English. NNT : 2010ENMP0005 . tel-00506471

HAL Id: tel-00506471
https://pastel.hal.science/tel-00506471

Submitted on 27 Jul 2010

HAL is a multi-disciplinary open access archive for the deposit and dissemination of scientific research documents, whether they are published or not. The documents may come from teaching and research institutions in France or abroad, or from public or private research centers.

L'archive ouverte pluridisciplinaire **HAL**, est destinée au dépôt et à la diffusion de documents scientifiques de niveau recherche, publiés ou non, émanant des établissements d'enseignement et de recherche français ou étrangers, des laboratoires publics ou privés.

Ecole doctorale n° 431 : ICMS - Information, Communication, Modélisation et Simulation

Doctorat ParisTech

THÈSE

pour obtenir le grade de docteur délivré par

l'École nationale supérieure des mines de Paris

Spécialité "Mathématique et Automatique "

présentée et soutenue publiquement par

Thomas LEROY

le 10 Mars 2010

Cylinder Filling Control of Variable-Valve-Actuation equipped Internal Combustion Engines

Directeur de thèse : **Nicolas PETIT**
Co-encadrement de la thèse : **Jonathan CHAUVIN**

Jury

M. Gregory SHAVER, Assistant Professor, School of Mechanical Engineering, Purdue University	Président
M. Lars ERIKSSON, Associate Professor, Dept. of Electrical Engineering, Linköping University	Rapporteur
M. Michel SORINE, Directeur de Recherche, INRIA	Rapporteur
M. Jonathan CHAUVIN, Ingénieur de recherche, IFP	Examinateur
M. Pascal MORIN, Chargé de recherche HDR, INRIA	Examinateur
M. Nicolas PETIT, Professeur, Centre Automatique et Systèmes, MINES ParisTech	Examinateur

THESE

MINES ParisTech
Unité Automatique et Systèmes
60 bd Saint Michel, 75272 Paris Cedex 06, France

MINES
ParisTech

ED n°431: ICMS - Information, Communication, Modélisation et Simulation

THESE

Pour obtenir le grade de
Docteur de l'Ecole nationale supérieure des Mines de Paris
Spécialité "Mathématiques et Automatique"

présentée et soutenue publiquement par
Thomas LEROY

le 10 Mars 2010

Contrôle du remplissage des Moteurs à Combustion Interne équipés de Systèmes de Distribution Variable

Directeur de Thèse: M. Nicolas PETIT

Jury

Président	M. Gregory SHAVER
Rapporteur	M. Lars ERIKSSON
Rapporteur	M. Michel SORINE
Examinateur	M. Jonathan CHAUVIN
Examinateur	M. Pascal MORIN
Examinateur	M. Nicolas PETIT

MINES
ParisTech

PhD THESIS

To obtain
the Doctor's degree from l'Ecole nationale supérieure des Mines de Paris
Speciality "Mathématiques et Automatique"

defended in public by
Thomas LEROY

the 10^{th} March, 2010

Cylinder Filling Control of Variable-Valve-Actuation equipped Internal Combustion Engines

Thesis Advisor: M. Nicolas PETIT

Committee

Chair	M. Gregory SHAVER
Referee	M. Lars ERIKSSON
Referee	M. Michel SORINE
Examiner	M. Jonathan CHAUVIN
Examiner	M. Nicolas PETIT
Examiner	M. Nicolas PETIT

Thomas LEROY

Centre Automatique et Systèmes, Unité Mathématiques et Systèmes, MINES ParisTech, 60 bd St Michel 75272 Paris Cedex 06, France.

IFP, 1&4 av. du Bois Préau, 92852 Rueil-Malmaison, France.

E-mail: thomas.leroy@{ifp.fr, mines-paristech.fr}

Key words. - Internal combustion engine, Variable Valve Actuation, Engine control, Cylinder filling, Dynamical coordination
Mots clés. - Moteur à combustion interne, Distribution variable, Contrôle moteur, Remplissage, Coordination dynamique

---

July 6, 2010

REMERCIEMENTS

En tout premier lieu, mes remerciements s'adressent à mon directeur de thèse, Nicolas Petit, ainsi qu'à mon responsable au sein de l'IFP, Jonathan Chauvin. Je remercie infiniment Nicolas pour tout ce qu'il m'a transmis, pour les discussions parfois sans fin que l'on a pu avoir ainsi que pour son enthousiasme à tout épreuve. Je suis également très reconnaissant envers Jonathan pour la confiance qu'il m'a toujours accordée, pour la motivation qu'il a su me transmettre même dans les moments où le doute était le plus fort ainsi que pour sa disponibilité.

Je remercie également Gilles Corde, chef du département Automatique, Traitement du signal et Informatique temps réel à l'IFP où j'ai passé ces trois ans, pour m'avoir proposé cette thèse et pour l'avoir suivie avec tant d'attention.

Je souhaite remercier Lars Eriksson ainsi que Michel Sorine qui ont accepté d'être les rapporteurs de cette thèse. Je remercie également Messieurs Gregory Shaver et Pascal Morin qui m'ont fait l'honneur de participer au Jury de soutenance.

Je remercie tout particulièrement Mathieu, Riccardo, Emmanuel, Thomas et Grégory, collègues doctorants à l'IFP, grâce à qui l'ambiance de travail était très agréable.

Je tiens à remercier toutes les personnes de l'IFP avec lesquelles j'ai travaillé pendant ces années : Philippe, Guénaël, Olivier, Fabrice G., Alexandre, Jérémy, Frédéric, Ghizlane, Gianluca, Carole, Hérald, Fabrice L.B., Pierre, Louis-Marie, Régis, David. Merci pour les agréables moments passés à l'étranger lors des conférences.

Je remercie également les Professeurs Pierre Rouchon, Philippe Martin, Laurent Praly et Jean Lévine que j'ai côtoyés lors de mes passages au CAS. Merci aux personnes avec qui j'ai passé de bons moments aux Mines : Erwan, Pierre-Jean, Florent, Eric, Caroline et Paul.

Enfin, j'ai une pensée pour toute ma famille et pour Delphine en particulier.

Cylinder Filling Control of Variable-Valve-Actuation equipped Internal Combustion Engines

RESUME

Nous étudions la production de couple et de polluants de moteurs à combustion interne à distribution variable d'un type fréquemment répandu dans l'industrie automobile (moteurs Diesel ou essence). Les systèmes de distribution variable (VVA pour Variable Valve Actuation) ont été introduits dans les moteurs pour optimiser l'efficacité du fonctionnement global sur des plages très larges de points de fonctionnement, considérés à l'équilibre.

A tout instant, les résultats de la combustion dépendent du remplissage en air/gaz brûlés du cylindre, qui lui même dépend de la position des actionneurs VVA et des conditions dans le collecteur d'admission. Ces deux sous-systèmes ont des temps de réponse différents, ce qui conduit, pendant les transitoires, à des pertes d'efficacité du moteur. Dans cette thèse, nous proposons une solution a ce problème, qui prend la forme de boucle de coordination entre les sous-systèmes de contrôle de bas-niveau. Cette coordination s'effectue par l'intermédiaire d'un modèle de remplissage développé dans ce manuscrit. Des résultats expérimentaux établissent qu'il est possible d'améliorer la production de couple et de réduire les polluants.

ABSTRACT

The production of torque and pollutants of Variable Valve Actuation equipped internal combustion engines found in the automotive industry (both Diesel and gasoline engines) is studied. Variable Valve Actuation (VVA) is a technology which has been introduced to optimize engine efficiency at steady-states covering a wide range of operating conditions.

In more details, the outcome of the internal combustion engine (torque and pollutant) depends on the cylinder filling at each stroke which, itself, depends on the VVA positions and the engine intake manifold conditions. These two subsystems have inconsistent response times which results in efficiency losses during transient operations. In this manuscript, a remedy for this issue which takes the form of coordination loops of low-level controllers is proposed. This coordination uses a cylinder filling model, designed in the thesis. Experimental results prove that torque production and pollutant emissions can be improved.

Contents

Introduction xix

Acronyms, notation and mathematical definitions xxiii

1 A description of cylinder filling control issues for Variable-Valve-Actuation internal combustion engines 1

1.1 Background on internal combustion engines 1

1.1.1 Engine four-stroke operating cycle 1

1.1.2 Around the combustion chamber 3

1.1.3 Variable Valve Actuation technologies 3

1.2 Background on VVT equipped SI engines 4

1.2.1 SI engine generalities: the air and fuel inflows 5

1.2.2 Ways to lower consumption: downsizing, turbocharging and pumping losses 5

1.2.3 Impact of VVT actuators on the engine 7

1.2.4 Existing controllers for SI engines 9

1.2.5 Issues during transients 10

1.3 Background on VLD equipped CI engines 12

1.3.1 CI engine generalities: the air and fuel inflows 12

1.3.2 Towards lower emissions using EGR 13

1.3.3 Impact of VLD on the engine: benefits of the internal gas recirculation 13

1.3.4 Existing controllers for CI engines 15

1.3.5 Issues during transients 15

1.4 The proposed coordination solution 17

2 Cylinder filling model of internal combustion engines 19

2.1 General analytic cylinder filling model 22

2.1.1 In-cylinder total mass at intake valve closing 23

2.1.2 Aspirated mass coming from the exhaust 23
2.1.3 Aspirated mass through the intake valve 26
2.2 Cylinder filling model for turbocharged VVT SI engines 27
2.2.1 High frequency analysis 28
2.2.2 Aspirated masses mean-value model 28
2.2.3 Experimental data 32
2.2.4 Model calibration 32
2.2.5 Comparisons with experimental data 34
2.3 Cylinder filling model for VLD CI engines 35
2.3.1 High frequency analysis 36
2.3.2 Aspirated masses mean-value model 36
2.3.3 Experimental data 39
2.3.4 Model calibration 39
2.3.5 Comparisons with experimental data 40
2.4 Conclusion 41

3 Case study 1: VVT turbocharged SI engines control 43
3.1 Model properties 45
3.1.1 Intake manifold pressure and VVT dynamics 46
3.1.2 Breathing model 48
3.1.3 Breathing model properties 48
3.2 Proposed control strategy 50
3.2.1 Coordination strategy 51
3.2.2 Block structure 53
3.2.3 Stability analysis 54
3.2.4 Practical usage of the stability analysis 57
3.3 Experimental results 58
3.3.1 Experimental setup 59
3.3.2 Low and part load 59
3.3.3 High load 61
3.4 Conclusion on the obtained results 64

4 Case study 2: VLD Diesel engines control 65
4.1 System modeling 66
4.1.1 Aspirated masses model 67
4.1.2 In-cylinder composition and temperature model 67
4.1.3 Model summary 71

4.1.4 Control-oriented rewriting of the model 71
4.2 Proposed control strategy 74
4.2.1 In-cylinder set points 74
4.2.2 Coordination strategy 75
4.2.3 Block structure 76
4.2.4 Stability analysis 76
4.3 Experimental results 83
4.3.1 Engine setup 84
4.3.2 Intake manifold BGR variation 84
4.3.3 Torque transients 86
4.3.4 ECE driving cycle 89
4.4 Conclusion on the obtained results 91

5 Conclusions and perspectives **93**
5.1 Main contributions 93
5.2 Perspectives 95

A Intake manifold pressure controller for SI engines **97**
A.1 Introduction 97
A.2 System modeling 98
A.2.1 Balance in the intake manifold 98
A.2.2 State space model and physical assumptions 100
A.3 Reference trajectory 101
A.4 Trajectory-tracking strategy 101
A.4.1 Open-loop control when the bias is known 101
A.4.2 Closed-loop control in the case of unknown bias 102
A.5 Experimental tip-in on test bench 104
A.5.1 Implementation 104
A.5.2 Torque transients at test bench 104
A.5.3 Torque transient on vehicle 105
A.6 Conclusion 107

B Usage of a mass air flow sensor **109**
B.1 Introduction 109
B.2 System modeling 109
B.2.1 Balance in the intake manifold 109
B.2.2 State space model and physical assumptions 110
B.3 Reference trajectory 110

B.4 Trajectory-tracking strategy . . . 111
  B.4.1 Observer design . . . 111
  B.4.2 Closed loop control law . . . 113
  B.4.3 Convergence proof of the observer-controller . . . 113
  B.4.4 Conclusion on air mass control . . . 118
B.5 Experimental tip-in on test bench . . . 118
  B.5.1 Implementation . . . 118
  B.5.2 Torque transients . . . 118
B.6 Conclusion . . . 119

C Air/Fuel Ratio controller for SI engines **123**
C.1 Introduction . . . 123
C.2 Existing control strategy . . . 123
C.3 Proposed alternative control strategy . . . 124
C.4 Experimental results . . . 125
  C.4.1 Test bench results . . . 125
  C.4.2 Vehicle results . . . 126
C.5 Conclusion . . . 127

D Static positioning of the VVA actuators **129**
D.1 Static positioning of the VVT actuators . . . 129
D.2 Static positioning of the VLD actuator . . . 130

E Publications **131**
E.1 Conference papers . . . 131
E.2 Journal contributions . . . 132
E.3 Patent . . . 132

Bibliography **133**

Introduction

The systems under consideration in this thesis are Variable Valve Actuation (VVA)-equipped internal combustion engines. Such systems are becoming more common in the automotive industry. The topic addressed here is the control of cylinder filling. Two technologies of VVA are considered: Variable Valve Timing (VVT) and Variable Lift and Duration (VLD).

Classically, the aim is to control the production of torque, while limiting pollutant emissions and fuel consumption resulting from the combustion. At each stroke, these outputs are directly determined by the properties of the blend of fuel, fresh air, and burned gases present in the cylinder prior to combustion.

In modern automotive engines, cylinders are filled by the so-called *air path* and *fuel path* subsystems. Depending on the employed technologies, these subsystems consist of the turbocharger, exhaust gas recirculation loop(s), intake manifold, and, on the other hand, the injectors. Different implementations of VVA are also becoming more common. VVA generally permits the control of the inlet and exhaust gas flows into and out of the cylinders.

In practice, cylinder filling is usually managed by embedded controllers using extensive look-up tables covering every possible engine working point. These tables act as inputs to the controllers of the air path (including the VVA) and fuel path subsystems. An important limitation of this approach is that, implicitly, the engine is considered to operate at a *steady point*. Indeed, look-up tables generally contain only data obtained at steady-state. Yet, engines are mostly used in transient modes, as most driving conditions require frequent gear shifts and torque variations to satisfy a constantly changing load (this point is also apparent in standardized testing cycles).

During these transients, cylinder filling is frequently sub-optimal. Cylinder filling depends on the following variables: the cylinder-peripheral conditions (pressure, temperature, composition), the VVA positions and engine speed. These variables each have *their own response times*, determined by both their respective controllers. The primary culprit for the sub-optimal cylinder filling during transients is the dispersion of response times for these variables.

This problem has has a solution: cylinder filling can be improved to a large extent during transients via a methodology presented in this thesis. First, a particular control objective is formulated (depending on the case under consideration, this can be an in-cylinder gas mass or composition). Then, an analytic model is established for this variable involving the cylinder-peripheral conditions and the VVA positions, representing the control variables. From this model, a strategy is deduced to compensate the sluggishness of one of the control variables via modulation of one of the others. This results in a coordination of existing low-level controllers and leads to an improvement of the high-level objective transient control.

The thesis is organized as follows. Background information on the functioning of internal combustion engines equipped with VVA are presented in Chapter 1. The cylinder filling phenomena is focused on. The two cases under consideration in this thesis are detailed: Spark ignition (SI) engines and Compression Ignition (CI). After commenting on the beneficial effects of VVA technologies during steady state operation, the shortcomings of state-of-the-art controllers during transients are described. In each case control problems are formulated for the transient control of cylinder filling. The focus is on torque production and pollutant emissions. Briefly, coordination strategies are sketched to solve each of the formulated control problems. To determine effective generalizable coordination formulas, a cylinder filling model is needed. Such a quantitative model is proposed in Chapter 2. It is developed using first principles equations for the aspirated gas masses. These analytic equations include cylinder-peripheral thermodynamic conditions, and the intake and exhaust valve lift histories. Following a general formulation of the breathing phenomenon, the two particular cases of SI engine (equipped with VVT generating *back-flow* and *scavenging*) and CI engine (equipped with VLD allowing a second exhaust valve re-opening generating exhaust re-induction) are detailed. The models are calibrated using experimental data obtained at test benches. The subsequent two chapters report case-studies. In Chapter 3, a VVT equipped, turbocharged SI engine is considered. Here, the control strategy is to coordinate the VVT and the intake manifold pressure, which can be, depending on the operating point, actuated by the throttle or the turbocharger. After a discussion of the mathematical model properties, the stability of the coordinated system is proven. Specifically, a small gain theorem provides insight into the nature of the interconnection. Extensive experimental results obtained both on a test bench and on board a vehicle stress the relevance of the approach. A substantial speedup of the torque response is observed (the response time for the torque response on a large tip-in is reduced by 20%), and, further, it is possible to manage the mass of burned gas, which is convenient for cold-start. In Chapter 4, a low-pressure Exhaust Gas Recirculation (EGR) VLD equipped Diesel engine is studied. The model of Chapter 2 is complemented by further investigations to represent the rate of burned gases inside the cylinders. Here, the VLD is used to compensate for the sluggishness of the intake manifold burned gas rate. An Input-to-State-Stability (ISS) approach is considered to prove stability of the obtained cascade resulting from the proposed coordination. Supportive experimental results show significant reduction of NO_x during transients, resulting in on 5% reduction in NO_x generated over a NEDC dryving cycle and widely more on torque tips-in and out.

The presented coordination methodology is very general. It consists of using the actuators, to control the cylinder filling as optimally as possible. The objectives treated in the SI and CI cases are particular cases. Extensions are possible. These objectives have been reached thanks to existing VVA actuators, without any further sensor nor actuator, at the sole expense of an improvement of the embedded software.

Acronyms, notation and mathematical definitions

Acronyms

AFR	Air/Fuel Ratio
BDC	Bottom Dead Center
BGR	Burned Gas Rate
CI	Compression Ignition
CO	Carbon Monoxide
CO_2	Carbon Dioxide
DOHC	Double Over Head Camshaft
EGR	Exhaust Gas Recirculation
evc	Exhaust Valve Closing
evo	Exhaust Valve Opening
HC	Hydrocarbons
HP	High Pressure
IEGR	Internal Exhaust Gas Recirculation
IGR	Internal Gas Recirculation
IMEP	Indicated Mean Effective Pressure
ISS	Input-to-State Stability
ivc	Intake Valve Closing
ivo	Intake Valve Opening
LP	Low Pressure
LTC	Low Temperature Combustion
LTV	Linear Time Varying
MAF	Mass Air Flow
NEDC	New European Driving Cycle
NO_x	Nitrogen Oxides

PI	Proportional Integral
PM	Particulate Matter
SI	Spark Ignition
TDC	Top Dead Center
TWC	Three Way Catalyst
UGAS	Uniformly Globally Asymptotically Stable
UGES	Uniformly Globally Exponentially Stable
VGT	Variable Geometry Turbocharger
VLD	Variable Lift and Duration
VVA	Variable Valve Actuation
VVT	Variable Valve Timing

General Notation

Symbol	Quantity	Unit
AFR_s	Stoichiometric air/fuel ratio	-
$Area$	Opening area under both valves	m^2
m_{asp}^{exh}	In-cylinder aspirated mass from the exhaust manifold	kg/stroke
m_{asp}^{int}	In-cylinder aspirated mass from the intake manifold	kg/stroke
m_{cyl}	In-cylinder mass at *ivc*	kg/stroke
m_{evc}^{exh}	Exhaust gas mass at *evc*	kg/stroke
m_f	Injected fuel mass	kg/stroke
$m_{overlap}^{exh}$	Mass of gas through both valves	kg/stroke
$\dot{m}_{asp}^{exh}$	Aspirated mass flow from the exhaust manifold	kg/s
$\dot{m}_{asp}^{int}$	Aspirated mass flow from the intake manifold	kg/s
$\dot{m}_{MAF}$	Intake mass air flow measured by MAF sensor	kg/s
n_{cyl}	Number of cylinders	-
N_e	Engine speed	rpm
OF	Overlap factor	$\text{m}^2 \cdot \text{deg}$
P_{int}	Intake manifold pressure	Pa
P_{cyl}	In-cylinder pressure at *ivc*	Pa
P_d	Downstream pressure	Pa
P_{exh}	Exhaust manifold pressure	Pa
P_u	Upstream pressure	Pa
R	Ideal gas constant	J/kg/K

Symbol	Quantity	Unit
T_{cyl}	In-cylinder temperature at *ivc*	K
T_{exh}	Exhaust manifold temperature	K
T_{int}	Intake manifold temperature	K
T_u	Upstream temperature	K
T_q	Engine torque	Nm
V_{BDC}	In-cylinder volume at BDC	m^3
V_d	Total displaced volume of all the cylinders	m^3
V_{ivc}	In-cylinder volume at *ivc*	m^3
V_{int}	Intake manifold volume	m^3
V_{TDC}	In-cylinder volume at TDC	m^3
V_{evc}	In-cylinder volume at *evc*	m^3
$\boldsymbol{A}$	Matrix of regressors	*
$\boldsymbol{B}$	Matrix of regressors	*
$\boldsymbol{y}$	Measurement vector	*
$\boldsymbol{\alpha}$	Parameter vector	*
γ	Specific heat ratio	-
θ_{evc}	*evc* angle	deg
θ_{ivc}	*ivc* angle	deg

Notations for the SI case study

Symbol	Quantity	Unit
$Area_{th}$	Throttle opening area	m^2
m_{asp}	In-cylinder aspirated mass from the intake manifold	kg/stroke
m_{asp}^{pred}	Predicted in-cylinder aspirated mass	kg/stroke
m_f^{ff}	Feedforward term for fuel injection	kg/stroke
m_{igr}	IGR mass	kg/stroke
$\dot{m}_{at}$	Throttle mass air flow	kg/s
P_{dc}	Downstream compressor pressure	Pa
α_1	First breathing model parameter term	-
α_2	Second breathing model parameter term	$\mathrm{kg/m^2/s}$
α_3	Third breathing model parameter term	$\mathrm{kg/m^3}$
η_{vol}	Volumetric efficiency	-
$\delta\eta$	Volumetric efficiency modeling error	-

Symbol	Quantity	Unit
ϵ_{th}	Throttle mass flow modeling error	kg/s
Φ_{int}	Intake VVT actuator position	deg
Φ_{exh}	Exhaust VVT actuator position	deg
θ_{th}	Opening throttle angle	%

Notations for the CI case study

Symbol	Quantity	Unit
c_v	Constant volume specific heat	J/kg/K
P_{evo}	In-cylinder pressure at *evo*	Pa
Q_{LHV}	Lower heating value of fuel	J/kg
T_{ac}	In-cylinder temperature after combustion	K
T_{bc}	In-cylinder temperature before combustion	K
T_{ivc}	In-cylinder temperature at *ivc*	K
X_{exh}	Exhaust manifold BGR	-
X_{iegr}	In-cylinder BGR at *ivc*	-
X_{int}	Intake manifold BGR	-
X_{ivc}	In-cylinder BGR at *ivc*	-
V_{comb}	In-cylinder volume when combustion occurs	m^3
β_1	First breathing model parameter term	-
β_2	Second breathing model parameter term	-
δ_T	Tolerated temperature overrun	K
μ_1	First combustion model parameter	-
μ_2	Second combustion model parameter	-
Φ_{vld}	VLD actuator position	deg

Mathematical definitions

$\|\cdot\|$ stands for the Euclidean norm.

The induced norm of a matrix $\boldsymbol{M} \in \mathcal{M}_n(\mathbb{R})$ is defined as $\|\boldsymbol{M}\| = \sup_{v\in\mathbb{R}^n,\ v\neq 0} \frac{\|\boldsymbol{M}v\|}{\|v\|}$.

Definition 1 **([34]).**
A continuous function $\alpha : [0; a) \to [0; \infty)$ *is said to belong to the* ***class*** $\mathcal{K}$ *if it is strictly increasing and* $\alpha(0) = 0$*.*

Definition 2 **([34]).**
A continuous function $\beta : [0; a) \times [0; \infty[\to [0; \infty)$ *is said to belong to the* ***class*** $\mathcal{KL}$ *if, for a fixed* s*, the mapping* $\beta(r, s)$ *belongs to the class* $\mathcal{K}$ *with respect to* r *and, for a fixed* r*, the mapping* $\beta(r, s)$ *is decreasing with respect to* s *and* $\beta(r, s) \to 0$ *as* $s \to \infty$*.*

Definition 3 **([34]).**
Consider the system

$$\dot{x} = f(t, x, u) \tag{1}$$

where $f : [0,\ \infty) \times \mathbb{R}^n \times \mathbb{R}^m \to \mathbb{R}^n$ *is piecewise continuous in* t *and locally Lipschitz in* x *and* u*. The system (1) is said to be* ***input-to-state stable (ISS)*** *if there exist a class* $\mathcal{KL}$*-function* β *and a class* $\mathcal{K}$*-function* γ *such that for any initial state* $x(t_0)$ *and any bounded input* $u(t)$*, the solution* $x(t)$ *exists for all* $t \geq t_0$ *and satisfies*

$$\|x(t)\| \leq \beta(\|x(t_0)\|, t - t_0) + \gamma\left(\sup_{t_0 \leq \tau \leq t} \|u(\tau)\|\right)$$

Definition 4 **([31]).**
Consider the system

$$x(k+1) = f(x(k), u(k)) \tag{2}$$

The system (2) is said to be ***input-to-state stable (ISS)*** *if there exist a class* $\mathcal{KL}$*-function* β *and a class* $\mathcal{K}$*-function* γ *such that for any initial state* $x(k_0)$ *and any bounded input* $u(k)$*, the solution* $x(k)$ *exists for all* $k \geq k_0$ *and satisfies*

$$\|x(k)\| \leq \beta(\|x(k_0)\|, k - k_0) + \gamma\left(\sup_{k_0 \leq s \leq k} \|u(s)\|\right)$$

Chapter 1

A description of cylinder filling control issues for Variable-Valve-Actuation internal combustion engines

In this first chapter, the issues related to cylinder filling in internal combustion engines equipped with Variable Valve Actuation devices are described. Both cases of Spark Ignition (SI) and Compression Ignition (CI) are discussed. Following a physical description of the involved technologies and the filling phenomenon, the role of usually considered control systems is detailed. This stresses the necessity for a coordination strategy to take better advantage of the full potential of VVA devices.

1.1 Background on internal combustion engines

First, one focuses on a general technological description of internal combustion engines.

1.1.1 Engine four-stroke operating cycle

The purpose of internal combustion engines is the production of mechanical power from the chemical energy contained in the fuel. The internal combustion engines under consideration in this thesis are Spark-Ignition (SI) engines (also referred to as Gasoline engines) and Compression-Ignition (CI) engines (also referred to as Diesel engines).

Internal combustion engines found in cars most commonly use a four-stroke cycle. The four strokes refer to intake, compression, combustion (power) and exhaust strokes occurring during two crankshaft rotations during each working cycle of the SI engine and CI engine.

A four-stroke engine is characterized by four strokes, or reciprocating movements of a piston in a cylinder (see Figure 1.1, intake and exhaust valve lifts are presented at the bottom). The cycle begins at top dead center (TDC), when the piston is the farthest away from the axis of the crankshaft. On the intake or induction stroke of the piston, the piston goes down from the top of the cylinder, reducing the pressure inside the cylinder (phase ①). Fresh air is forced into the cylinder through the intake port. The intake valve then closes near bottom dead center (BDC), and, then, fuel is injected into the cylinder (for direct injection engines). The compression stroke compresses the fuel-air mixture (phase ②). The air-fuel mixture is then ignited near the end of the compression stroke, usually by a spark plug (for SI engines) or by the heat and pressure of compression (for CI engines). The resulting pressure of burning gases pushes the piston through the power stroke (phase ③). In the exhaust stroke, the piston pushes the products of combustion from the cylinder through the exhaust valve (phase ④).

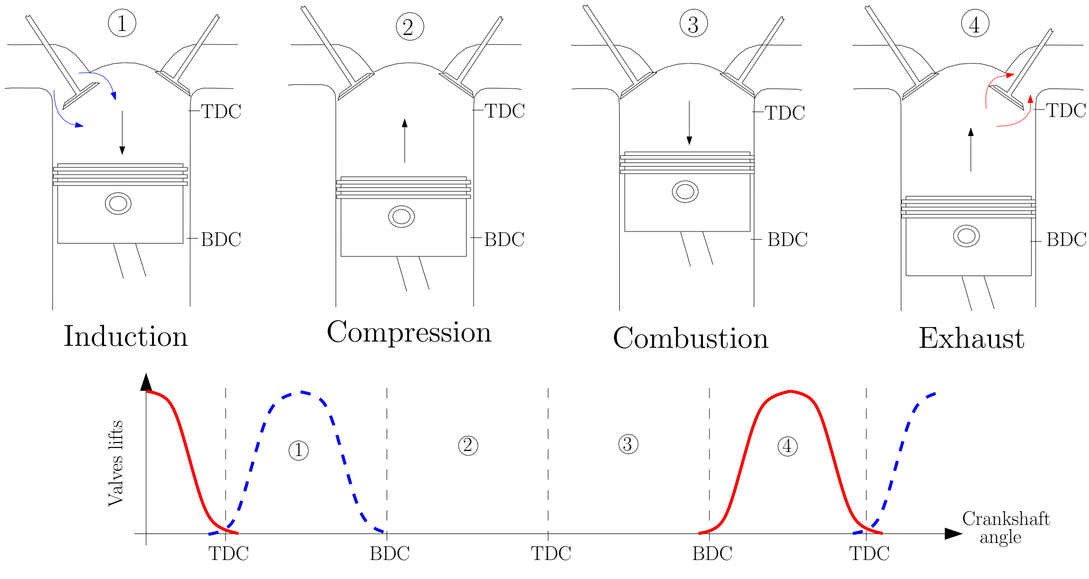

Figure 1.1: Four-stroke cycle of internal combustion engines. Four successive phases (induction, compression, combustion, exhaust) take place. They are separated by TDC and BDC.

1.1.2 Around the combustion chamber

The engine cylinders are contained in the engine block. The combustion-generated gas pressure in the combustion chamber pushes down the piston which transmits the energy to the crankshaft via the connecting rod (see Figure 1.2). The cylinder head contains the spark plug (in the case of SI engines), a fuel injector[1], and a part of the valve mechanism. A camshaft with one cam per valve is used to open and close the valves with an accurate timing. Fresh air comes from the intake manifold and burned gases are expelled towards the exhaust manifold.

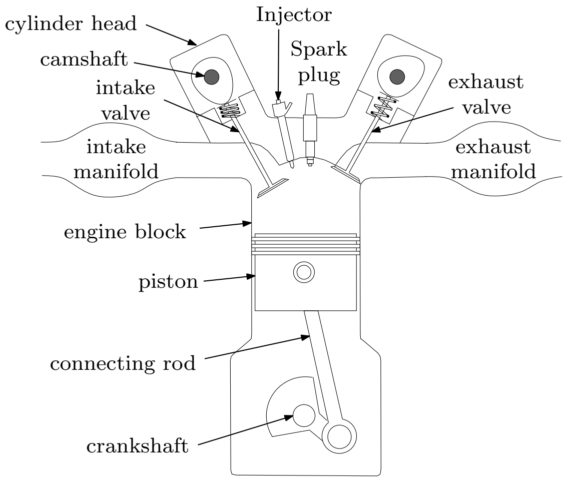

Figure 1.2: Engine components about the combustion chamber.

1.1.3 Variable Valve Actuation technologies

Conventional engines are designed with fixed mechanically-actuated valves. The position of the crankshaft, and the profile of the camshaft determine the valve events (i.e, the timing of the opening and closing of the intake and exhaust valves) as is pictured in Figure 1.1. In conventional engines, valve motion is mechanically determined by the crankshaft position (through the camshaft), and the valve motion is the same for all operating conditions. In this situation, the cylinder filling (in-cylinder pressure, temperature, mass) is only a function of the intake manifold thermodynamic quantities and the engine speed. However, the ideal scheduling (in terms of consumption, emissions, and combustion stability) of the valve events greatly differs between different operating conditions (e.g. at idle, partial load or high load). This simplification represents a significantly costly trade-off in engine design [45, 68, 77].

---

[1] The fuel injector can be located either in the intake pipe (port-fuel injection) or in the cylinder (direct injection).

To optimize the engine behavior over its whole operating range, Variable Valve Actuation (VVA) devices have been introduced since the early 90's. These modify the valves lifts profiles pictured in Figure 1.1. Engines equipped with VVA can be categorized by their means of actuation: electro-hydraulic, electromechanical, and *cam-based actuators*. Thanks to its quality-price ratio, cam-based actuation has quickly become standard on many production engines [1]. Maximizing their potential benefits has been the topic of significant research and development.

Cam-based actuators can be categorized into discretely-staged cam-profile switching systems [23], Variable Valve Timing (VVT) systems and continuously variable cam-profile systems [19]. Discretely-staged cam-profile switching systems generally have two or possibly three different cam profiles that one can switch from. VVT allows change to the valve timings, but not the valve lift profiles and durations themselves. The camshafts can only be advanced or delayed with respect to its neutral position on the crankshaft. VVT can be controlled by a hydraulic actuator called a cam phaser [4]. Engines can have a single cam phaser (intake cam only) or two cam phasers (both intake and exhaust cams) as pictured in Figure 1.3(a). Continuously-variable cam-profile systems have a profile with a constant shape, but its magnitude can be increased or decreased within a range of values [38, 40]. Figure 1.3(b) represents a second exhaust valve lift capability, referred to as VLD (Variable Lift and Duration) system, as an example to a continuously-variable cam-profile type system.

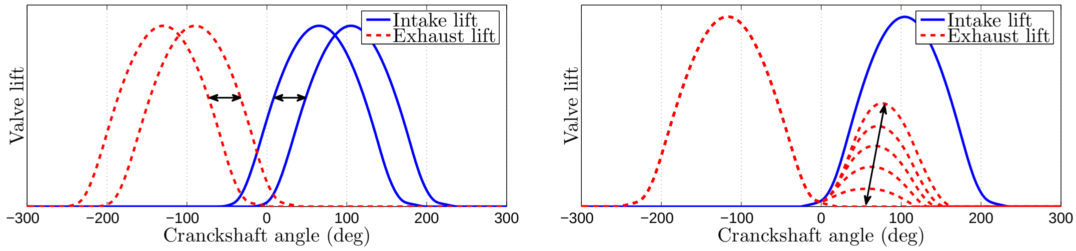

(a) Dual independent VVT. Valve timing actuators can move separately.

(b) VLD actuator controls the exhaust valve lift and duration re-opening.

Figure 1.3: Two examples of VVA technologies: a variable valve timing system (VVT) and a continuously variable cam-profile system (VLD).

1.2 Background on VVT equipped SI engines

Now, the particular case of SI engines is detailed. The nature of the cylinder gas exchange, the importance of pumping losses, and the role of gas recirculation and scavenging that are generated using VVT actuators are detailed. Finally, the limitations of classic control designs during transients are stressed.

1.2.1 SI engine generalities: the air and fuel inflows

In SI engines, the air/fuel mixture is ignited by an electrical discharge arising across the spark plug. This starts the combustion process at the end of the compression phase. To guarantee a reliable combustion, the ratio of air mass flow to fuel mass flow must be held approximately constant at a level determined by the stoichiometry. Further, to reduce pollutant emissions and meet emissions standards[2], SI engines have been equipped with three-way catalytic converters [21] (see Appendix C)[3] that force the engine to operate under stoichiometric conditions.

Due to the necessity of maintaining a stoichiometric blend of air and fuel in the combustion chamber, the variation of the torque output of an SI engine is obtained by *simultaneously* modifying the air mass flow and the fuel mass flow entering into the cylinders (and to some extents also by modifying the spark advance [66]). A throttle valve [79], located at the intake of the engine (see Figure 1.4), controls the air flow (through the intake manifold pressure) while injectors (located in the inlet ports or in the chamber for direct injection engines) control the amount of fuel that has to be injected to keep the constant air/fuel ratio. Because of the slowness of the fresh air cylinder filling process compared to the instantaneous fuel injection process, the engine torque output follows the aspirated air mass dynamics. It is then of paramount importance to accurately control the aspirated air mass.

1.2.2 Ways to lower consumption: downsizing, turbocharging and pumping losses

The main problem of the SI engine is its poor efficiency at low load [24]. The use of a throttle in the intake manifold implies non-negligible pumping losses. Because of

---

[2] For a few years, emissions standards have appeared to set specific limits to the amount of pollutants that can be released into the environment. Many emissions standards focus on regulating pollutants released by automobiles. The European Union has its own set of mandatory emissions standards (“Euro”). The emission levels of car engines are determined on the New European Driving Cycle (NEDC) test cycle. It is supposed to represent the typical usage of a car in Europe. Standards for SI and CI engines generally focus on the emissions of Nitrogen Oxides (NO_x), Carbon Monoxide (CO), Particulate Matter (PM) and volatile Hydrocarbons (HC).

[3] This device located at the exhaust of the engine has three simultaneous tasks: to reduce NO_x, to oxidize CO and to oxidize unburned HC. These three reactions occur most efficiently when the catalytic converter receives exhaust from an engine running near the stoichiometric point. This is about 14.6 parts air to 1 part fuel, by weight, for gasoline.

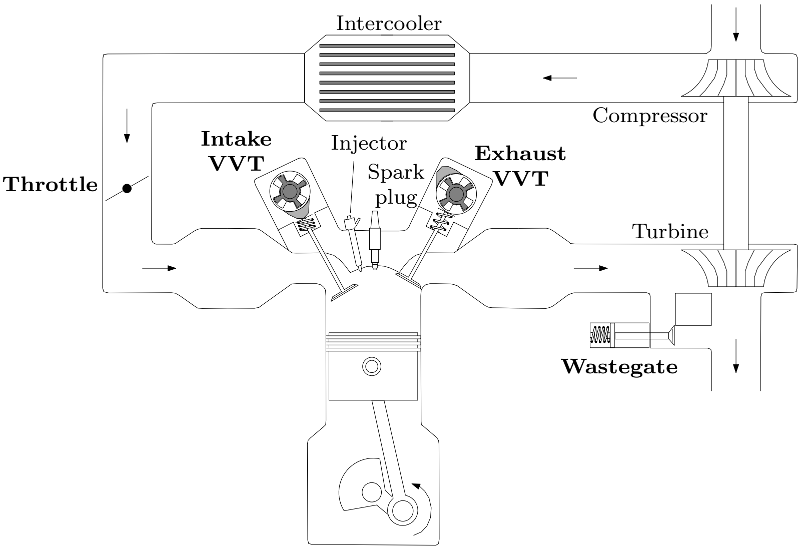

Figure 1.4: Schematic illustration of a turbocharged, VVT-equipped SI engine.

a low intake manifold pressure at low and partial load, the pumping work[4] is large and contributes to a poor global efficiency of the engine.

Some new technological solutions have appeared to improve the overall efficiency (and reduce fuel consumption) of SI engines. One of the most promising way is the reduction of the engine capacity, named *downsizing* [44]. To generate the same torque output (same cylinder fresh air mass quantity) as with an engine of larger capacity, the intake manifold pressure has to be higher. Consequently, the depression created by the throttle is decreased, and so is the negative pumping work. Downsizing leads to a better engine efficiency, but requires supercharging to maintain performances [63]. Engine supercharging can be achieved using a turbocharger that recovers energy from the exhaust gas, as pictured in Figure 1.4. The compressor is powered by the turbine located downstream of the exhaust manifold. A wastegate valve deflects part of the turbine flow, and thus indirectly controls the compression rate. The turbocharger controls the intake manifold pressure at high load (when the intake throttle is fully open). As a drawback, the turbocharger inertia implies a large response time, during transient, for the intake manifold pressure, and then in the engine torque output.

Additional improvements are achieved using VVT devices [37, 44]. VVT actuators are located on the camshafts (see Figure 1.4) and permit independent modification of the timing of the intake and exhaust valves lifts, and, in turn, drastically modify the fresh air cylinder filling process. Their impact on the engine behavior is detailed in the following section.

---

[4] Work transfer between the piston and the cylinder gases during the induction and exhaust strokes [24].

1.2.3 Impact of VVT actuators on the engine

VVT actuators have a strong impact on the cylinder filling process. Indeed, modifying the timing of both the intake and exhaust valves (see Figure 1.3(a)) affect the cylinder filling through two effects. First, the variation of the valve overlap (time when both valves are open together) permits the realization of an Internal Gas Recirculation (IGR). This phenomenon depends on the engine operating range since it is a function of the pressure difference between the intake and exhaust manifolds. Secondly, modifying the timing of the intake valve permits modulation of the effective cylinder capacity, and, so, the admissible air volume. Now, we detail the beneficial impacts of the VVT actuators under part load and under high load conditions.

VVT at partial load: the benefits of the internal burned gas recirculation

Under partial load, because of the negative pressure difference between the intake and exhaust manifolds, increasing the valve overlap permits exhaust gas back-flow towards the intake (see Figure 1.5). These gases are then directly reintroduced into the chamber during the intake stroke. An increase of the in-cylinder burned gas quantity results.

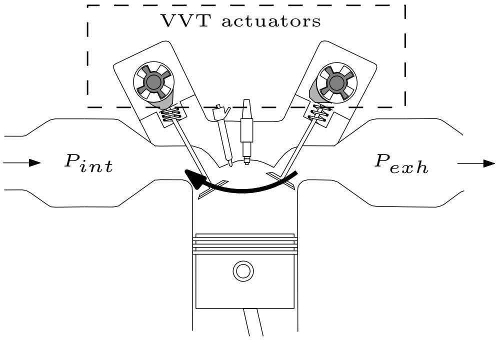

Figure 1.5: Under atmospheric conditions, *back-flow* of exhaust burned gases may occur during the intake stroke.

This IGR of burned gases modifies the fresh air cylinder filling, because burned gases occupy a non-negligible cylinder volume. Two beneficial impacts result. First, IGR permits a reduction in the pumping losses (like downsizing) because it is necessary to increase the intake manifold pressure to keep a constant aspirated air mass (and then torque output). Secondly, the presence of burned gases has the effect of slowing down the combustion. A reduced combustion temperature, that is beneficial in terms of NO_x emissions [24], follows.

Figure 1.6 shows the effects of the burned gas quantity on the intake manifold pressure and the NO_x emissions at constant torque. The higher the valve overlap is, the higher the amount of the residual gas. An increase of the intake manifold pressure to keep a constant engine torque (decrease of the pumping losses, and then of the consumption), and a decrease of the NO_x emissions follows.

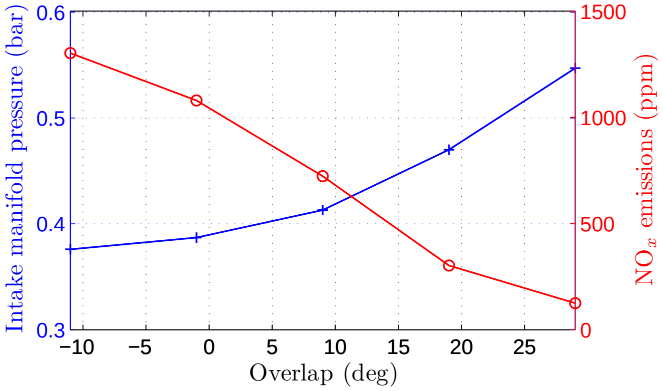

Figure 1.6: Beneficial effects of valve overlap variations on the intake manifold pressure and the NO_x emissions at constant engine speed (1500 rpm) and constant torque (30 Nm). Experimental data obtained on a 4-cylinder SI engine test bench equipped with VVT actuators.

From a combustion viewpoint the presence of burned gases inside the cylinder increases the in-cylinder temperature prior to combustion. This accelerates fuel vaporization and improves charge homogenization prior to ignition. On SI engines, an optimized combustion is obtained by limiting air/fuel ratio dispersions in the chamber, because rich zones burn with a lower efficiency. In this case fuel is only partially oxidized and the part of the CO in the combustion products increases. Formation of CO during combustion provides less energy than the generation of CO_2. Thus, residual burned gases yield an additional fuel consumption reduction by improving the mixing.

On the other hand, burned gas quantity must be upper bounded to ensure combustion stability. Water and CO_2 molecules contained in the burned gases slow down the flame propagation. These molecules are characterized by a higher specific heat than air. Flame temperature is then lower and propagation is less efficient.

VVT at high load: the benefits of scavenging

At high load, because of the positive pressure difference between the intake and exhaust manifolds (thanks to the turbocharger capabilities [44, 65]), increasing the valve overlap permits some fresh gases to flow through the cylinder, driving out the residual burned gases (see Figure 1.7). This is the *scavenging* effect.

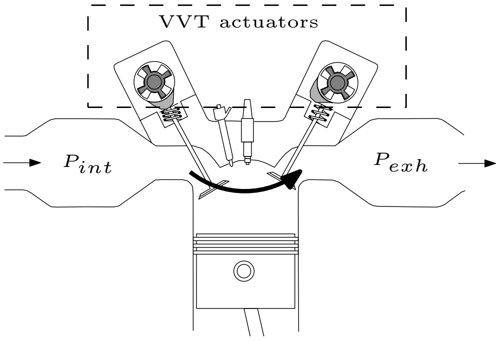

Figure 1.7: Under turbocharging conditions, a part of the fresh air can be *scavenged* towards the exhaust pipe.

At high load, combustion efficiency is limited by the knock phenomenon[5] [24]. Spark advance has to be shifted from its optimum value to prevent knock. Knock is strongly related to the presence of in-cylinder burned gases, because of their high temperature. Thanks to scavenging, burned gases are easily removed from the cylinder. Moreover, the fresh gases flowing through the cylinder to the exhaust pipe during the scavenging phase lower the in-cylinder temperature. Then, spark advance can be set to its optimum value, combustion becomes more efficient, and fuel consumption is reduced.

The decrease in in-cylinder temperature also implies an increase of the aspirated fresh air mass. It can be observed on the engine performances with an increase of the maximum achievable torque. Moreover, increasing the scavenged air mass flow allows an earlier turbine initiation (also referred to as turbo lag reduction). This contributes to increase the engine load at low engine speeds [37, 41, 63].

1.2.4 Existing controllers for SI engines

Earlier in Section 1.2.1, it has been seen that the engine torque output is related to the aspirated fresh air mass. In fixed valve timing engines, this variable is controlled through the intake manifold pressure (actuating the throttle and the wastegate). In VVT engines, the problem is more involved since the VVT actuators have a strong impact on the aspirated air mass. Controlling the torque of a VVT equipped SI engine is then equivalent to controlling both the intake manifold pressure and the VVT actuators positions.

---

[5] Knock is the name given to the noise which is transmitted through the engine structure when essentially spontaneous ignition of a portion of the gas occurs.

As seen it in Section 1.2.3, in classic engine control strategies, VVT actuators are used to optimize the engine efficiency (by reducing the pumping losses) while minimizing the pollutant emissions. As a result of such a trade-off, static positions of the VVT actuators are determined to cover every possible engine set point (see e.g. [4] or [45]). The VVT actuators are used in a *passive* way: they are independent of the system functioning. In practice, this positioning is used as follows. From a torque request specified by the driver through the accelerator pedal, and from the engine speed, two-dimensional look-up tables give set points for the intake manifold pressure and VVT actuators positions (see Figure 1.8).

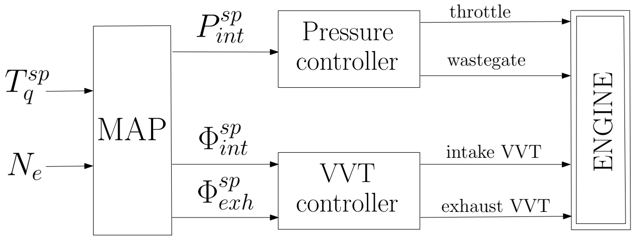

Figure 1.8: Classic control strategy to manage the cylinder filling. T_q^{sp} and N_e refer to the driver torque demand and the engine speed, respectively. Look-up tables determine set points for the intake manifold pressure and VVT actuator positions, P_{int}^{sp}, Φ_{int}^{sp}, and Φ_{exh}^{sp}.

The intake manifold pressure and VVT actuators controllers can be considered as low-level controllers. In this thesis; only asymptotic stability properties and rough estimates of the response times of these controllers are used. No design detail are developed. An exception is made for the intake manifold pressure controller under atmospheric conditions (using the throttle actuator), which is addressed in Appendix A for which a new contribution is proposed. Some intake manifold pressure controllers under turbocharged conditions are given in [60, 69, 76] for example. Some VVT actuators controllers can be found in [8, 18]. Reference static positioning of the VVT actuators are given in Appendix D.

1.2.5 Issues during transients

The dynamic responses of the intake manifold pressure and VVT actuators are rather different. On the one hand, the response of the intake manifold pressure is quite fast under atmospheric conditions because it is controlled by the throttle, which is electrically actuated and follows a fast first-order dynamics representing the filling–emptying phenomenon of the intake manifold [24]. Under turbocharging conditions, the inertia of the turbocharger substantially slows down the response of the intake pressure. On the other hand, the VVT mechanism (see [19] for a complete description) is slower than the intake pressure dynamics under atmospheric conditions.

These discrepancies between the response time of the two subsystems (the intake manifold pressure and the VVT actuators) during transients may lead to performance losses [75] because cylinder filling objectives are not satisfied. Figure 1.9 reports results on a large torque tip-in. The two figures on the left present the intake manifold pressure and the VVT actuators positions set points and measurements respectively. The figure on the right pictures the resulting engine torque output. It is clear that two distinct dynamics are observed for the two low-level subsystems. Indeed, the intake pressure is slower than the VVT actuators because of the turbocharger inertia (at the beginning of the transient, the pressure is widely faster because it is modulated thanks to the throttle). Here, VVT actuators are not optimally used because they passively remain stuck on their reference mapped positions during the transient.

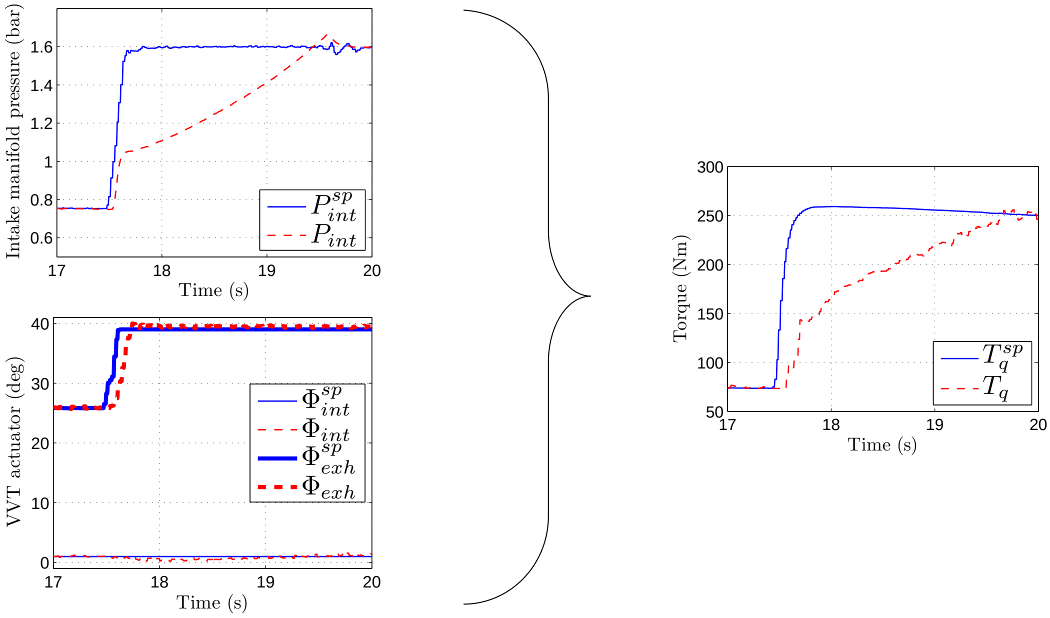

Figure 1.9: Experimental results obtained on vehicle during a large torque tip-in. Classical controller do not exploit the VVT actuators at their best. These are fed with static set points values. The obtained torque response is relatively slow, and can be improved.

From the preceding observations, an issue has been identified.

Problem 1 (VVT SI engine)**.**
The difference in response times of the two subsystems contributing to the cylinder filling (the intake manifold pressure and the VVT actuators) lead to engine performance losses in terms of torque response.

1.3 Background on VLD equipped CI engines

Now, one focuses on CI engines. The nature of cylinder gas exchange and the usage of VLD actuators are detailed. The limitations of classic control architectures are stressed.

1.3.1 CI engine generalities: the air and fuel inflows

A CI engine is an internal combustion engine using the heat of compression to ignite the fuel, which is injected into the combustion chamber during the final stage of compression. Torque production control is achieved by varying the amount of fuel injected during each cycle[6]; the air flow at a given engine speed is essentially unchanged in naturally aspirated engines (combustion is lean). Modern CI engines are usually equipped with a Variable Geometry Turbocharger (VGT, see Figure 1.10). This permits an increase in engine torque output by increasing the air mass flow per displaced volume unit, thereby allowing an increase in fuel flow [24]. Besides a substantial decrease of consumption arising from higher engine efficiency, CI engines generate problematic pollutant emissions.

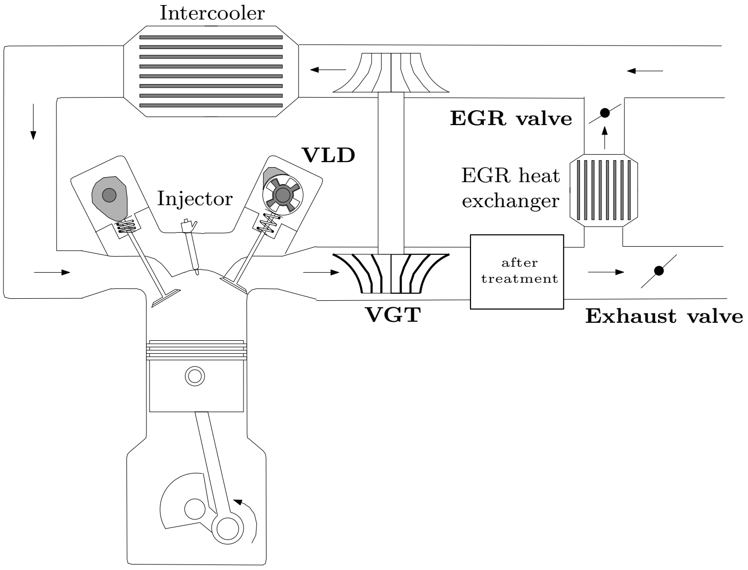

Figure 1.10: Schematic illustration of turbocharged, VLD-equipped CI engine.

---

[6] Contrary to SI engines, no stoichiometric blend is needed.

1.3.2 Towards lower emissions using EGR

Upcoming Diesel engines emission standards such as Euro 6[7] require significant reduction of smoke, HC, CO and above all NO_x emissions. This has spurred an interest in new (cleaner) combustion modes. Premixed combustion modes (LTC: Low Temperature Combustion) represent a relatively simple and affordable solution to reduce the emissions while retaining the advantages of the CI engine. These modes consist of incorporating large amounts of Exhaust Gas Recirculation (EGR) into the combustion process. The change of in-cylinder oxygen by exhaust gas reduces the availability of oxygen during the combustion. This lowers the post-combustion temperature, leading to decreased NO_x emissions (see [58], [39], [70] and the references therein). NO_x emissions is then deeply related to the Burned Gas Rate (BGR)[8] inside the cylinder.

Control of the BGR can be realized in two possible manners: through a High Pressure (HP) or a Low Pressure (LP) EGR circuit. The LP EGR technology (which is considered in this thesis, as pictured in Figure 1.10) possesses many advantages over the HP EGR circuit. In this technology, the exhaust gases are picked up downstream of the turbine and the after-treatment system (see Figure 1.10). The fresh air and burned gases mix and then flow through the compressor. The advantages of LP EGR are threefold. First, due to the EGR circuit length, the intake manifold mixture temperature is lower than in the case of the HP EGR. This has a beneficial impact on the NO_x emissions. Second, higher EGR rates can be obtained because LP EGR does not have a significant discharge effect on the turbocharger. Third, because the recirculated gases are cleaned by the after-treatment system, there is no problem of exchanger fouling. However, one main drawback of the LP technology is the large settling time because of EGR pipe length and low inlet-outlet pressure difference.

Recently, a new way to generate EGR can be achieved using a VLD device [5]. The VLD actuator is located on the camshaft (see Figure 1.10). It permits a variable exhaust valve re-opening that drastically modifies the cylinder filling process. Its impact on the engine working is detailed in the following section.

1.3.3 Impact of VLD on the engine: benefits of the internal gas recirculation

As has been discussed previously in Section 1.3.2, the LP EGR provides good results in terms of NO_x emissions. Nevertheless, a reduced exhaust temperature resulting from the highly diluted combustion tends to produce a sharp increase in HC and CO emissions at part load because of after treatment catalyst deactivation [5]. Utilization of a VLD actuator can address this problem. VLD re-inducts the gases directly inside the combustion chamber (Internal Exhaust Gas Recirculation, IEGR). Significantly higher gas temperature levels at valve closure can be reached. This permits to activate the catalyst, and, in turn, to reduce the HC and CO emissions.

---

[7] European emissions standard from 2014.

[8] Mass of burned gas over total mass. The burned gas rate in the intake manifold is equal to the EGR rate multiplied by the fuel/air ratio

In engines where both external EGR and IEGR take place, the in-cylinder BGR and temperature can be controlled. Figure 1.11 reports emissions measurements in regards to an increase of EGR/IEGR rates (using either the LP EGR or the VLD) at constant IMEP[9]. In details, Figure 1.11(a) gives NO_x results for increasing EGR/IEGR rates, while Figure 1.11(c) and Figure 1.11(d) underline the beneficial impact of hot residual gases on the HC-CO emissions. Finally, Figure 1.11(b) shows that higher in-cylinder mixture temperature increases the smoke emissions.

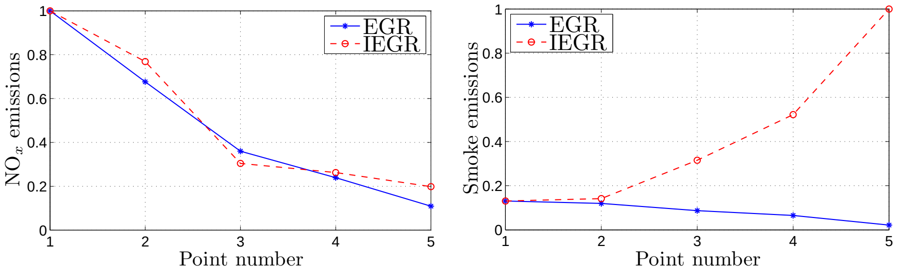

(a) NO_x emissions (b) Smoke emissions

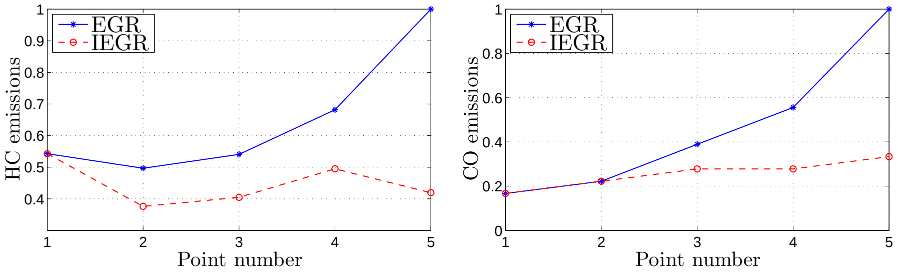

(c) HC emissions (d) CO emissions

Figure 1.11: Engine emissions for increasing external or internal EGR at constant IMEP (2 bar), constant engine speed (2000 rpm) and constant intake manifold pressure (1 bar). IEGR allows a reduction of the HC-CO emissions to the detriment of the smoke emissions. Experimental data obtained at test bench on a 4-cylinder CI engine equipped with VLD actuator and LP EGR capability.

---

[9] The IMEP (Indicated Mean Effective Pressure) is the work delivered to the piston over the entire four strokes of the cycle, per unit displaced volume.

1.3.4 Existing controllers for CI engines

It has been seen that the NO_x emissions are related to the in-cylinder BGR. In fixed valve timing engines, this variable is controlled through the intake manifold BGR (actuating the EGR valves). In VLD-equipped engines, it is more complicated since the VLD actuator has a strong impact on the in-cylinder BGR. Controlling the in-cylinder BGR of a VLD equipped CI engine is then equivalent to controlling both the intake manifold BGR and the VLD actuator position.

Following the same approach discussed for SI engines in Section 1.2.4, static positions of the VLD actuator are determined to cover every possible engine set point. The VLD actuator is used in a *passive* way, it is totally independent of the system function. In practice, this positioning is used as follows. From a torque request specified by the driver through the accelerator pedal, and from the engine speed, two-dimensional look-up tables give set points for the intake manifold BGR and the VLD actuator position (see Figure 1.12).

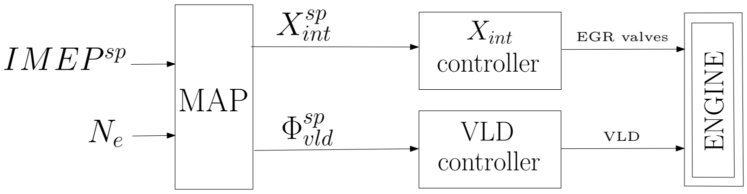

Figure 1.12: Classic control strategy to manage the cylinder filling. $IMEP^{sp}$ and N_e refer to the driver torque demand and the engine speed, respectively. Look-up tables determine set points for the intake manifold BGR and VLD actuator position, X_{int}^{sp} and Φ_{vld}^{sp}.

As in SI engines, the intake manifold BGR and VLD actuator controllers can be considered as low-level controllers. No details about the derivation of such controllers are given. Some intake manifold BGR controllers are given in [7, 18, 28]. Some VLD actuators controllers can be found in [8, 18]. Reference static positioning of the VVA actuator is exposed in Appendix D.

1.3.5 Issues during transients

The dynamic responses of the intake manifold BGR and the VLD actuator are rather different. On the one hand, the response of the intake manifold BGR is quite slow (because of the EGR pipe length, and the low inlet-outlet pressure difference). On the other hand, the VLD actuator dynamics is fast.

These discrepancies between the two subsystems (the intake manifold BGR and the VLD actuator) during transients lead to undesired engine behavior. The situation is similar to the one observed on SI engines in Section 1.2.5. Figure 1.13 gives results on NO$_x$ emissions during a IMEP transient. Detrimental emission peak can be observed. The two figures on the left give the intake manifold BGR and the VLD actuator position. The figure on the right reports the resulting NO$_x$ emissions. Here, the change of engine operating point modifies the intake BGR and VLD actuator position set points (more external EGR, and, consequently, less IEGR is required). Because of the intake manifold BGR sluggishness corresponding to a slow external EGR response (compared to a fast IEGR response because of the fast VVA actuator position actuation), the in-cylinder BGR objective is not satisfied. NO$_x$ emission peak follows from this poor in-cylinder BGR control. Here, the VLD actuator is not optimally used because it remains on its reference position during the transient (used as passive actuator).

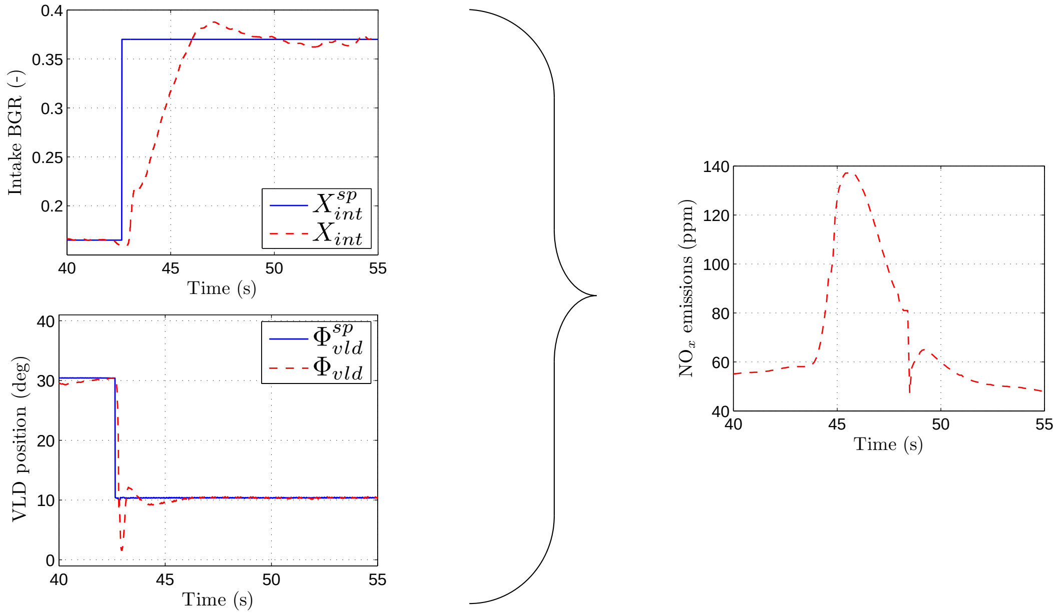

Figure 1.13: Experimental IMEP transient (3-5 bar) at test bench on a 4-cylinder CI engine equipped with VLD actuator and LP EGR capability. The difference in response times between the intake manifold BGR and the VLD actuator leads to NO$_x$ emission peak during transient.

This discussion allows us to identify a second issue.

Problem 2 (VLD CI engine)**.**
The difference in response times of the two subsystems contributing to the cylinder filling (the intake manifold BGR and the VVA actuator) lead to engine performance losses in terms of NO$_x$ emissions.

1.4 The proposed coordination solution

In summary, SI and CI engine controllers have similar block-scheme representation (pictured in Figure 1.8 and Figure 1.12 respectively). From a driver torque request and current engine speed, look-up tables derived under steady state conditions generate set points of the intake manifold quantities (pressure for SI engines, BGR for CI engines) and the VVA positions. Then, two low-level controllers track on these set points. At each engine stroke, fresh mixture coming from the intake manifold is aspirated into the cylinder, depending on the valves lifts profiles.

As has been identified in the statements of Problem 1 and Problem 2, differences in response times of the respective low-level controllers impact the cylinder filling during transients in non-favorable ways. This leads to a poor global engine behavior (torque for SI engines, emissions for CI engines). To improve the transient behavior, it is advantageous to coordinate the two subsystems. The proposed solution is to relate the intake manifold quantities/VVA and the in-cylinder filling quantities, without any modification of the low-level controllers (it is an add-on to an existing control strategy). Figure 1.14 pictures this coordination strategy. A high-level controller feeds the low-level controllers by coordinating them in order to satisfy a pre-defined cylinder filling objective.

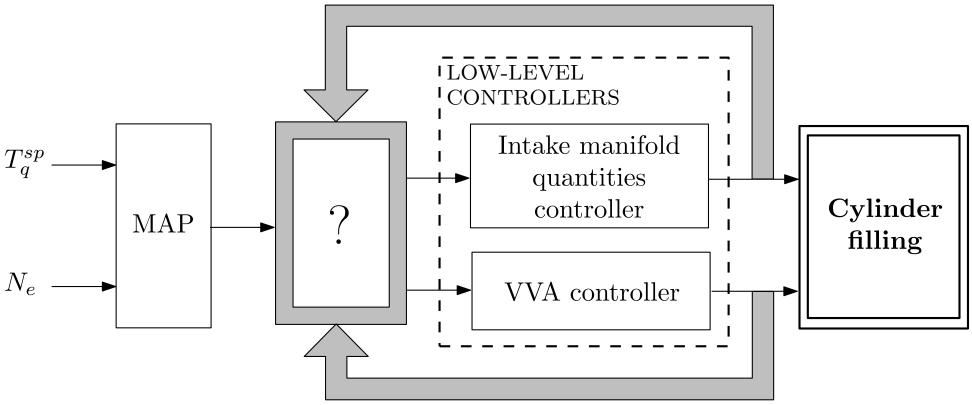

Figure 1.14: Sketch of the coordination-based control strategy. T_q^{sp} and N_e refer to the driver torque demand and the engine speed, respectively. A high-level controller block takes place upstream the low-level controllers.

It is now required to determine the right coordination strategy. A control law needs to be computed. For this purpose, a model of the cylinder filling process is now developed in the following chapter which will permit to quantitatively relate the cylinder quantities and the two low-level subsystems. This is done in the Chapter 3 and 4 respectively.

Chapter 2

Cylinder filling model of internal combustion engines

In this chapter, a general model for the filling of cylinders is presented. Following the discussion of Chapter 1, one looks for a model representing internal masses in terms of information from commonly available sensors: intake manifold thermodynamics quantities (pressure and temperature), VVA actuator position and engine speed. In particular, this discards approaches based on information from in-cylinder sensors (such as pressure sensors). For the control methodology sketched in Chapter 1 and to be exposed in details in Chapters 3 and 4, a model is required. In this chapter, such a model using analytic expressions is proposed. The model proposed here is valid for both SI and CI engines. Its structure and the identification of its parameters represent a contribution of importance for the following application chapters. The obtained models are given in equation (2.18) for the SI case study and in equation (2.20) for the CI case study respectively.

Two variables play important roles in the model: the in-cylinder air mass and the in-cylinder composition.

A common air mass flow model (see e.g. [10, 24, 36]) is given by the speed-density equation, which states that the mass of air flowing into the cylinders equals the volume flow of the engine multiplied by the air density. Because the engine does not behave as a perfect pump, the actual value of this flow is corrected by a volumetric efficiency η_{vol}, which is a dimensionless coefficient measuring the breathing performance of the engine. This coefficient is usually computed from steady-state measurements. Following the previous discussion, the mean flow aspirated (in kg/s) from the intake manifold is modeled under the form

$$\dot{m}_{asp}^{int} = \eta_{vol}(N_e, P_{int}) \frac{P_{int} V_d}{R T_{int}} \frac{N_e n_{cyl}}{2 \times 60} \tag{2.1}$$

where the volumetric efficiency η_{vol} is a function of the intake manifold conditions. It (almost exclusively) depends on the engine speed N_e (in rpm) and the intake manifold pressure P_{int}. Here, $\dot{m}_{asp}^{int}$ is the mean port mass flow. T_{int} is the intake manifold temperature. V_d is the displacement volume of the engine, n_{cyl} the number of cylinders, and R is the ideal gas constant. Integrating the signal over one engine cycle, the total mass aspirated from the intake writes

$$m_{asp}^{int} = \dot{m}_{asp}^{int} \frac{2 \times 60}{N_e n_{cyl}} \tag{2.2}$$

This model is only valid for fixed valve engines. In variable valve gear applications, the modification of the valve lift profiles affects the cylinder breathing process. Figure 2.1 shows that any valve-timing change strongly impacts the volumetric efficiency on a VVT turbocharged SI engine. Besides impinging on the fresh air coming from the intake, increasing the valve overlap (both valves being opened simultaneously) also increases the internal recirculation of burned gases. For this reason, it is necessary to account for the valve lift profiles (and their overlap) to model the cylinder filling (composed of both the aspirated mass from the intake and the aspirated mass from the exhaust).

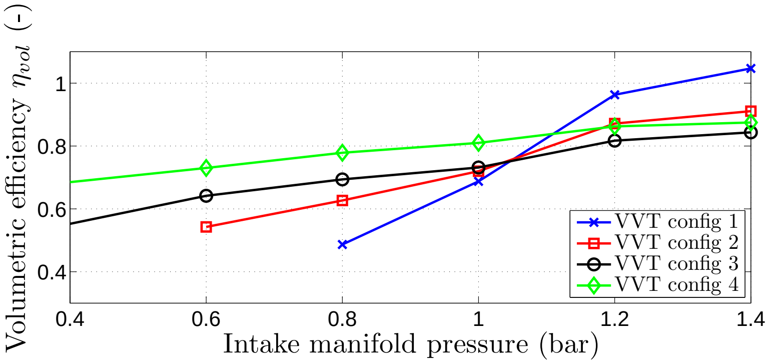

Figure 2.1: Volumetric efficiency function of the intake manifold pressure, at constant engine speed (1500 rpm), and different positions of the VVT actuators.

Some models of the in-cylinder aspirated air mass have been proposed in the literature for engines equipped with VVT actuators. In [73], a polynomial model is given for a dual equal VVT SI engine. Besides addressing a different VVT system than the one considered here, the complexity of this model is too high for the application. In [29], Jankovic *et al.* assume that the air flow rate in the VVT engine is an affine function of the intake manifold pressure (for a given engine speed and camshaft phasing). This model does not account for the two independent VVT actuators that are considered here. In [13] and [85], artificial neural networks are used for dual independent VVT SI engines. These complex models are not easily invertible which is inconsistent with our requirements. In [82], the aspirated mass is estimated thanks to a first principles model based on the in-cylinder pressure estimated from an exhaust pressure sensor. On top of the fact that this model appears very hard to calibrate, the use of the exhaust pressure sensor is impossible in our case. As a result, none of the models from the literature can be used in our approach.

Modeling the in-cylinder burned gas mass is a challenging issue, because it is difficult to actually measure it. However, several models have been proposed. Various numbers of inputs have been considered. For example, a model of the burned gas fraction using in-cylinder pressure sensor is presented in [59] and in [64]. This sensor is not available in the application. Fox *et al.* propose in [17] a model of the residual gas fraction using exhaust pressure measurements. Although it is not directly usable here, this model, which introduces the notion of overlap factor, has inspired our work. This model has spurred strong interest in the community of engine modeling. Cavina *et al.* apply this model to a VVT engine in [6]. In [62], some comparisons are made between these models (in-cylinder pressure based models are of course more reliable). In [13], an artificial neural network is proposed to estimate the in-cylinder burned gas mass and the scavenged air mass using engine speed, intake manifold pressure and VVT actuators positions measurements. While accurate, this model is not usable in this case.

Here, in accordance to the requirements of the application (analytic model without any in-cylinder sensor), a model for both the aspirated air and the burned gas masses using only commercial sensors (engine speed, intake manifold pressure and VVA positions) is proposed. The model is based on first principles, and explicitly depends on engine geometrical characteristics and valves lifts profiles. In this way, the model is relatively versatile and can be used for many variable-valve-gear technologies and many engines (either SI or CI). Its analytical expressions are also real-time computable which is important for control applications. The model is built as follows. In Section 2.1, a general model of in-cylinder aspirated masses from the intake and from the exhaust is presented. In Section 2.2 and Section 2.3, this model is detailed on a turbocharged double VVT SI and a VLD CI engines. Experimental results are given for each application.

2.1 General analytic cylinder filling model

Figure 2.2 details the notations: P, T and m refer to pressure, temperature and mass respectively. int, exh and cyl refer to intake manifold, exhaust manifold, and cylinder, respectively. The in-cylinder variables are by definition the quantities at intake valve closing (ivc). Finally, $\dot{m}_{asp}^{int}$ and $\dot{m}_{asp}^{exh}$ are the mean mass flows going through the intake and the exhaust valves, respectively.

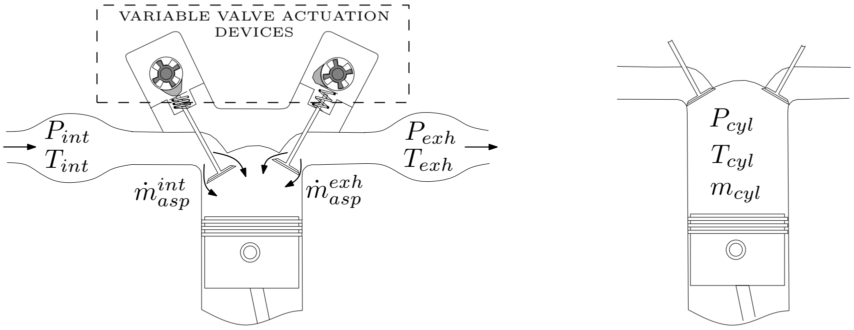

(a) Mass flows during the intake stroke.

(b) In-cylinder quantities at ivc.

Figure 2.2: Notation used in the cylinder filling model. In this section, all the intake and exhaust manifolds thermodynamics quantities for the general model design are used. It will be seen later that some exhaust quantities are in fact not measured in the application.

There is no sensor in the combustion chamber to evaluate the contained quantities of fresh air and burned gases. To calibrate and validate the model, it is needed to refer to remotely measured variables. On a test bench, it is possible to measure the aspirated mass (through the intake valve) under steady-state conditions. This information is given by a mass air flow sensor (referred to as MAF) located at the intake of the engine. Then, the aspirated mass coming from the intake, m_{asp}^{int} (which can be composed of only air, or be a blend of air and burned gases in case of EGR equipped engines), is expressed. This mass is given by the difference between the total mass inside the cylinder at ivc, m_{cyl}, and the aspirated mass coming from the exhaust, m_{asp}^{exh}. One has

$$m_{asp}^{int} = m_{cyl} - m_{asp}^{exh} \tag{2.3}$$

Now, physical expressions of the two terms in the right-hand side of equation (2.3) are given.

2.1.1 In-cylinder total mass at intake valve closing

The in-cylinder mass at *ivc* can be easily obtained using the ideal gas law in the combustion chamber. Note P_{cyl} and T_{cyl} the thermodynamic conditions of the mixture in the cylinder at *ivc*, one has

$$m_{cyl} = \frac{P_{cyl} V_{ivc}}{R T_{cyl}} \tag{2.4}$$

where R is the ideal gas constant, and V_{ivc} refers to the cylinder volume when the intake valve closes. *One should note that this last variable is sensitive to a variation of the intake valve profile.*

Now, it is assumed that the induction process is sufficiently long so that a pressure equilibrium is reached between the intake manifold and the cylinder. This means that the in-cylinder pressure, P_{cyl}, can be approximated by the intake manifold pressure, P_{int}. To account for the simplicity of this mean-value modeling, a correcting term α_1 is included in the expression (in the same spirit as in Equation (2.1) where a volumetric efficiency correcting term is used). This gives

$$m_{cyl} = \alpha_1 \frac{P_{int} V_{ivc}}{R T_{cyl}} \tag{2.5}$$

Remark 2.1.
If one considers the cylinder filling of a fixed-valve-gear engine, i.e. without any aspirated mass from the exhaust, model (2.5) represents the classic relationship giving the aspirated mass (see equation (2.2)). In this case, V_{ivc} *is a constant (value close to the displaced volume* V_d*), and* T_{cyl} *is approximately equal to the intake temperature (neglecting heat losses) because there is no hot exhaust gases recirculation. Finally, the correcting term* α_1 *represents the volumetric efficiency (*η_{vol}*).*

2.1.2 Aspirated mass coming from the exhaust

The aspirated gas mass coming from the exhaust is more complex to model than the total mass. It can be divided into two terms. First, a part of the aspirated mass coming from the exhaust is the quantity of gas flowing through both valves during the overlap. It models either the back-flow of burned gases towards the intake runner or the scavenged air towards the exhaust runner (depending on the sign of the pressure difference between the intake and the exhaust runners). Secondly, the other part of the aspirated mass from the exhaust is the exhaust gases remaining inside the cylinder or going back from the exhaust pipe into the cylinder[1]. Let us note $m^{exh}_{overlap}$ and m^{exh}_{evc} these two quantities, respectively. Then, one has

$$m^{exh}_{asp} = m^{exh}_{overlap} + m^{exh}_{evc} \tag{2.6}$$

Mass of gas flowing through both intake and exhaust valves

The mass of gas flowing through both the intake and exhaust valves when the crankshaft is close to the TDC (time when both valves can be opened together) is now modeled. One notes P_u, T_u, and P_d the upstream and downstream pressures and temperature (referring either to the intake manifold or to the exhaust), respectively. Then, for all $t \in [t_{ivo}, t_{evc}]$ (t_{ivo} and t_{evc} stand for the instant when the intake valve opens and the exhaust valve closes respectively), the instantaneous mass flow of gas through both valves is modeled by

$$\dot{m}^{exh}_{overlap}(t) = Area(t) \cdot \psi(P_u(t), P_d(t), T_u(t)) \tag{2.7}$$

where $Area$ defines the common opening area of both valves, and the function ψ models the mass flow rate [24]. Explicitly, one has

$$\begin{aligned}\psi(P_u(t),&P_d(t), T_u(t)) \\ &= \frac{P_u(t)}{\sqrt{RT_u(t)}} \begin{cases} \left(\frac{P_d(t)}{P_u(t)}\right)^{\frac{1}{\gamma}} \sqrt{\frac{2\gamma}{\gamma-1}\left(1-\left(\frac{P_d(t)}{P_u(t)}\right)^{\frac{\gamma-1}{\gamma}}\right)} & \text{, if } \frac{P_d(t)}{P_u(t)} > r_c \\ \sqrt{\gamma\left(\frac{2}{\gamma+1}\right)^{\frac{\gamma+1}{\gamma-1}}} & \text{, otherwise} \end{cases}\end{aligned}$$

where $r_c = (2/(\gamma+1))^{\gamma/(\gamma-1)}$ denotes the critical pressure ratio. By integrating (2.7) over the interval $[t_{ivo}, t_{evc}]$, one obtains

$$m^{exh}_{overlap} = \int_{t_{ivo}}^{t_{evc}} Area(t) \cdot \psi(P_u(t), P_d(t), T_u(t))dt \tag{2.8}$$

To simplify this formula, mean values of pressure and temperature upstream and downstream the restriction during the overlap are considered. Note $\overline{P_u}$, $\overline{P_d}$, $\overline{T_u}$ these mean values. A change of variable is performed, by considering the crankshaft angle θ instead of the time variable t, $d\theta = N_e \cdot dt$. Then, (2.8) rewrites

$$m^{exh}_{overlap} = \psi(\overline{P_u}, \overline{P_d}, \overline{T_u}) \frac{\overline{Area}}{N_e} \int_{\theta_{ivo}}^{\theta_{evc}} d\theta$$

---

[1] This depends on the *evc* position compared with TDC.

where the term $\overline{Area}$ is the area between both valves (see Figure 2.3)

$$\overline{Area} = \frac{1}{\theta_{evc} - \theta_{ivo}} \int_{\theta_{ivo}}^{\theta_{evc}} Area(\theta) d\theta$$

Figure 2.3 gives a schematic representation of the overlap area $\overline{Area}$.

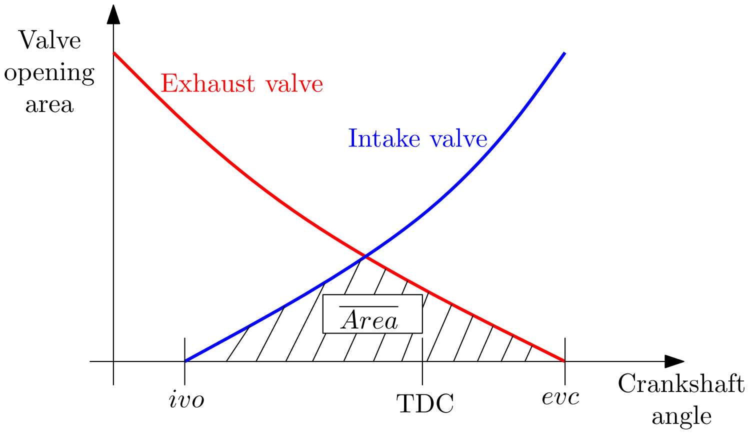

Figure 2.3: Intake and exhaust valves opening areas as a function of the crankshaft angle. $\overline{Area}$ is defined as the average opening area under both valves during the valve overlap.

Finally, the overlap factor (following [17]) is introduced

$$\text{OF} = \int_{\theta_{ivo}}^{\theta_{evc}} Area(\theta) d\theta \tag{2.9}$$

Then, the mass of gas flowing through both the intake and exhaust valves during the overlap is simply given by

$$m_{overlap}^{exh} = \psi(\overline{P_u}, \overline{P_d}, \overline{T_u}) \frac{\text{OF}}{N_e} \tag{2.10}$$

Remark 2.2.

Upstream and downstream thermodynamic variables either correspond to intake or exhaust quantities. Indeed, if the exhaust pressure is higher than the intake pressure, then $\psi(\overline{P_u}, \overline{P_d}, \overline{T_u}) = \psi(P_{exh}, P_{int}, T_{exh})$. *In this case, a positive flow may appear, i.e. some gases from the exhaust are reintroduced in the cylinder. This models the discussed* back-flow *process. Otherwise, when the intake pressure is higher than the exhaust pressure, then* $\psi(\overline{P_u}, \overline{P_d}, \overline{T_u}) = -\psi(P_{int}, P_{exh}, T_{int})$. *In this case, a negative flow may appear, i.e.*

some aspirated mass from the intake is directly driven to the exhaust. This models the scavenging *process.*

The mapping Ψ is introduced as a function of the intake and exhaust manifold pressures and temperatures

$$\Psi(P_{int}, P_{exh}, T_{int}, T_{exh}) = \begin{cases} \psi(P_{exh}, P_{int}, T_{exh}) & \text{, if } P_{int} < P_{exh} \\ -\psi(P_{int}, P_{exh}, T_{int}) & \text{, otherwise} \end{cases} \tag{2.11}$$

Again, to account for the simplicity of this mean-value model, a term α_2 is added in the expression which will be useful in the model calibration. Then, (2.10) becomes

$$m^{exh}_{overlap} = \alpha_2 \Psi(P_{int}, P_{exh}, T_{int}, T_{exh}) \frac{\text{OF}}{N_e} \tag{2.12}$$

Exhaust gas mass at exhaust valve closing

Similar to equation (2.4), the exhaust gas mass at *evc* can be easily obtained using the ideal gas law in the combustion chamber. Noting P_{evc} and T_{evc} the thermodynamic conditions of the mixture in the cylinder at *evc*, one has

$$m^{exh}_{evc} = \frac{P_{evc} V_{evc}}{R T_{evc}}$$

where R is the ideal gas constant and V_{evc} refers to the cylinder volume when the exhaust valve closes. Note that this variable is sensitive to a variation of the exhaust valve profile.

Again, the exhaust process is assumed to be sufficiently long so that a pressure equilibrium is reached between the exhaust manifold and the cylinder. This means that the in-cylinder pressure, P_{evc}, can be approximated by the exhaust manifold pressure, P_{exh}. We also assume that the temperature of the exhaust gases in the cylinder, T_{evc}, is equal to the temperature in the exhaust manifold, T_{exh}. To account for the simplicity of this mean-value model, a correcting term α_3 is included in the expression. This parameter will turn useful in the calibration of the model. Finally, this gives

$$m^{exh}_{evc} = \alpha_3 \frac{P_{exh} V_{evc}}{R T_{exh}} \tag{2.13}$$

2.1.3 Aspirated mass through the intake valve

The aspirated mass coming from the exhaust is the sum of the mass of gas going through both intake and exhaust valves during the overlap (2.12) and the exhaust gas mass at evc (2.13). Then, (2.6) gives

$$m_{asp}^{exh} = \alpha_2 \Psi(P_{int}, P_{exh}, T_{int}, T_{exh}) \frac{\mathrm{OF}}{N_e} + \alpha_3 \frac{P_{exh} V_{evc}}{R T_{exh}} \tag{2.14}$$

One can now compute the aspirated mass coming from the intake. Substituting (2.5) and (2.14) into (2.3) yields

$$m_{asp}^{int} = \alpha_1 \frac{P_{int} V_{ivc}}{R T_{cyl}} - \alpha_2 \Psi(P_{int}, P_{exh}, T_{int}, T_{exh}) \frac{\mathrm{OF}}{N_e} - \alpha_3 \frac{P_{exh} V_{evc}}{R T_{exh}} \tag{2.15}$$

Finally, the in-cylinder temperature at ivc, T_{cyl}, is modeled as the mass-weighted average of the temperatures of the flows contributing to the trapped mass m_{cyl} (assuming that all the specific heats are the same for air and burned gas)

$$T_{cyl} m_{cyl} = T_{int} m_{asp}^{int} + T_{exh} m_{asp}^{exh} \tag{2.16}$$

Replacing respectively m_{cyl} and m_{asp}^{exh} by their expressions (2.5) and (2.14) and using model (2.16) into (2.15), one can obtain the aspirated mass from the intake as a function of intake and exhaust manifold thermodynamic conditions, engine speed and valve-gear

$$m_{asp}^{int} = \alpha_1 \frac{P_{int} V_{ivc}}{R T_{int}} - \alpha_2 \Psi(P_{int}, P_{exh}, T_{int}, T_{exh}) \frac{\mathrm{OF}}{N_e} \frac{T_{exh}}{T_{int}} - \alpha_3 \frac{P_{exh} V_{evc}}{R T_{int}} \tag{2.17}$$

Together with (2.14), this last equation (2.17) is the general model considered for the cylinder filling process.

2.2 Cylinder filling model for turbocharged VVT SI engines

In this section, the general model (2.14)-(2.17) is further detailed for the case of turbocharged SI engine equipped with double VVT actuators. Analysis of the impact of the VVT actuators on the intake process is made using a reference high frequency simulator. Then, the model of the masses is presented and some experimental results are given. This model uses only commonly available sensors, at the expense of a simplification of (2.14)-(2.17) which is detailed.

2.2.1 High frequency analysis

To highlight flows exchanges between the intake and exhaust manifolds and the cylinder, we use a reference high-frequency simulator developed on an Amesim^{TM} platform [42]. Figure 2.4 presents simulated mass flow rates for two positions of the intake VVT actuator (large and small overlap, see Figure 2.4(a)) for two engine operating points (low load and high load).

Figure 2.4(b) reports instantaneous cylinder flows going through the intake and exhaust valves for a 0.4 bar mean-value intake manifold pressure and a 1.1 bar mean-value exhaust manifold pressure. In the case of a small overlap, intake and exhaust processes are completely decoupled, i.e. there is no gas exchange between the intake and the exhaust manifolds. There is no IGR at that operating point. In the case of a larger overlap, intake and exhaust processes are not decoupled any more. Because of the low value of the intake manifold pressure (referring to low load), some exhaust gases previously expelled towards the exhaust are reintroduced into the cylinder, and a part of it goes through the intake valve towards the intake runner (see the negative mass flow through the intake valve). This is the back-flow phenomenon discussed in Section 1.2.3. In the proposed model (2.17), the second term represents this phenomenon. The higher the pressure difference between the intake and the exhaust manifolds is, the higher the quantity of burned gases reintroduced in the cylinder is and the lower the aspirated mass from the intake (function Ψ increases) is too.

Figure 2.4(c) shows cylinder flows for a 2 bar mean-value intake manifold pressure, and a 1.8 bar mean-value exhaust manifold pressure. The main differences for both intake and exhaust mass flow rates can be observed during the overlap phase. The intake and exhaust mass flows are larger when the overlap is positive: fresh air goes directly from the intake to the exhaust manifold. This is the scavenging phenomenon discussed in Section 1.2.3. In the proposed model (2.17), the second term also accounts for this phenomenon. The higher the pressure difference between the intake and exhaust manifolds is, the higher the quantity of fresh air scavenged directly towards the exhaust and the aspirated mass from the intake (function Ψ is negative - see (2.11) - and its absolute value increases) are.

2.2.2 Aspirated masses mean-value model

In view of applications, the developed models have to only use commercial sensors, and, further, must be real-time computable. However, the exhaust thermodynamic variables (which are not measured on a vehicle) are used in the computation of

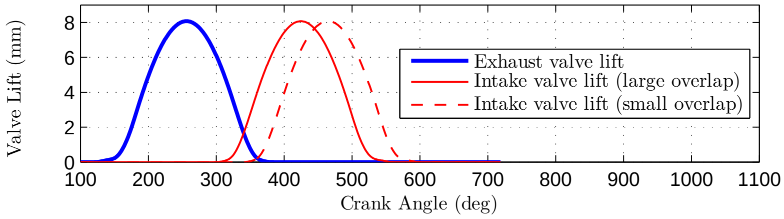

(a) Intake and exhaust valve lift profiles.

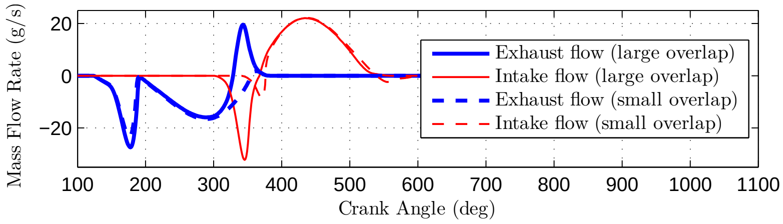

(b) Part load ($P_{int} = 0.4$ bar).

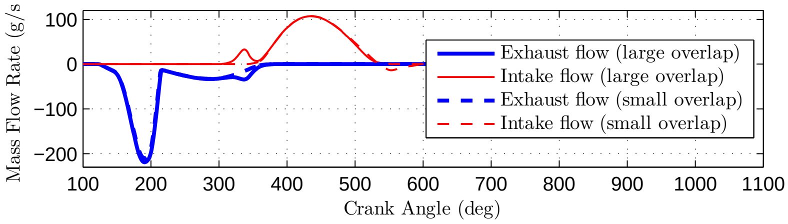

(c) High load ($P_{int} = 2$ bar).

Figure 2.4: Amesim$^{\text{TM}}$ simulator results. Instantaneous flows through intake and exhaust valves for two different valve overlap at part and high load.

model (2.14)-(2.17). This lack of information can be compensated for by the three tuning parameters (α_1, α_2 and α_3) that we chose to be functions of the engine speed and the intake manifold pressure. Using models (2.14) and (2.17), the mean-value model of the aspirated masses from the intake and the exhaust writes

$$\left\{\begin{aligned} m_{asp}^{int} &= \alpha_1(N_e, P_{int})\frac{P_{int}V_{ivc}(\Phi_{int})}{RT_{int}} - \alpha_2(N_e, P_{int})\frac{\text{OF}(\Phi_{exh} - \Phi_{int})}{N_e} \\ &\qquad - \alpha_3(N_e, P_{int})V_{evc}(\Phi_{exh}) \\ m_{asp}^{exh} &= \alpha_2(N_e, P_{int})\frac{\text{OF}(\Phi_{exh} - \Phi_{int})}{N_e} + \alpha_3(N_e, P_{int})V_{evc}(\Phi_{exh}) \end{aligned}\right. \tag{2.18}$$

where α_1, α_2 and α_3 are functions of the intake manifold pressure P_{int}, and the engine speed N_e[2]. Here, V_{ivc} is the cylinder volume at ivc, which is a function of the intake valve timing, Φ_{int}. Similarly, V_{evc} is the cylinder volume at evc. It is a function of the exhaust valve timing, Φ_{exh}. At last, the overlap factor OF is a function of both the intake and the exhaust valve timings, Φ_{int} and Φ_{exh} (see (2.9)). These three functions are completely known because they are functions of the valve-gear profiles and of some available engine geometrical data. These functions are pictured in Figure 2.5.

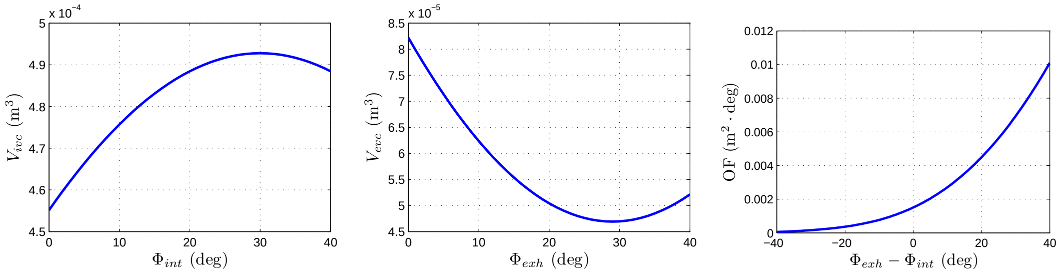

(a) In-cylinder volume at *ivc*. (b) In-cylinder volume at *evc*. (c) Overlap factor.

Figure 2.5: Modeling parameters functions of the VVT actuators positions.

Figure 2.6 illustrates the various effects accounted for by the cylinder filling model.

Summary of the model simplifications Simplifications have been made from the models (2.14)-(2.17) to the model (2.18). They are now detailed for sake of clarity. In the second term, the Ψ function has been removed because no exhaust pressure is measured. It is now lumped in the α_2 term. A similar simplification has been made in the third term. Another difference is that the aspirated mass from the exhaust, m_{asp}^{exh}, should be equal to the sum of the second and third terms of the aspirated mass from the intake multiplied by the ratio T_{int}/T_{exh} (following faithfully the model (2.14)). In (2.18), because the exhaust temperature measurement is missing, this ratio cannot be computed. As a result, the modeled aspirated mass from the exhaust is higher than it is in reality (because the exhaust temperature is always higher than the intake one). However, an exhaust temperature model based on combustion modeling could be used in the case when the absolute burned gas quantity value is necessary. Later-on, we will see that this information is necessary for CI engine applications since the in-cylinder temperature is an important variable for the combustion. This is not really the case in SI engines.

---

[2] These two variables being the available measurements which characterize the operating point in fixed-valve timing SI engines (see the classical speed-density equation (2.1)).

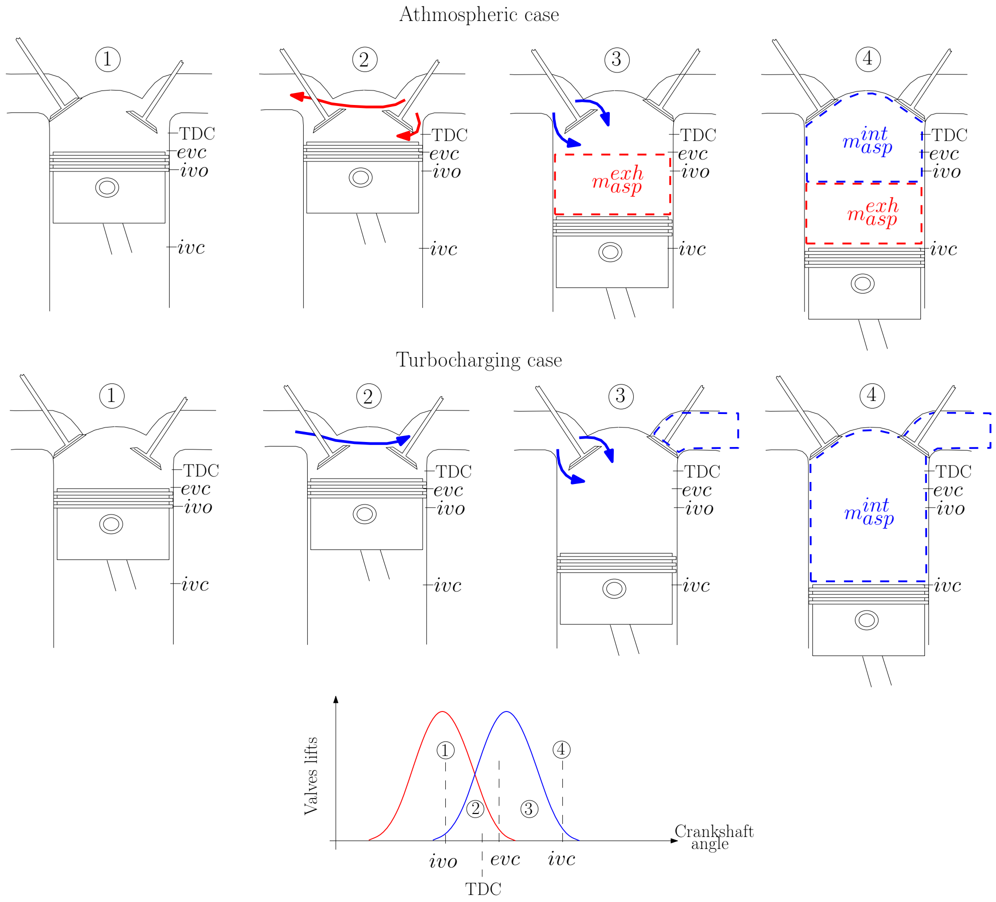
Athmospheric case
①
②
③
④
TDC
evc
ivo
ivc
m_{asp}^{exh}
m_{asp}^{int}
Turbocharging case
Valves lifts
Crankshaft angle
ivo
evc
ivc
TDC

Figure 2.6: Cylinder filling process under atmospheric and turbocharging conditions. 1: Intake valve opens. 2: Both intake and exhaust valves are open, back-flow of burned gases (respectively scavenging of fresh air) can be observed in the atmospheric (turbocharging) case. 3: exhaust valve closes, the rest of the cylinder volume is filled with intake fresh air. 4: end of the intake stroke (notice that part of the aspirated air mass is not contained in the cylinder in the turbocharging case because of the scavenging phenomenon).

Remark 2.3.

The total mass of air contained in the cylinder at ivc is equal to the aspirated mass from the intake. Indeed, the aspirated air mass from the intake, m_{asp}^{int}*, is only composed of fresh air since the engine under consideration is not equipped with any EGR capability. Also, the aspirated air mass from the exhaust,* m_{asp}^{exh}*, is only composed of burned gases because of the stoichiometric combustion in SI engines.*

2.2.3 Experimental data

The representativeness of the proposed model (2.18) needs to be evaluated comparing to real data. The engine under consideration is a 1.8L four-cylinder SI engine using direct injection and homogeneous combustion. The air path consists of a turbocharger and two VVT devices, for intake and exhaust valves. This engine is of the type pictured in Figure 1.4.

To calibrate and validate the model, an extended range of operating points has been studied. The measurements cover engine speeds from 750 rpm to 3000 rpm, from zero to full load. The VVT positions are selected on an equally spaced 9 × 9 grid (see Table 2.1). Steady state tests have been conducted for each combination, producing results for a total of more than 3000 test points.

Data	**Unit**	**Operating range**	**Step size**
Engine speed	rpm	750 to 3000	500
Intake manifold pressure	bar	0.4 to 2	0.2
Intake VVT actuator position	deg	0 to 40	5
Exhaust VVT actuator position	deg	0 to 40	5

Table 2.1: Test bench data.

For each operating point, the aspirated mass determined from the air-flow meter (MAF) information is stored. To obtain the aspirated mass from the MAF sensor, the signal is integrated over one engine cycle

$$m_{MAF} = \dot{m}_{MAF} \frac{2 \times 60}{N_e n_{cyl}} \tag{2.19}$$

2.2.4 Model calibration

The three look-up tables α_1, α_2 and α_3 appearing in (2.18) are determined as follows. Each point of the look-up tables (constant intake manifold pressure and constant engine speed) is obtained by fitting model (2.18) on experimental measurements (2.19), through a classic least-squares linear regression. Only 3 intake and exhaust VVT actuators positions are considered, i.e. 9 combinations for each engine working point (the rest of the experimental points will be used for the model validation). From (2.18), one can note

$$\boldsymbol{y} = \boldsymbol{A\alpha}$$

with

$$\boldsymbol{y} = \begin{pmatrix} m_{MAF}(1) \\ \cdots \\ m_{MAF}(n) \end{pmatrix}, \ \boldsymbol{\alpha} = \begin{pmatrix} \alpha_1 \\ \alpha_2 \\ \alpha_3 \end{pmatrix} \text{ and}$$

$$\boldsymbol{A} = \begin{pmatrix} \frac{P_{int}(1)V_{ivc}(\Phi_{int}(1))}{RT_{int}(1)} & \frac{\mathrm{OF}(\Phi_{exh}(1)-\Phi_{int}(1))}{N_e} & V_{evc}(\Phi_{exh}(1)) \\ \cdots & \cdots & \cdots \\ \frac{P_{int}(n)V_{ivc}(\Phi_{int}(n))}{RT_{int}(n)} & \frac{\mathrm{OF}(\Phi_{exh}(n)-\Phi_{int}(n))}{N_e} & V_{evc}(\Phi_{exh}(n)) \end{pmatrix}$$

where n defines the number of experiments for each operating point (here, $n = 9$, number of combinations of VVT actuators positions). Finally, look-up tables α_1, α_2 and α_3 are obtained using the pseudo-inverse

$$\boldsymbol{\alpha} = (\boldsymbol{A}^T\boldsymbol{A})^{-1}\boldsymbol{A}^T\boldsymbol{y}$$

Figure 2.7 presents the obtained results. The three look-up tables are smooth. Depending on the operating point under consideration, the second parameter α_2 is either negative or positive. This is because the function Ψ defined in (2.11) (which is here included in parameter α_2) is positive when the pressure difference between the intake and exhaust manifold is negative, and, on the other hand, is negative when the pressure difference is positive (see Figure 2.7(b)). These observations are consistent with the discussion of Section 2.2.1. Notice also that the coefficient α_1 is consistent with a classic volumetric efficiency look-up table (see Figure 2.7(b)).

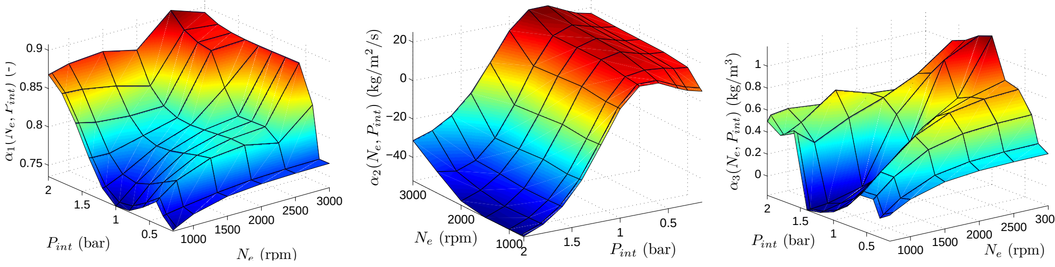

(a) Look-up table α_1.
(b) Look-up table α_2.
(c) Look-up table α_3.

Figure 2.7: Look-up tables for the cylinder filling model parameters.

2.2.5 Comparisons with experimental data

Figure 2.8 shows the representativeness of the model on experimental data on a particular engine operating point ($N_e = 2000$ rpm and $P_{int} = 0.6$ bar). Figure 2.8(a) represents intake and exhaust VVT actuators variations realized at this working point. Figure 2.8(b) compares the aspirated mass from the intake coming from the MAF sensor (reference bench data) and the model (2.18). To highlight the relevance of the three terms, the figure compares three model structures of increasing complexity. The first one (green curve) is obtained using only the first term of model (2.18). It corresponds to a classic model of the aspirated air mass (2.1), α_1 being the volumetric efficiency. It does not capture any VVT actuator variation. The second one (black curve) incorporates the overlap term in the modeling. Here, the major trends are captured. When the overlap increases, the aspirated air mass decreases. Adding the third term in the model (red curve) permits to capture all the variations. Indeed, when the exhaust valve closes before the TDC (VVT actuator position being near to zero), some exhaust gases remain trapped inside the cylinder. This reduces the aspirated air mass.

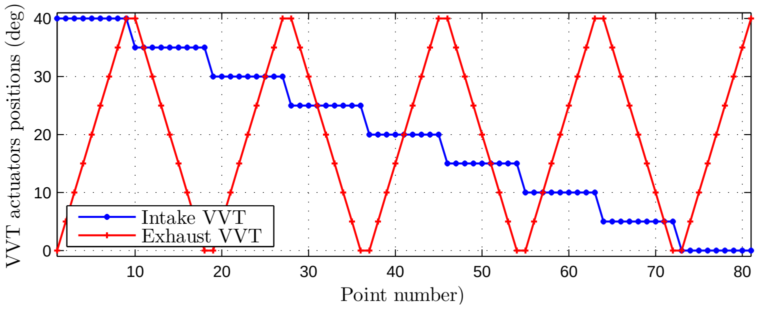

(a) VVT actuators positions.

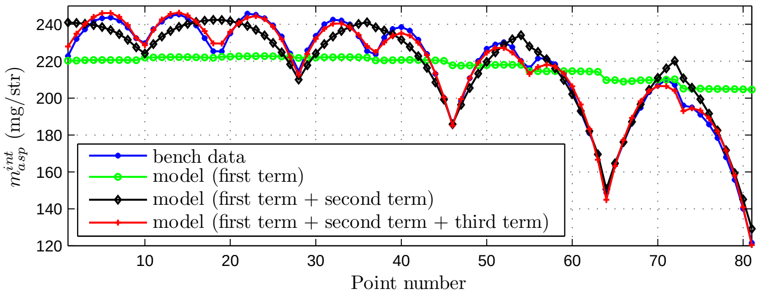

(b) In-cylinder aspirated mass from intake.

Figure 2.8: Comparison between modeled and experimental aspirated air mass. Constant engine operating point ($P_{int} = 0.6$ bar and $N_e = 2000$ rpm), intake and exhaust VVT actuators positions variations.

Figure 2.9 compares model (2.18) against experimental data on the whole data set (see Table 2.1). The maximum relative error is less than 5%.

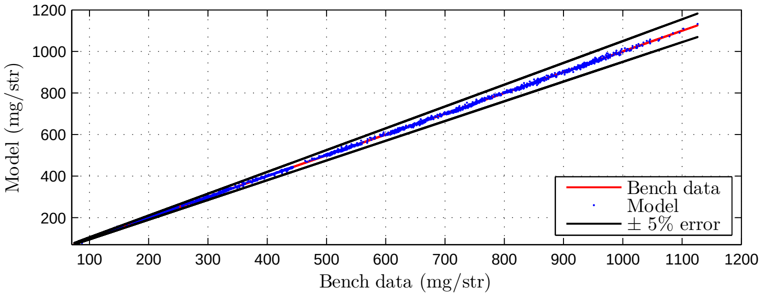

(a) Comparisons between modeled and experimental aspirated air mass.

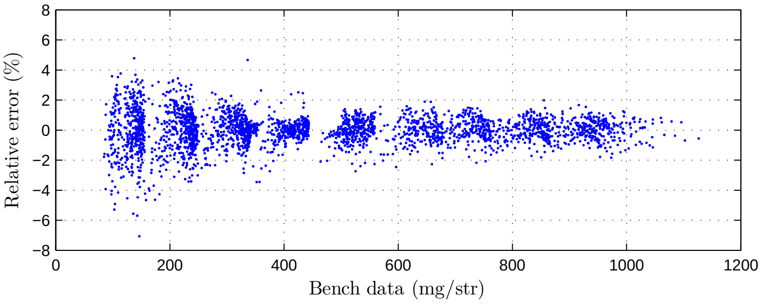

(b) Relative error.

Figure 2.9: Comparisons between modeled and experimental aspirated air mass over more than 3000 points (P_{int} from 0.3 to 2 bar, N_e from 750 to 3000 rpm and all intake and exhaust VVT actuators positions).

By contrast with the aspirated mass from the intake, the aspirated mass from the exhaust, m_{asp}^{exh}, is almost impossible to measure. Yet, its effect on pollutants can be observed, and provide indirect information. Representativeness of the model is highlighted in Figure 2.10. When the estimated quantity of burned gases in the cylinder increases (m_{asp}^{exh} is only composed of burned gases because of the stoichiometric combustion), at constant torque (constant in-cylinder air mass), NO_x emissions are lowered. This decrease is consistent with the experimental results reported in [24].

2.3 Cylinder filling model for VLD CI engines

In this section, the general model (2.14)-(2.17) is considered for a CI engine equipped with exhaust VLD actuator allowing a second lift of the exhaust valve during the intake process. It is first analyzed the impact of the VLD actuator on the intake process using

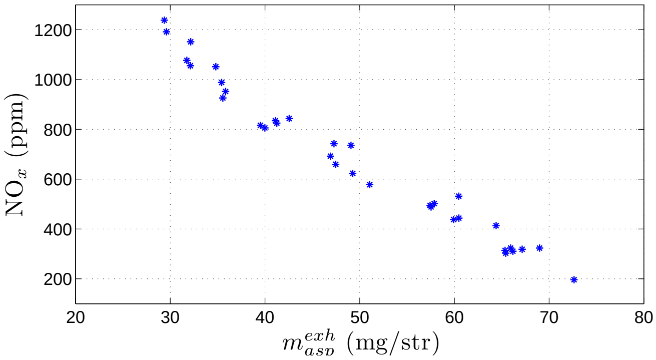

Figure 2.10: Experimental NO$_x$ emissions function of estimated aspirated mass from the exhaust at constant torque. Emissions decrease with the increase of the in-cylinder burned gas fraction [24].

a reference high frequency simulator, and, then, the model of the masses is presented and simulation and experimental results are given.

2.3.1 High frequency analysis

To highlight flows exchanges between the intake and exhaust manifolds and the cylinder, we use the reference high-frequency simulator developed on the Amesim$^{\text{TM}}$ platform [2] again. Figure 2.11 represents the instantaneous flows going in and out of the cylinder, during exhaust and intake phases. Intake and exhaust valves lifts profiles are given in Figure 2.11(a). Using the VLD actuator permits a large re-opening of the exhaust valve. Figure 2.11(b) shows that, before the TDC, in-cylinder residual gases are expelled towards the exhaust runner (negative flow). Then, the intake valve opens, and the exhaust valve re-opens while the piston begins to go down. Fresh mixture is aspirated into the cylinder through the intake valve. Meanwhile, exhaust gases are re-aspirated into the cylinder, through the exhaust valve.

2.3.2 Aspirated masses mean-value model

As for the SI application in Section 2.2, the designed model for the CI application has to only use commercial sensors, and has to be consistent with real-time requirements. In this application, besides measuring the engine speed, the intake pressure and temperature and the VLD actuator position, the pressure in the exhaust manifold is also measured. The missing exhaust temperature could be compensated for by the tuning parameters as was done in the SI application. However, the aspirated mass from the exhaust permits estimation of the in-cylinder burned gas rate which is an essential variable for CI engine control purpose. It is then necessary to estimate the exhaust

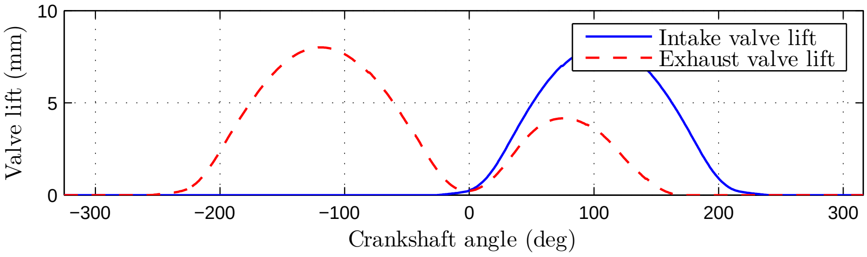

(a) Intake and exhaust valve lift profiles.

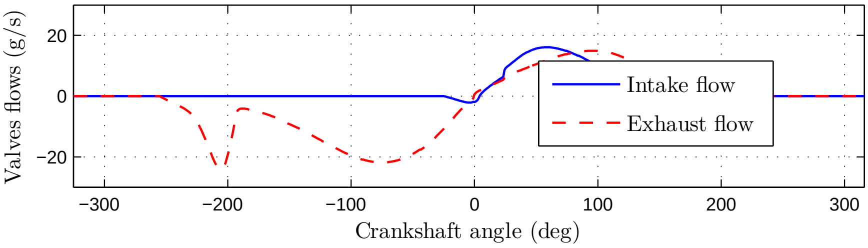

(b) Instantaneous flows going in and out of the cylinder.

Figure 2.11: Amesim^{TM} simulator results. Instantaneous flows through intake and exhaust valves for a large exhaust valve re-opening.

temperature. Such a model will be presented in Section 4.1.2. Using models (2.14) and (2.17), the model of the aspirated masses from the intake and the exhaust writes

$$\begin{cases} m_{asp}^{int} = \alpha_1(N_e)\dfrac{P_{int}V_{ivc}}{RT_{int}} - \alpha_2(N_e)\dfrac{P_{exh}V_{evc}(\Phi_{vld})}{RT_{int}} \\ m_{asp}^{exh} = \alpha_2(N_e)\dfrac{P_{exh}V_{evc}(\Phi_{vld})}{RT_{exh}} \end{cases} \tag{2.20}$$

where α_1 and α_2 are functions of the engine speed, N_e[3]. V_{evc} is the cylinder volume at exhaust valve closing (evc). It is a function of the VLD actuator, Φ_{vld}. Again, this function is completely known because it is a function of the valve-gear profiles and some engine geometrical data. It is pictured in Figure 2.12.

Figure 2.13 pictures the various effects accounted for in the cylinder filling model (2.20). It is clear that some simplifications have been made between models (2.14)-(2.17) and model (2.20). Indeed, we have neglected the second term of model (2.17), considering that the aspirated mass coming during the overlap is negligible (because

---

[3] The terms α_1 and α_2 can also be functions of the intake or exhaust pressure. However, since we only consider part load in the study, the intake and exhaust pressures are near to the atmospheric pressure, and are not considered in the present calibration of α_1 and α_2.

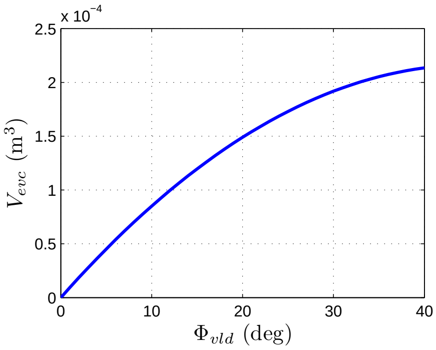

Figure 2.12: Modeling the V_{evc} parameter function of the VLD actuator position.

the pressure difference between intake and exhaust manifolds is almost null at low load in CI application).

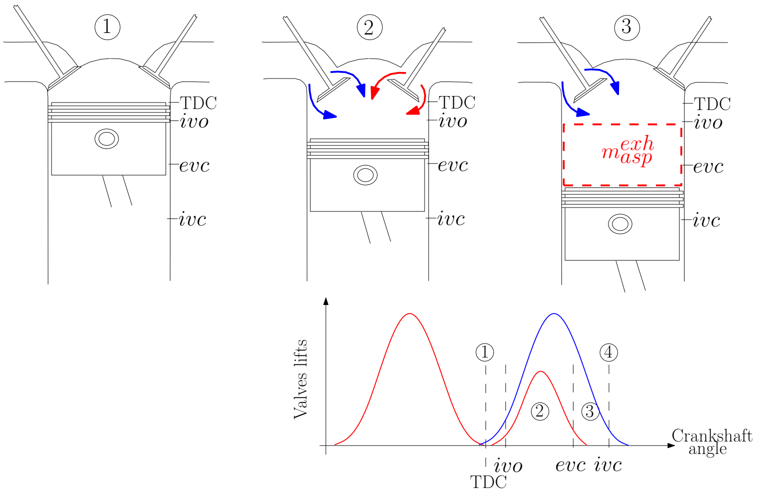

Figure 2.13: Cylinder filling process. 1: piston is at TDC, end of the exhaust stroke. 2: piston starts to go down, both intake and exhaust valves open, gases are admitted from both sides. 3: exhaust valve closes, the rest of the cylinder volume is filled with intake mixture (fresh air and burned gases from EGR). 4: end of the intake stroke, total in-cylinder mass of gas at *ivc*, m_{cyl}, is equal to the aspirated mass from the intake, m_{asp}^{int}, plus the mass of gas coming from IEGR, m_{asp}^{exh}.

Remark 2.4.

Contrary to the SI engine case, both the aspirated masses from the intake and from the exhaust valves are composed of air and burned gases. Indeed, EGR brings burned gases towards the intake, and lean combustion allows presence of air in the combustion residual gases.

2.3.3 Experimental data

Representativeness of the model (2.20) is investigated using real data. The engine under consideration is a 1.6L four-cylinder CI engine. The air path consists of a turbocharger, a LP EGR capability, and a VLD device allowing a second exhaust valve lift.

To calibrate and validate the model, an extended range of operating points has been studied. The measurements cover engine speeds from 800 rpm to 2500 rpm, under zero to partial load. The VLD position is selected on an equally spaced mesh (see Table 2.2). Steady state tests have been conducted for every possible combination, producing results for a total of more than 150 test points.

Data	Unit	Operating range	Step size
Engine speed	rpm	800 to 2500	500
IMEP	bar	2 to 6	1
VLD actuator position	deg	0 to 40	5

Table 2.2: Test bench data.

Again, for each operating point, the MAF information is captured. To obtain the aspirated mass from the MAF sensor, the signal is integrated over one engine cycle (as in Equation (2.2)),

$$m_{MAF} = \dot{m}_{MAF} \frac{2 \times 60}{N_e n_{cyl}} \tag{2.21}$$

2.3.4 Model calibration

Similarly to Section 2.2.4, the two look-up tables α_1 and α_2 are determined as follows. Each point of the look-up tables (constant engine speed) is obtained by fitting model (2.20) on experimental measurements (2.21), through a classic least-squares linear regression. Only three VLD actuator positions per engine working point are considered. From Equation (2.20), one can note

$$\boldsymbol{y} = \boldsymbol{B\alpha}$$

with

$$\boldsymbol{y} = \begin{pmatrix} m_{MAF}(1) \\ \cdots \\ m_{MAF}(n) \end{pmatrix}, \ \boldsymbol{\alpha} = \begin{pmatrix} \alpha_1 \\ \alpha_2 \end{pmatrix} \text{ and } \boldsymbol{B} = \begin{pmatrix} \frac{P_{int}(1)V_{ivc}}{RT_{int}(1)} & \frac{P_{exh}(1)V_{evc}(\Phi_{vld}(1))}{RT_{exh}(1)} \\ \cdots & \cdots \\ \frac{P_{int}(n)V_{ivc}}{RT_{int}(n)} & \frac{P_{exh}(n)V_{evc}(\Phi_{vld}(n))}{RT_{exh}(n)} \end{pmatrix}$$

where n defines the number of experiments for each operating point (here, $n = 3$, which is the number of VLD actuator positions). Finally, look-up tables α_1 and α_2 are obtained from the pseudo-inverse

$$\boldsymbol{\alpha} = (\boldsymbol{B}^T\boldsymbol{B})^{-1}\boldsymbol{B}^T\boldsymbol{y}$$

2.3.5 Comparisons with experimental data

Figure 2.14 compares model (2.20) against data measured at test bench for varying IMEP and VLD actuator positions at constant engine speed (1500 rpm). Figure 2.14(a) and Figure 2.14(b) represent VLD actuator and IMEP variations respectively. Figure 2.14(c) and Figure 2.14(d) represent modeled and measured aspirated mass from the intake, and the modeled aspirated mass from the exhaust, respectively. One can note the influence of the in-cylinder volume at *evc* (see Figure 2.12). Indeed, when the second exhaust valve lift increases (VLD actuator position increases), the available volume for residual gases increases too, and, in turn, the aspirated mass coming from the intake decreases. Note that there is a very weak influence of the IMEP variation on the aspirated mass. Actually, the intake and exhaust pressures are relatively close to the atmospheric pressure (for these engine operating points), and, then, do not have any impact on the cylinder charge. On the other hand, IMEP variations have a non-negligible impact on the exhaust temperature, and, then, on the aspirated mass coming from the exhaust.

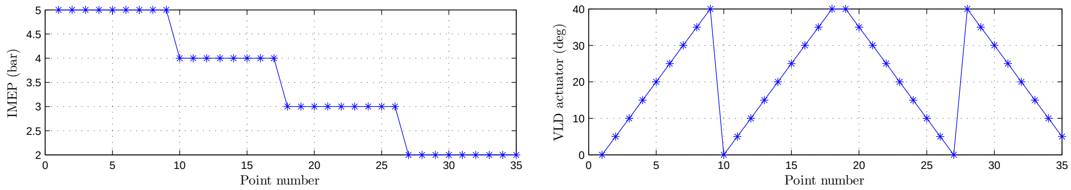

(a) IMEP variation.

(b) VLD variation.

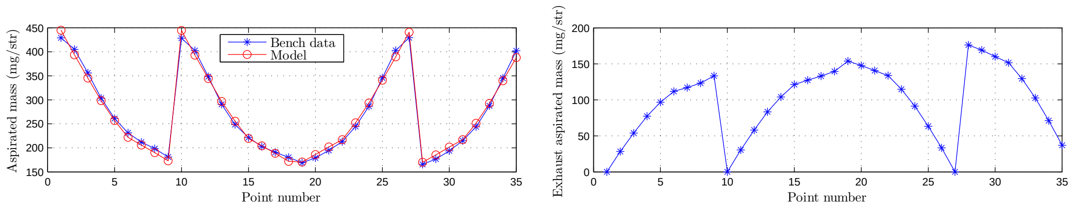

(c) Comparisons between modeled and experimental aspirated mass from the intake.

(d) Aspirated mass from the exhaust.

Figure 2.14: Comparisons between modeled and experimental aspirated mass at constant engine speed (1500 rpm).

Figure 2.15 compares the model (2.20) against experimental data on the whole data set (see Table 2.2). A vast majority of the tested operating points have maximum relative error under 5%.

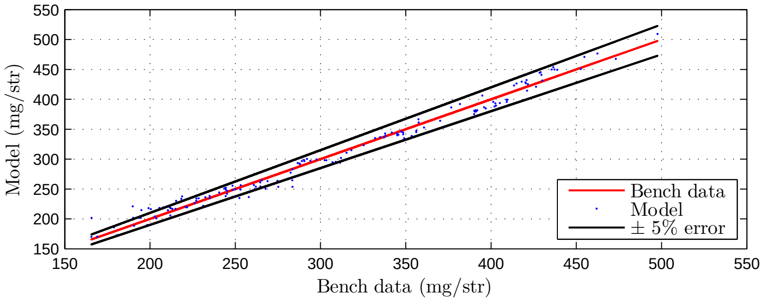

(a) Comparisons between modeled and experimental aspirated mass.

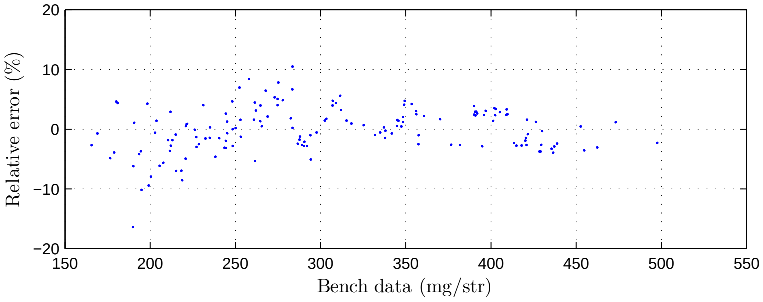

(b) Relative error.

Figure 2.15: Comparisons between modeled and experimental aspirated mass over about 150 points (IMEP from 2 to 6 bar, N_e from 800 to 2500 rpm and all VLD actuator positions).

The aspirated mass model (2.20) will be used later-on to estimate the in-cylinder BGR which is a key control variable for CI engine control. This modeling, taking into account the intake manifold BGR (brought by the external EGR circuit), will be discussed in Chapter 4. To check the model consistency, one may analyze the NO_x emissions when the in-cylinder BGR is varied. Figure 2.16 presents the NO_x emissions as a function of the in-cylinder BGR for different intake manifold BGR levels at constant engine speed.

2.4 Conclusion

In this chapter, two (static) models have been derived for the cylinder filling phenomenon in SI (Eq. (2.18)) and CI (Eq. (2.20)) engines, respectively. They use the

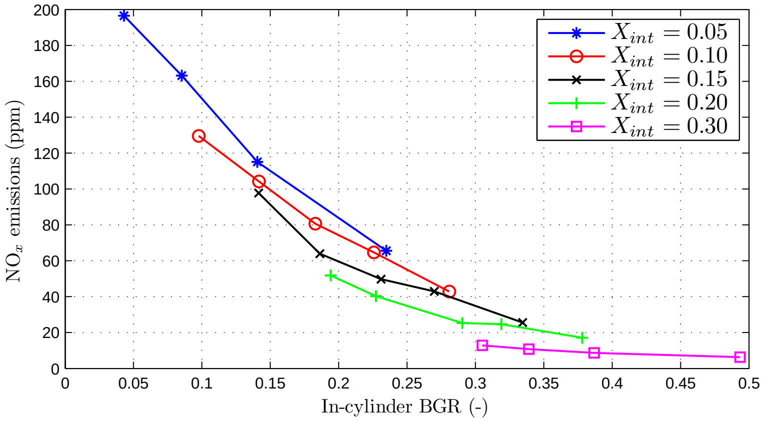

Figure 2.16: NO$_x$ emissions function of the in-cylinder BGR, for different intake manifold BGR levels, X_{int}, at constant engine speed (2000 rpm).

intake and exhaust manifold quantities, and stress the role of the valve lift profiles. The aspirated mass model consists of three terms. The first term expresses the classical speed-density relationship used in fixed-valve gear engines. The second term models the impact of the gas exchange between both intake and exhaust manifolds while the two valves are simultaneously open (overlap). Finally, the third term models the impact of the residual gases coming from a variation of the exhaust valve closing.

Two cases of study have been analyzed: a double VVT equipped SI engine, and a second exhaust valve re-opening capability CI engine. These analytic models involve look-up tables that are obtained through classic identification procedures from test bench data. Once these models, which stem from first principles, are calibrated, they can be used to predict the mass flow rates of fresh air and burned gas aspirated into the cylinder for any valve gear, using *only commonly available sensors* (intake manifold pressure and temperature, engine speed and positions of the variable valve gear actuators). Extensive experimental results have stressed the representativeness of these models in the two cases under consideration in this thesis (SI and CI engines).

In the next two chapters, this cylinder breathing model is used to quantitatively determine a cylinder filling control strategy.

Chapter 3

Case study 1: VVT turbocharged SI engines control

In this chapter, a controller is proposed to handle air path transients of a (general) VVT equipped SI engine, taking into account the various, and, as discussed in Chapter 1, *inconsistent in terms of speed of convergence*, dynamics present in the system. The considered engine setup is pictured in Figure 3.1.

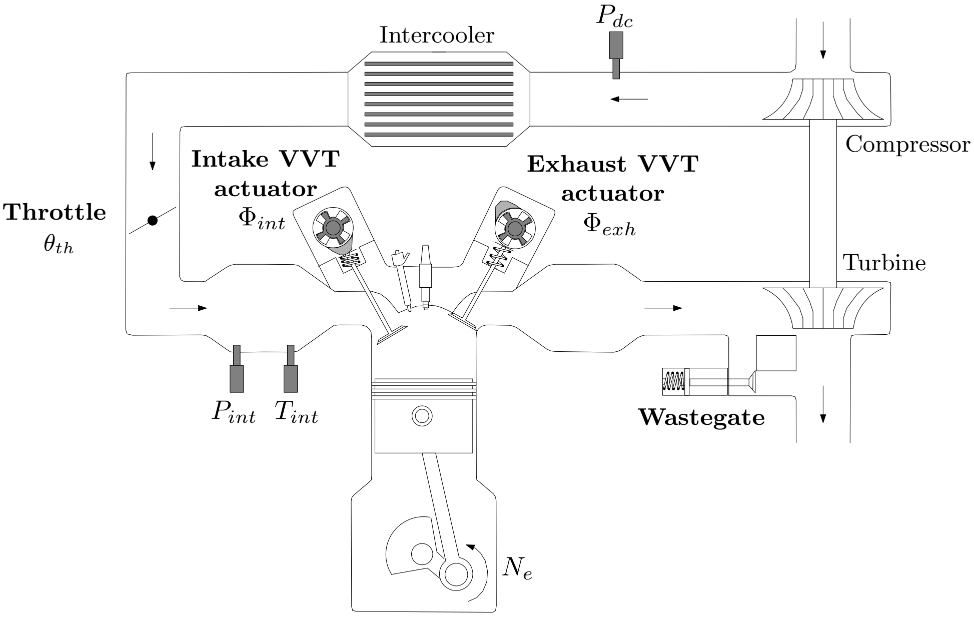
Intercooler
P_{dc}
Compressor
Intake VVT actuator
Φ_{int}
Exhaust VVT actuator
Φ_{exh}
Throttle
θ_{th}
Turbine
P_{int}
T_{int}
Wastegate
N_e

Figure 3.1: Schematic illustration of a turbocharged, VVT-equipped SI engine. The intake manifold pressure and temperature P_{int} and T_{int} and the downstream compressor pressure P_{dc} are measured by sensors. θ_{th} is the angular position of the throttle, Φ_{int} and Φ_{exh} are the positions of the VVT actuators.

In SI engines, the engine torque output is directly related to the fresh air charge contained in the cylinder[1]. It is then absolutely necessary to manage the *aspirated air mass* well. In the literature, controlling the aspirated air mass in presence of VVT actuators has been addressed as follows. In [61], the invention considers control of the valve timing in presence of a cylinder pressure sensor, which is not the case in the application. In [71], the invention corrects the value of intake valve closing when the intake manifold pressure is considered as erroneous (sensor default). In [25, 74], a dynamic camshaft-scheduling technique based on throttle position and engine speed has been presented. A torque response similar to that of a fixed-valve-timing engine can be obtained. In [26, 27, 30], VVT actuators are seen as a disturbance of the in-cylinder air mass control. This disturbance is taken into account in the throttle control strategy. In these approaches, valve-timing devices are seen as a static function of the engine operating point. Specifically, a direct compensation of VVT positions is performed by means of the throttle. This strategy is relevant under atmospheric conditions, but does not address the case of turbocharged conditions.

As previously mentioned, in these approaches from the literature, the VVT actuators are seen as disturbances, and are not part of the control strategy. However, using this left-over degree of freedom for controlling an extra control objective could be useful in an attempt to move forward in the direction of combustion control. In [80], the invention is about compensating the presence of burned gases by changing the intake valve closing timing in a camless engine (the intake pressure is equal to the atmospheric value because of the absence of any throttle or turbocharger). This application is different from the one under considertion in this work that uses slower hydraulic cam timing actuators. Moreover, in the case under consideration in this thesis, the cylinder filling is also impacted by the intake manifold pressure. In [14], it is proposed to control the so called *Internal Gas Recirculation (IGR) mass.* Certainly, the IGR mass is equivalent, *at steady state*, to the VVT actuator positions. Instead of the VVT positions, the high-level control objective should be the IGR mass, because it directly impacts on the combustion, and, therefore, on pollutant emissions.

To address an accurate control of the in-cylinder quantities, the model presented in the previous chapter is now used. It permits the relation of the high-level control variables (aspirated air mass and IGR mass) and the low-level variables (intake manifold pressure and VVT actuators positions). The proposed strategy coordinates the two low-level control subsystems to improve the overall performance. When the VVT actuators are slow, the controller adjusts the intake manifold set point to speed up the air-feeding process, so that the aspirated air mass is satisfied. Conversely, under turbocharging conditions, the controller uses the VVT to compensate the slow response of the intake manifold pressure due to the turbocharger inertia, so that the IGR mass objective is reached. Interestingly, accelerating the response of the IGR mass also accelerates the response of the aspirated fresh-air mass (by increasing the scavenging process). Explicitly, set points for the two low-level controllers are determined in real time, based on measurements of the intake manifold pressure and the VVT actuator positions. It is important to note that the same control strategy operates under both atmospheric and turbocharging conditions, even if the fast and slow variables of the system are not the same in these two operating areas. Difficulties arising while changing the operating area are also considered. This model-based controller is now detailed.

---

[1] Assuming a tight stoichiometric air/fuel ratio and spark control loop.

3.1 Model properties

The proposed controller is derived from the engine breathing model (2.18) of Chapter 2. The variables of interest (the aspirated air mass, m_{asp}, and the IGR mass, m_{igr}) are the two outputs of the model (2.18), m_{asp}^{int} and m_{asp}^{exh}. Indeed, for this SI engine application, there is no external EGR, thus the gases flowing into the cylinder through the intake valve are only composed of fresh air. Further, because the combustion is maintained near stoichiometry, the exhaust gases are only composed of burned gases. Figure 3.2 presents the input variables of the breathing model. Notice that the IGR mass variable represents either the in-cylinder burned gas mass when the engine is operating under atmospheric conditions, or the scavenged air mass when the engine is operating under turbocharged conditions.

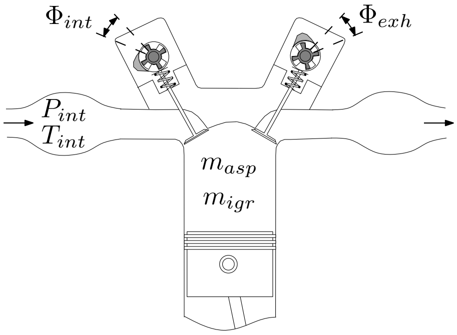

Figure 3.2: SI engine control variables as a function of cylinder bounding conditions. m_{asp} and m_{igr} are the control targets. P_{int}, Φ_{int} and Φ_{exh} are the “actuators”.

The global model consists of a static relationship expressing the aspirated air mass and the IGR mass as functions of the outputs of dynamical systems governing the intake manifold pressure and the VVT actuators positions (see Figure 3.3).

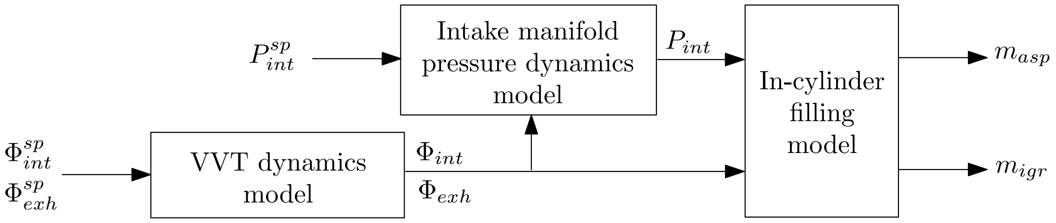

Figure 3.3: Scheme of the system modeling. Intake pressure and VVT actuators positions set points are the inputs of dynamical systems. Note that VVT actuators have an impact on the intake manifold pressure dynamics. The quasi-static cylinder filling model give aspirated and IGR masses.

3.1.1 Intake manifold pressure and VVT dynamics

Intake manifold pressure

Under atmospheric conditions, the throttle can be used to (almost instantly) control the intake manifold pressure. Under turbocharged conditions, the throttle is wide open, and the intake manifold pressure equals the downstream compressor pressure minus negligible pressure losses. In this latter regime, the dynamics of the intake manifold pressure depends on the turbocharger inertia. Its control is achieved by actuating the wastegate.

No details are given for modeling. The intake manifold dynamics has been largely described in the literature (see [26], [16] or [60] for example, also recalled in Appendix A). Here, it is simply assumed that, thanks to a well-designed controller, the dynamics of the intake manifold pressure follows a first-order dynamics with a response time depending on the engine operating point and the VVT actuators positions. This is a very reasonable assumption. The pressure dynamics (representing both system and controller dynamics) reads

$$\dot{P}_{int} = \varphi(P_{int}, \Phi_{int}, \Phi_{exh}, P_{int}^{sp}) \tag{3.1}$$

The static gain between P_{int} and P_{int}^{sp} is equal to 1 (i.e. the intake pressure controller is efficient and yields zero static error). It is now mathematically formulated two physical properties of the intake manifold system and the impact of the VVT onto it. First, stability and time constant boundedness of the intake manifold pressure system are assumed. In details, it is assumed that there exist two positive constant parameters $\underline{\lambda}$ and $\overline{\lambda}$ such that

$$-\overline{\lambda} \leq \frac{\partial \varphi}{\partial P_{int}} = -\frac{\partial \varphi}{\partial P_{int}^{sp}} \leq -\underline{\lambda} < 0 \tag{3.2}$$

Roughly speaking, $\underline{\lambda}$ and $\overline{\lambda}$ represent the settling time corresponding to the two operating areas. Notice that the turbocharger dynamics highly depends on the engine speed. Settling time variations can be of order of 5 between the two operating areas.

Further, it is also assumed that the VVT actuators have limited impact on the pressure dynamics. For this, two constant parameters δ_i and δ_e are introduced such that

$$\left\|\frac{\partial\varphi}{\partial\Phi_{int}}\right\| \leq \delta_i \quad \text{and} \quad \left\|\frac{\partial\varphi}{\partial\Phi_{exh}}\right\| \leq \delta_e \tag{3.3}$$

As will be discussed later in Section 3.3, these two assumptions (3.2) and (3.3) are consistent with observed behaviors.

VVT actuator positions

VVT actuators are hydraulically actuated (see [19] for a complete description of such systems). Their dynamics depends on the internal oil pressure and temperature (see [8], [18]). Therefore they are controlled in a closed loop. Their positions Φ_{int} and Φ_{exh} are measured by sensors.

Classically, the VVT actuators are modeled as first-order systems with response times depending on the engine operating point. Then, the dynamics of the VVT actuator positions (representing both system and controller dynamics) can be written under the following form

$$\begin{cases} \dot{\Phi}_{int} = \eta_i(\Phi_{int}, \Phi_{int}^{sp}) \\ \dot{\Phi}_{exh} = \eta_e(\Phi_{exh}, \Phi_{exh}^{sp}) \end{cases} \tag{3.4}$$

The static gains between Φ_{int} and Φ_{int}^{sp}, and between Φ_{exh} and Φ_{exh}^{sp}, respectively, are assumed to be equal to 1 (i.e. that both the intake and the exhaust VVT controllers are efficient and yield zero static error). Again, stability and time constant boundedness of the VVT actuators systems are assumed. For this, it is assumed that there exist four positive constant parameters $\underline{\mu_i}$, $\overline{\mu_i}$, $\underline{\mu_e}$, and $\overline{\mu_e}$ such that

$$\begin{aligned} -\overline{\mu_i} \leq \frac{\partial\eta_i}{\partial\Phi_{int}} = -\frac{\partial\eta_i}{\partial\Phi_{int}^{sp}} \leq -\underline{\mu_i} < 0 \\ -\overline{\mu_e} \leq \frac{\partial\eta_e}{\partial\Phi_{exh}} = -\frac{\partial\eta_e}{\partial\Phi_{exh}^{sp}} \leq -\underline{\mu_e} < 0 \end{aligned} \tag{3.5}$$

These inequalities allow to bound the nonlinearities of (3.4). Contrary to the intake manifold pressure, VVT dynamics is about the same over the whole engine operating area (for a given oil temperature).

3.1.2 Breathing model

The quantities of aspirated fresh air and IGR at each stroke are determined by the thermal conditions of the intake manifold (pressure, P_{int}, and temperature, T_{int}), the engine speed, N_e, and the positions of the VVT actuators, Φ_{int} and Φ_{exh}, respectively. Detailed models have been presented in Section 2.2.2 and are recalled below (3.6). These allow determination of the aspirated air mass, and the IGR mass using engine geometrical parameters

$$\begin{cases} m_{asp} = \alpha_1 \dfrac{P_{int} V_{ivc}(\Phi_{int})}{RT_{int}} - \alpha_2 \dfrac{\mathrm{OF}(\Phi_{exh} - \Phi_{int})}{N_e} - \alpha_3 V_{evc}(\Phi_{exh}) \\ m_{igr} = \alpha_2 \dfrac{\mathrm{OF}(\Phi_{exh} - \Phi_{int})}{N_e} + \alpha_3 V_{evc}(\Phi_{exh}) \end{cases} \tag{3.6}$$

where α_1, α_2, and α_3 are known functions of P_{int} and N_e (this dependency is omitted for sake of conciseness). V_{ivc} is the cylinder volume at intake valve closing (ivc). It is a function of the intake valve timing, Φ_{int}. Similarly, V_{evc} is the cylinder volume at exhaust valve closing (evc). It is a function of the exhaust valve timing, Φ_{exh}. Finally, the overlap factor (OF) is a function of both the intake and the exhaust valve timings, Φ_{int} and Φ_{exh}.

3.1.3 Breathing model properties

Let $\Omega_{\Phi_{int}}$, $\Omega_{\Phi_{exh}}$, Ω_p, Ω_{asp}, and Ω_{igr} be the sets of practically feasible values of the intake VVT actuator position, exhaust VVT actuator position, intake manifold pressure, air mass, and IGR mass, respectively.

Using (3.6), functions $f : \mathbb{R}^3 \to \mathbb{R}$ and $g : \mathbb{R}^3 \to \mathbb{R}$ are defined such that[2]

$$\begin{cases} m_{asp} \triangleq f(P_{int}, \Phi_{int}, \Phi_{exh}) \\ m_{igr} \triangleq g(P_{int}, \Phi_{int}, \Phi_{exh}) \end{cases} \tag{3.7}$$

Owing to the structure of α_1, α_2, α_3, OF, V_{ivc}, and V_{evc} as functions of P_{int}, Φ_{int}, and Φ_{exh}, the following three partial-invertibility assumptions hold.

---

[2] Notice that we do not mention the dependency on the engine speed and the intake manifold temperature for sake of conciseness.

Proposition 3.1.
For all $(\Phi_{int}, \Phi_{exh}, m_{asp}) \in \Omega_{\Phi_{int}} \times \Omega_{\Phi_{exh}} \times \Omega_{air}$*, there exists a unique* $P_{int} \in \Omega_p$ *such that* $f(P_{int}, \Phi_{int}, \Phi_{exh}) = m_{asp}$*. The inverse function* $F : \Omega_{\Phi_{int}} \times \Omega_{\Phi_{exh}} \times \Omega_{air} \rightarrow \Omega_p$ *is defined such that for all* $(\Phi_{int}, \Phi_{exh}) \in \Omega_{\Phi_{int}} \times \Omega_{\Phi_{exh}}$*,*

$$f(F(\Phi_{int}, \Phi_{exh}, m_{asp}), \Phi_{int}, \Phi_{exh}) = m_{asp} \tag{3.8}$$

Proof 3.1.

Let $\zeta : \mathbb{R}^3 \times \mathbb{R} \rightarrow \mathbb{R}$ be a class C^1 mapping such that $\zeta(\Phi_{int}, \Phi_{exh}, m_{asp}, P_{int}) = f(P_{int}, \Phi_{int}, \Phi_{exh}) - m_{asp}$. By definition, there exist a point $(\Phi^0_{int}, \Phi^0_{exh}, m^0_{asp}, P^0_{int}) \in W$ where W is an open set of $\mathbb{R}^4$ such that $\zeta(\Phi^0_{int}, \Phi^0_{exh}, m^0_{asp}, P^0_{int}) = 0$ (reference steady-state point). This shows that at every engine operating point,

$$\left.\frac{\partial \zeta}{\partial P_{int}}\right|_{\Phi^0_{int}, \Phi^0_{exh}, m^0_{asp}, P^0_{int}} \neq 0$$

Physically, this means that the variation of the aspirated air mass in response to a variation of the intake manifold pressure is never null. Then, from the implicit function theorem, there exist an open set $U = \Omega_{\Phi_{int}} \times \Omega_{\Phi_{exh}} \times \Omega_{air} \subset \mathbb{R}^3$, an open set $V = \Omega_p \subset \mathbb{R}$, and a class C^1 mapping $F : U \rightarrow V$ such that

- for all $(\Phi_{int}, \Phi_{exh}, m_{asp}, P_{int}) \in U \times V$, one has

$$\zeta(\Phi_{int}, \Phi_{exh}, m_{asp}, P_{int}) = 0 \;\Rightarrow\; P_{int} = F(\Phi_{int}, \Phi_{exh}, m_{asp})$$

- for all $(\Phi_{int}, \Phi_{exh}, m_{asp}) \in U$, one has

$$\zeta(\Phi_{int}, \Phi_{exh}, m_{asp}, F(\Phi_{int}, \Phi_{exh}, m_{asp})) \;=\; 0$$

Then, from the definition of the function ζ, the proposition follows. ■

Similarly, the two following propositions follow from the same reasoning.

Proposition 3.2.
For all $(P_{int}, \Phi_{exh}, m_{igr}) \in \Omega_p \times \Omega_{\Phi_{exh}} \times \Omega_{igr}$*, there exists a unique* $\Phi_{int} \in \mathbb{R}$ *such that* $g(P_{int}, \Phi_{int}, \Phi_{exh}) = m_{igr}$*. One can define the inverse function* $G_i : \Omega_p \times \Omega_{\Phi_{exh}} \times \Omega_{igr} \rightarrow \Omega_{\Phi_{int}}$ *such that for all* $(P_{int}, \Phi_{exh}) \in \Omega_p \times \Omega_{\Phi_{exh}}$*,*

$$g(P_{int}, G_i(P_{int}, \Phi_{exh}, m_{igr}), \Phi_{exh}) = m_{igr} \tag{3.9}$$

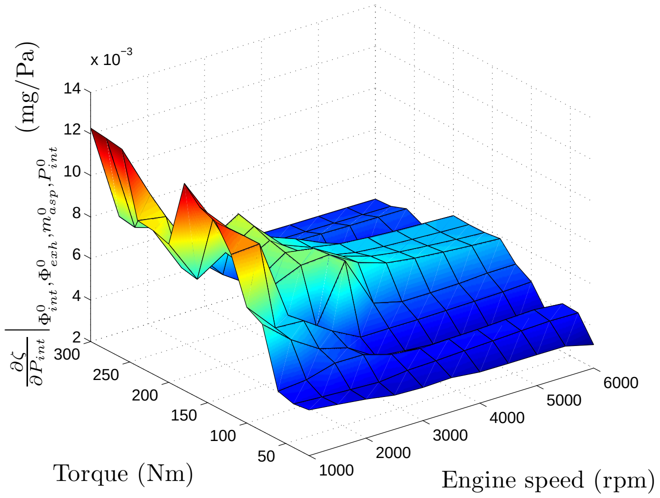

Figure 3.4: Numerical investigation of the sufficient condition for applying the implicit function theorem at each engine operating point.

Proposition 3.3.
For all $(P_{int}, \Phi_{int}, m_{igr}) \in \Omega_p \times \Omega_{\Phi_{int}} \times \Omega_{igr}$*, there exists a unique* $\Phi_{exh} \in \mathbb{R}$ *such that* $g(P_{int}, \Phi_{int}, \Phi_{exh}) = m_{igr}$*. One can define the inverse function* $G_e : \Omega_p \times \Omega_{\Phi_{int}} \times \Omega_{igr} \to \Omega_{\Phi_{exh}}$ *such that for all* $(P_{int}, \Phi_{int}) \in \Omega_p \times \Omega_{\Phi_{int}}$*,*

$$g(P_{int}, \Phi_{int}, G_e(P_{int}, \Phi_{int}, m_{igr})) = m_{igr} \tag{3.10}$$

In practice, VVT actuators can only admit bounded values. The inversion formula appearing in (3.9) and (3.10) may produce infeasible values that need to be saturated before they can be used as input signals to the VVT control system. This point is addressed in the next section.

3.2 Proposed control strategy

One notes T_q^{sp} the torque requested by the driver through the accelerator pedal[3]. Then, m_{asp}^{sp} and m_{igr}^{sp} are defined as the set points for the aspirated fresh-air and IGR masses given by the model (3.7), and by lookup tables experimentally derived from steady-state calibration on a test bench (giving set points for the intake manifold pressure and VVT actuator positions; see Figure 1.8), i.e.

$$\begin{cases} m_{asp}^{sp} \triangleq f(P_{int}^{sp}, \Phi_{int}^{sp}, \Phi_{exh}^{sp}) \\ m_{igr}^{sp} \triangleq g(P_{int}^{sp}, \Phi_{int}^{sp}, \Phi_{exh}^{sp}) \end{cases} \tag{3.11}$$

---

[3] There is a high-level torque demand filtering to account for driveability constraints.

The two control inputs, the intake manifold pressure, and the VVT have an effect on the outputs, m_{asp} and m_{igr}, in a quasi-static way. It is then possible to achieve accurate control by inverting the model (3.7) of the aspirated air and IGR masses.

3.2.1 Coordination strategy

The inverse models (3.8)-(3.9)-(3.10) outlined in Section 3.1.3 are used to compute set points for the low-level controllers. To take into account the previously discussed slow responses of the corresponding subsystems, target set points are replaced with real-time measurements. Among the numerous possible solutions, it has been chosen a technique aimed at satisfying the objectives for both the aspirated air mass and the IGR mass.

Aspirated air mass control

By comparison with the intake manifold pressure, VVT actuators have a more limited effect on the fresh air charge (as is evidenced by the breathing model structure (3.6)). Therefore, the intake manifold pressure is used as the control variable for control of the aspirated air mass. From an aspirated air mass set point m_{asp}^{sp}, a pressure set point $\overline{P_{int}}$ is computed by inverting the quasi-static model (3.7), using the function F defined in (3.8). In this formula, *measurements of the VVT actuator positions are used* (Φ_{int} and Φ_{exh}). This gives

$$\overline{P_{int}} = F(\Phi_{int}, \Phi_{exh}, m_{asp}^{sp}) \tag{3.12}$$

From (3.8), the following proposition holds.

Proposition 3.4.
If the intake manifold pressure P_{int} converges towards its set point $\overline{P_{int}}$ defined by (3.12), then the aspirated air mass m_{asp} defined in (3.7) converges towards its set point m_{asp}^{sp}.

The intake manifold pressure (3.1) is controlled by the throttle and by the wastegate at partial and high loads, respectively.

Remark 3.1.
Proposition 3.4 states that the aspirated air mass request is satisfied when the intake manifold pressure reaches its set point, for any VVT actuators positions. This permits compensation of the relative sluggishness of the VVT actuators compared to the intake pressure (under atmospheric conditions). Notice that this is only the case when the

pressure controller is fast enough. In Appendix A, a controller is proposed, based on a reference trajectory-tracking strategy, that guarantees this fact.

IGR mass control

The second control objective is the IGR mass. To reach this goal, two control variables remain: the positions of the VVT actuators. In fact, the IGR system is over actuated. First, the exhaust valve timing set point is determined, $\overline{\Phi_{exh}}$. Lookup tables obtained from engine energy optimization studies are used. This gives

$$\overline{\Phi_{exh}} = \Phi_{exh}^{sp} \tag{3.13}$$

Then, the intake valve timing Φ_{int} remains as a possible control variable to control the IGR mass. Its set point $\overline{\Phi_{int}}$ is computed from the IGR mass set point m_{igr}^{sp}. Again, as in Section 3.2.1, to coordinate the two control subsystems and maximize the speed of transients, *the intake manifold pressure set point is substituted by measurements* (P_{int}), using the function G_i defined in (3.9). This gives

$$\overline{\Phi_{int}} = G_i(P_{int}, \Phi_{exh}^{sp}, m_{igr}^{sp}) \tag{3.14}$$

Finally, when the control variable $\overline{\Phi_{int}}$ becomes infeasible (when the intake VVT set point is out of the saturation bounds), Equation (3.14) is saturated to the maximum or minimum admissible value, and the leftover degree of freedom, $\overline{\Phi_{exh}}$, is used to minimize the induced IGR mass mismatch. Using the function G_e defined in (3.10), the computation of the exhaust VVT position set point can be written as

$$\overline{\Phi_{exh}} = G_e(P_{int}, \overline{\Phi_{int}}, m_{igr}^{sp}) \tag{3.15}$$

Gathering (3.13), (3.14), and (3.15) together, the VVT control strategy can be written as

$$\left\{ \begin{array}{l} \overline{\Phi_{int}} = G_i(P_{int}, \Phi_{exh}^{sp}, m_{igr}^{sp}) \\ \overline{\Phi_{exh}} = \left\{ \begin{array}{ll} \Phi_{exh}^{sp} & \text{if } \overline{\Phi_{int}} \in \overset{\circ}{\Omega}_{\Phi_{int}} \\ G_e(P_{int}, \overline{\Phi_{int}}, m_{igr}^{sp}) & \text{otherwise} \end{array} \right. \end{array} \right. \tag{3.16}$$

where $\overset{\circ}{\Omega}_{\Phi_{int}}$ is the interior of the feasible set $\Omega_{\Phi_{int}}$. From (3.9) and (3.10), the following proposition holds.

Proposition 3.5.
The control strategy (3.16) guarantees that, provided that at least one of the two VVT positions is not saturated, when the positions of both VVT actuators converge towards their set points, the IGR mass m_{igr} *converges towards its set point* m_{igr}^{sp}.

The position of the valve gear is actuated by means of electronically controlled hydraulic devices. No details on the low-level VVT controller are given; the interested reader can refer to [8] or [18], for example.

3.2.2 Block structure

The two control laws (3.12) and (3.16) are now gathered. This gives the global control scheme pictured in Figure 3.5. The two control strategies are implemented in the *high-level controller* block. This block feeds the *low-level controllers* handling the intake manifold pressure and the VVT actuators. Measurements of the intake manifold pressure and VVT actuators are used in the high-level controller to coordinate the low-level controllers by means of the reference signals $\overline{P_{int}}$, $\overline{\Phi_{int}}$, and $\overline{\Phi_{exh}}$, determined according to (3.12) and (3.16).

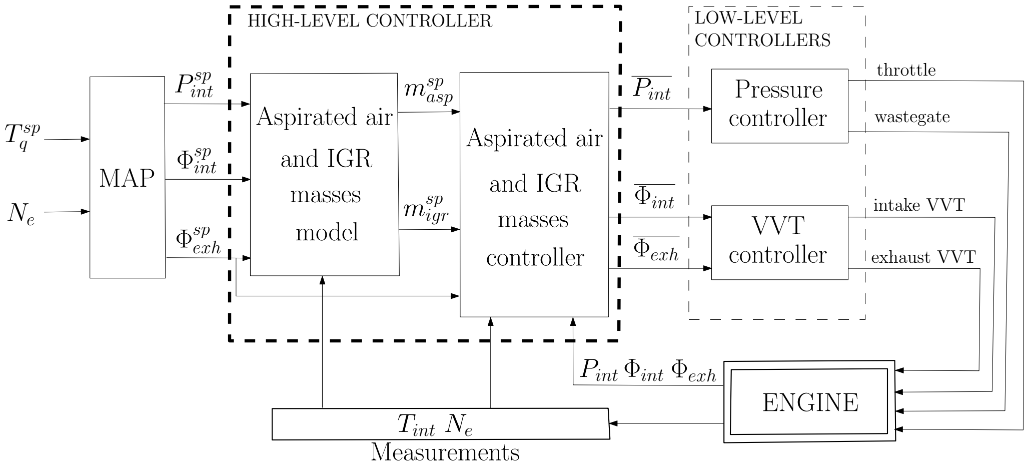
HIGH-LEVEL CONTROLLER
LOW-LEVEL CONTROLLERS
T_q^{sp}
N_e
MAP
P_{int}^{sp}
Φ_{int}^{sp}
Φ_{exh}^{sp}
Aspirated air and IGR masses model
m_{asp}^{sp}
m_{igr}^{sp}
Aspirated air and IGR masses controller
$\overline{P_{int}}$
$\overline{\Phi_{int}}$
$\overline{\Phi_{exh}}$
Pressure controller
VVT controller
throttle
wastegate
intake VVT
exhaust VVT
ENGINE
P_{int} Φ_{int} Φ_{exh}
T_{int} N_e
Measurements

Figure 3.5: Control scheme. The high-level controller coordinates the low-level controllers using control laws (3.12) and (3.16).

In the control strategy, the cylinder filling model is inverted in order to satisfy the high-level requirements during transients. In this way, potential modeling errors can be canceled and do not alter engine working during steady-state conditions (same model is used for set point computation and coordination control strategy). However, as we have introduced a feedback loop in the control strategy, we must assess stability of the newly interconnected system.

3.2.3 Stability analysis

Stability of the aspirated air and IGR masses can be addressed by studying stability of the intake manifold pressure and VVT actuators positions (because of the static nature of the relationship between these variables, see (3.7)). Now, we wish to investigate the convergence of the interconnection that we have created, which is sketched in Figure 3.6.

For sake of simplicity, but without loss of generality, only one VVT actuator is considered in the stability analysis, insofar as one of the two actuators is set to its optimal value or is saturated (see (3.16)). Depending on the case of interest, one notes Φ the intake or the exhaust VVT actuator position. Figure 3.6 represents the dynamical system derived from the control implementation shown in Figure 3.5.

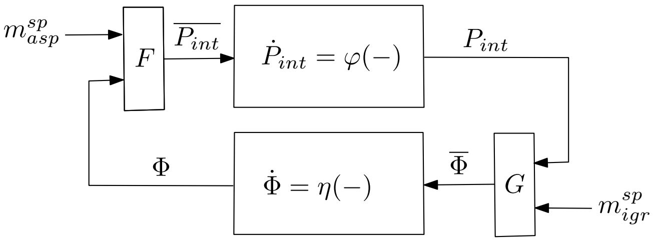

Figure 3.6: The control strategy implies an interconnection of the intake manifold pressure and the VVT subsystems. The mappings F and G are given by the model inversions (3.8) and (3.9)–(3.10).

Let $x \triangleq [P_{int},\ \Phi]^T$, $y \triangleq [P_{int},\ \Phi]^T$, and $u \triangleq [m^{sp}_{asp},\ m^{sp}_{igr}]^T$ be the state, the output, and the input, respectively, of the system represented in Figure 3.5. Then, gathering systems (3.1) and (3.4), and using the control strategies (3.12) and (3.16), one obtains

$$\dot{x}_1 = \varphi(x_1, y_2, F(y_2, u_1)),\ y_1 = x_1 \tag{3.17a}$$

$$\dot{x}_2 = \eta(x_2, G(y_1, u_2)), \qquad y_2 = x_2 \tag{3.17b}$$

From the (partial-)invertibility properties of the model given in Section 3.1.3, for every $\overline{u} \triangleq (\overline{u}_1, \overline{u}_2)$ a unique equilibrium point $\overline{x} \triangleq (\overline{x}_1, \overline{x}_2)$ needs to be considered. This can be written as

$$\begin{cases} \overline{x}_1 = F(\overline{x}_2, \overline{u}_1) \\ \overline{x}_2 = G(\overline{x}_1, \overline{u}_2) \end{cases} \tag{3.18}$$

Let $\tilde{x} \triangleq x - \overline{x}$ and $\tilde{y} \triangleq \tilde{x}$ be the error state and the output, respectively. The system (3.17a)–(3.17b) can be rewritten under the form

$$\dot{\tilde{x}}_1 = \varphi(\tilde{x}_1 + \overline{x}_1, \tilde{y}_2 + \overline{x}_2, F(\tilde{y}_2 + \overline{x}_2, \overline{u}_1)), \; \tilde{y}_1 = \tilde{x}_1 \tag{3.19a}$$

$$\dot{\tilde{x}}_2 = \eta(\tilde{x}_2 + \overline{x}_2, G(\tilde{y}_1 + \overline{x}_1, \overline{u}_2)), \qquad \tilde{y}_2 = \tilde{x}_2 \tag{3.19b}$$

The system (3.19a)–(3.19b) is composed of two interconnected systems. Figure 3.7 gives a representation of the interconnection.

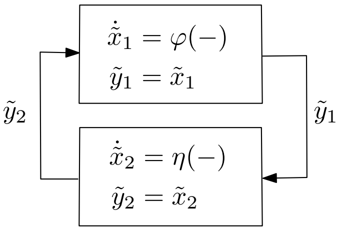
$\dot{\tilde{x}}_1 = \varphi(-)$
$\tilde{y}_1 = \tilde{x}_1$
$\tilde{y}_2$
$\tilde{y}_1$
$\dot{\tilde{x}}_2 = \eta(-)$
$\tilde{y}_2 = \tilde{x}_2$

Figure 3.7: Interconnected system (3.19a)–(3.19b).

Analyzing the stability of the system (3.19a)–(3.19b) leads to the following proposition[4].

Proposition 3.6.
The equilibrium point (3.18) is globally asymptotically stable (GAS) for the system (3.17a)–(3.17b) under the condition $(\overline{\lambda}\overline{\mu}/\underline{\lambda}\underline{\mu})\Gamma_F\Gamma_G < 1$ *where* $\Gamma_F \triangleq \sup_{\tilde{y}_2} \|\partial F/\partial \tilde{y}_2\|$ *and* $\Gamma_G \triangleq \sup_{\tilde{y}_1} \|\partial G/\partial \tilde{y}_1\|$.

Proof 3.2.

Equivalent error dynamics (3.19a)–(3.19b) is used to prove that (0, 0) is GAS. The stability of the global system (3.19a)–(3.19b) can be analyzed with a generalized small-gain theorem [32]. First, the input-to-state stability of the two interconnected systems are analyzed separately. First, (3.19a) having $\tilde{y}_2$ as input is considered, then, (3.19a) having $\tilde{y}_1$ as input is considered.

One begins with the subsystem $\tilde{x}_1$. Let $V_1(\tilde{x}_1) \triangleq \frac{1}{2}\tilde{x}_1^2$. Its differentiation with respect to time is

$$\dot{V}_1(\tilde{x}_1) = \tilde{x}_1\varphi(\tilde{x}_1 + \overline{x}_1, \tilde{y}_2 + \overline{x}_2, F(\tilde{y}_2 + \overline{x}_2, \overline{u}_1)) \tag{3.20}$$

---

[4] For convenience, some useful mathematical definitions (class $\mathcal{K}$ and $\mathcal{KL}$ functions) are recalled in the Notation and Acronyms part at the beginning of this manuscript.

From the intermediate value theorem, and the inequality (3.2), it follows that for all $(\tilde{x}_1, \tilde{y}_2)$,

$$\varphi(\tilde{x}_1 + \overline{x}_1, \tilde{y}_2 + \overline{x}_2, F(\tilde{y}_2 + \overline{x}_2, \overline{u}_1)) \leq -\underline{\lambda}\tilde{x}_1 + \varphi(\overline{x}_1, \tilde{y}_2 + \overline{x}_2, F(\tilde{y}_2 + \overline{x}_2, \overline{u}_1))$$

Then, Equation (3.20) becomes

$$\dot{V}_1(\tilde{x}_1) \leq -\underline{\lambda}\tilde{x}_1^2 + \tilde{x}_1\varphi(\overline{x}_1, \tilde{y}_2 + \overline{x}_2, F(\tilde{y}_2 + \overline{x}_2, \overline{u}_1))$$

For all positive ϵ, the following inequality holds

$$\dot{V}_1(\tilde{x}_1) \leq -\underline{\lambda}\left(1 - \frac{1}{1+\epsilon}\right)\tilde{x}_1^2 \tag{3.21}$$

for all $(\tilde{x}_1, \tilde{y}_2)$ such that

$$\|\tilde{x}_1\| \geq \frac{1+\epsilon}{\underline{\lambda}} \|\varphi(\overline{x}_1, \tilde{y}_2 + \overline{x}_2, F(\tilde{y}_2 + \overline{x}_2, \overline{u}_1))\| \tag{3.22}$$

Further, from the intermediate value theorem, it follows that for all $\tilde{y}_2$,

$$\|\varphi(\overline{x}_1, \tilde{y}_2 + \overline{x}_2, F(\tilde{y}_2 + \overline{x}_2, \overline{u}_1))\| = \left\| \frac{\partial\varphi}{\partial\tilde{y}_2} + \frac{\partial\varphi}{\partial F}\frac{\partial F}{\partial\tilde{y}_2} \right\| \|\tilde{y}_2\|$$

Applying the triangular inequality and using the inequalities (3.2) and (3.3) yields

$$\|\varphi(\overline{x}_1, \tilde{y}_2 + \overline{x}_2, F(\tilde{y}_2 + \overline{x}_2, \overline{u}_1))\| \leq \left(\delta + \overline{\lambda}\Gamma_F\right) \|\tilde{y}_2\| \tag{3.23}$$

where $\Gamma_F \triangleq \sup_{\tilde{y}_2} \|\partial F/\partial\tilde{y}_2\|$. Then, using the inequality (3.23) in (3.22), it follows that the inequality (3.21) holds for all $(\tilde{x}_1, \tilde{y}_2)$ such that

$$\|\tilde{x}_1\| \geq \frac{1+\epsilon}{\underline{\lambda}} \left(\delta + \overline{\lambda}\Gamma_F\right) \|\tilde{y}_2\|$$

Hence, the conditions of the Lyapunov-like theorem [34, Theorem 4.19] (sufficient conditions for input-to-state stability) are satisfied. The system (3.19a) having $\tilde{y}_2$ as input is input-to-state stable [72] with the class $\mathcal{K}$ function $\gamma_1(s) = ((1+\epsilon)/\underline{\lambda})\left(\delta + \overline{\lambda}\Gamma_F\right)s$. In other words, there exists a class $\mathcal{KL}$ function β_1 such that, for any initial state $\tilde{x}_1(t_0)$ and any bounded input $\tilde{y}_2(t)$, the solution $\tilde{x}_1(t)$ exists for all $t \geq t_0$ and satisfies

$$\|\tilde{x}_1(t)\| \leq \beta_1(\|\tilde{x}_1(t_0)\|, t - t_0) + \gamma_1\left(\sup_{t_0 \leq \tau \leq t} \|\tilde{y}_2(\tau)\|\right) \tag{3.24}$$

Now, consider the subsystem $\tilde{x}_2$. Similarly, the system is input-to-state stable with the class $\mathcal{K}$ function $\gamma_2(s) = ((1+\epsilon)/\underline{\mu})\overline{\mu}\Gamma_G s$, where $\Gamma_G \triangleq \sup_{\tilde{y}_1} \|\partial G/\partial \tilde{y}_1\|$. This means that there exists a class $\mathcal{KL}$ function β_2 such that, for any initial state $\tilde{x}_2(t_0)$ and any bounded input $\tilde{y}_1(t)$, the solution $\tilde{x}_2(t)$ exists for all $t \geq t_0$ and satisfies

$$\|\tilde{x}_2(t)\| \leq \beta_2(\|\tilde{x}_2(t_0)\|, t - t_0) + \gamma_2\left(\sup_{t_0 \leq \tau \leq t} \|\tilde{y}_1(\tau)\|\right) \tag{3.25}$$

Now, consider the interconnected system (3.19a)–(3.19b). The generalized small-gain theorem derived in [32] can be used to prove that $(0,0)$ is GAS. From (3.24) and (3.25), a sufficient small-gain condition is

$$\gamma_1 \circ \gamma_2(s) = \frac{\overline{\mu}(1+\epsilon)^2}{\underline{\lambda}\underline{\mu}}\left(\delta + \overline{\lambda}\Gamma_F\right)\Gamma_G s$$

Assuming the impact of the VVT actuators on the pressure dynamics to be small ($\delta \ll \overline{\lambda}\Gamma_F$), and for small ϵ, the small-gain condition becomes

$$\gamma_1 \circ \gamma_2(s) = \frac{\overline{\lambda}\overline{\mu}}{\underline{\lambda}\underline{\mu}}\Gamma_F\Gamma_G s \tag{3.26}$$

If the small-gain condition (3.26) satisfies $\gamma_1 \circ \gamma_2(s) < s$, then the system (3.19a)–(3.19b) is input-to-state stable. Moreover, as this system is unforced, the origin is GAS. This concludes the proof. ∎

3.2.4 Practical usage of the stability analysis

The estimate (3.26) of the loop gain of the interconnected system pictured in Figure 3.7 plays a key role in practical experiments.

In this expression, two factors appear. The first factor is $\overline{\lambda}\overline{\mu}/\underline{\lambda}\underline{\mu}$, which is evaluated from the bounds $\underline{\lambda}$, $\overline{\lambda}$, $\underline{\mu}$, and $\overline{\mu}$ defined in (3.2) and (3.5). Provided that the ranges of the state variables remain reasonably narrow, the upper and lower bounds $\overline{\lambda}$, $\underline{\lambda}$, and $\overline{\mu}$, $\underline{\mu}$ are close. Therefore, it can be expected that the first factor $\overline{\lambda}\overline{\mu}/\underline{\lambda}\underline{\mu}$ is bounded by 10 for transients of practical interest. This is typically the case for the experiments described in Section 3.3, more specifically in Figure 3.12 where the intake manifold pressure follows two very different dynamics due to atmospheric and turbocharged operating conditions. In the other hand, $\overline{\mu}$ and $\underline{\mu}$ are close because VVT actuators positions dynamics are quite the same over the entire operating range.

The second factor is $\Gamma_F \Gamma_G$. Its value depends on the operating conditions, i.e. the engine speed and the reference intake manifold pressure. This is shown in Figure 3.8. It is easy to see that for most of the conditions under consideration, i.e. away from 1 bar, the value of the second factor is largely below 1 (implying GAS of the origin). Naturally, the zone of pressures around 1 bar requires particular attention. The small gain sufficient condition could not be satisfied. We could consider adding a gain at the input of the subsystem $\tilde{x}_2$ to reduce the loop gain to a value strictly below 1. Such a gain would be active only when the intake manifold pressure was in the zone around 1 bar (and then guarantying the sufficient small gain condition). However, this ad hoc solution is not required in practice. The reason is that even if the criterion is not respected (note that the fact that the sufficient condition is not guaranteed does not imply instability), the variable $\tilde{x}_2$ would be bounded in practice owing to saturation of the VVT actuators. Furthermore, in this zone of reference pressure, the sensitivity of the aspirated air and IGR masses (model (3.7)) with respect to $\tilde{x}_2$ (VVT actuators) is very small. This point is illustrated in Figure 3.9, where the sensitivity of the aspirated air mass with respect to the exhaust VVT actuator is shown. Therefore, this possibly divergent behavior would have almost no effect on the variables of interest during a transient.

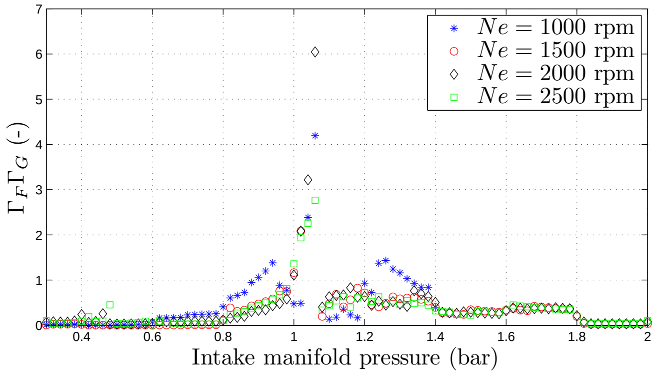

Figure 3.8: Conditions for small-gain theorem.

In summary, the controllers proposed in Section 3.2.1 can be used as-is under the whole range of operating conditions and transients under consideration.

3.3 Experimental results

The performance of the proposed control strategy are now illustrated at the light of experimental results.

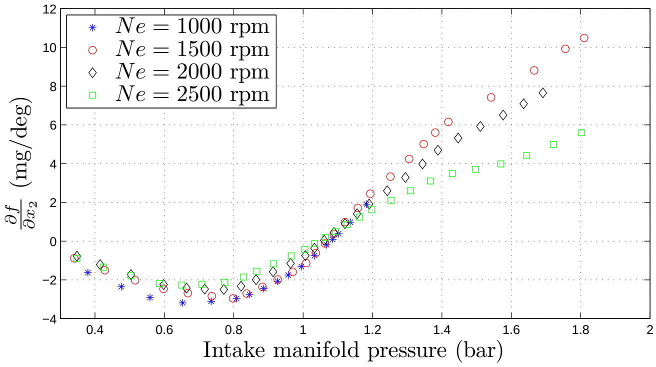

Figure 3.9: Sensitivity of aspirated air mass with respect to the VVT actuator.

3.3.1 Experimental setup

The engine used in the experiments is a 1.8 L four-cylinder SI engine using direct injection and homogeneous combustion. It is described in details in [43]. The air path consists of a turbocharger controlled by a wastegate, an intake throttle, and with two VVT devices, for the intake and exhaust valves. The engine specifications are given in Table 3.1. This engine belongs to the class pictured earlier in Figure 3.1.

Engine type	Renault F5P
Number of cylinders	4
Bore × Stroke	82.7 × 83.0 mm
Compression ratio	10.5:1
Engine Displacement	1.8 Liters
Turbocharger type	Mono-scroll
Intake valve closing	30 / -10 degBTDC
Exhaust valve opening	-29 / 11 degATDC

Table 3.1: Experimental SI engine setup

3.3.2 Low and part load

IGR mass variations

The first scenario under consideration consists of requesting various IGR mass set points for a constant air mass set point. This scenario is of particular interest during test-bench engine energy optimization processes when, for a given torque set point, the optimal IGR mass is sought with respect to criteria of minimum pollutant emissions.

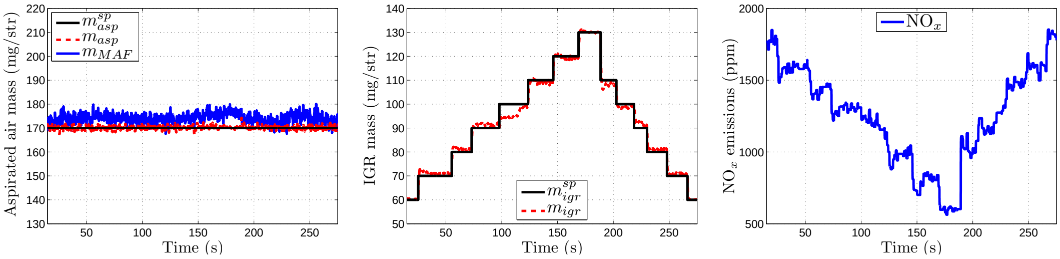

(a) Aspirated air mass (b) IGR mass (c) NO$_x$ emissions

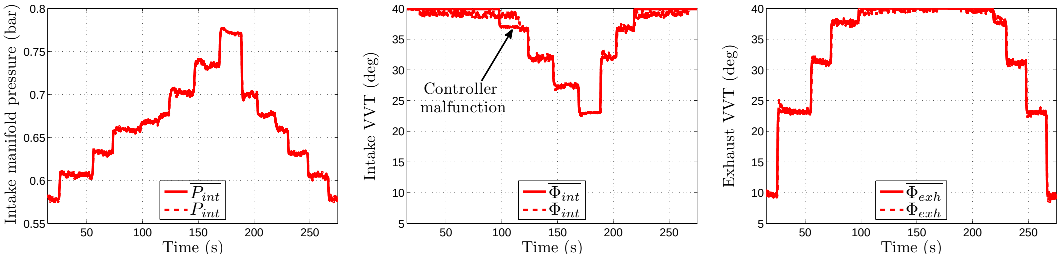

(d) Intake manifold pressure (e) Intake VVT actuator position (f) Exhaust VVT actuator position

Figure 3.10: Test bench experimental results for a four-cylinder turbocharged VVT SI engine at constant engine speed (2000 rpm). Variation of IGR mass at constant aspirated air mass. The tracking of reference signals for the aspirated air mass and IGR mass is very effective. Despite a temporary malfunction of the intake VVT actuator controller (around $t = 100$ s), the first control objective is fulfilled (the aspirated air mass remains constant).

Figure 3.10(b) represents the IGR mass set point m_{igr}^{sp} and its estimate given by the model (3.6), m_{igr}. Figure 3.10(a) gives the aspirated air mass set point (constant) m_{asp}^{sp}, its estimate given by the model (3.6), m_{asp}, and the measurement obtained at test bench with a mass flow sensor, m_{MAF}.

The proposed controller succeeds in fulfilling both objectives by manipulating simultaneously the intake manifold pressure and the VVT actuators. The MAF information stresses the accuracy of the estimation of the aspirated air mass in spite of large intake pressure manifold and VVT actuators variations. It is worth noticing that the limitations on the values of the VVT actuator positions are fully accounted for. This point is particularly visible over the time interval 100–220 s, in Figures 3.10(e) and 3.10(f), when the exhaust VVT actuator saturates to its maximum value while the intake VVT is automatically used to compensate the possibly induced mismatch of the IGR mass. As a result, the IGR mass perfectly tracks its reference, except immediately after $t = 100$ s. Interestingly, the response at time 100 s shows how the proposed controller uses the intake manifold pressure set point as a degree of freedom to compensate the temporary malfunction of the intake VVT actuator controller (see Figure 3.10(d)). Thanks to this insightful decision, the aspirated air mass remains at its set point.

In summary, this experiment stresses two facts. First, it shows the relevance of the cylinder filling model. Figure 3.10(a) shows good results of the aspirated air mass model (compared to MAF measurements), while Figure 3.10(c) demonstrates the good representativeness of the IGR mass of the engine behavior (indeed, increase of the cylinder burned gas fraction decreases NO_x emissions). Second, this experiment gives a first result on the coordination strategy (around time 100 s) that underlines the relevance of the designed control strategy.

Torque transient

The transient response observed in Figure 3.11 is particularly interesting. In this scenario, a torque transient is requested by the driver. This defines an increase in the in-cylinder air mass set point. Similarly, the set point for the IGR mass increases too. To perform this transient, both the intake manifold pressure and the VVT actuators must be controlled. Our proposed controller coordinates both the pressure and the VVT controllers. The VVT actuators behave relatively poorly (see Figure 3.11(d)), which is detected by the controller. To account for the discrepancy between the exhaust VVT set point and its actual position, the intake manifold pressure set point features a sharp change of slope in the middle of the transient (see Figure 3.11(c)). This avoids a possible overshoot in the observed aspirated air mass (see Figure 3.11(a)). The first control objective is fulfilled. The air mass transient is fast and accurate. A similar, but slightly less visible, behavior takes place at the following tip-out.

3.3.3 High load

An experiment was performed using a large torque tip-in, which typically occurs during rapid acceleration of the vehicle. The turbocharger inertia induces a non negligible acceleration time. In this experiment, two control strategies were compared. The first one is based on a quasi-static positioning of the VVT actuators, represented by the symbol "ref". The set points for the intake manifold pressure and VVT actuator positions, P_{int}^{sp}, Φ_{int}^{sp}, and Φ_{exh}^{sp}, are directly derived from reference lookup tables. The second control strategy is the one presented in this thesis (represented by the symbol "strat"). Here, the set points for the intake manifold pressure and VVT actuator positions, $\overline{P_{int}}$, $\overline{\Phi_{int}}$, and $\overline{\Phi_{exh}}$, are computed by the high-level controller presented in Section 3.2.1. Figure 3.12 shows experimental results obtained on vehicle. The aspirated air and IGR masses are given in Figure 3.12(a) and Figure 3.12(b). Figures

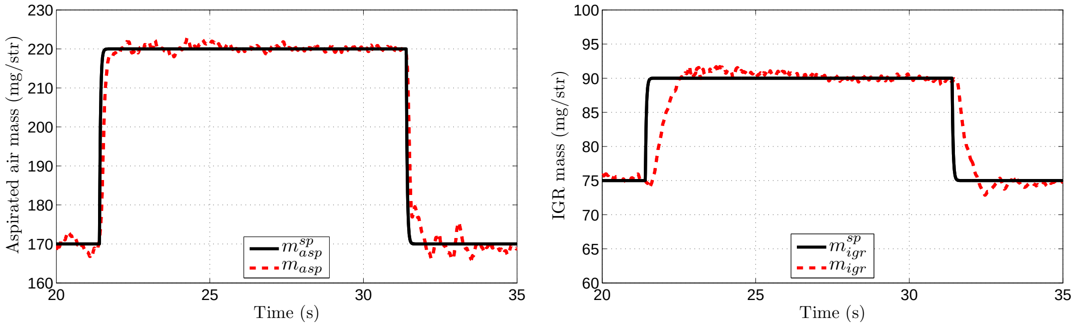

(a) Aspirated air mass

(b) IGR mass

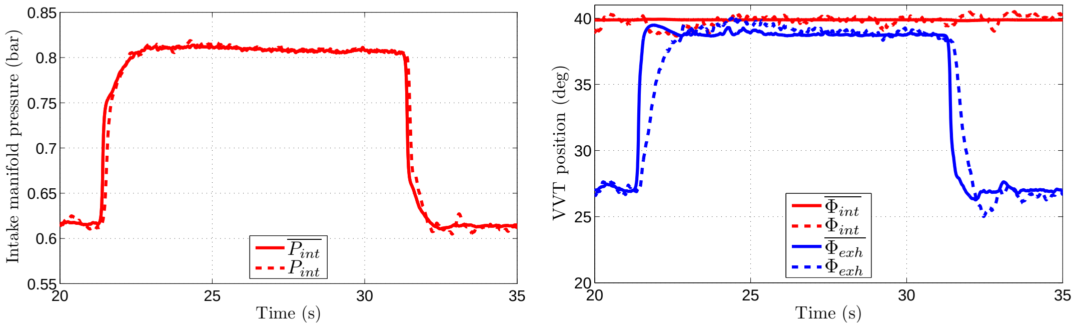

(c) Intake manifold pressure

(d) Intake VVT actuator position

Figure 3.11: Test bench experimental results from a four-cylinder turbocharged VVT SI engine at constant engine speed (2000 rpm). Torque transients under atmospheric conditions. In this regime, the exhaust VVT actuator is slow, and the intake manifold pressure compensates so as to bring the aspirated air mass close to its set point.

3.12(c), 3.12(d), and 3.12(e) give the intake manifold pressure, the intake VVT position, and the exhaust VVT position, respectively. The transient analysis is split into two parts.

The beginning of the transient is from 17.5 s to 17.8 s. The engine is under atmospheric conditions. The intake throttle is fully opened and the intake manifold pressure low-level controller actuates the wastegate to increase the intake manifold pressure. Figure 3.12(c) shows almost no difference between the two control strategies. This means that the VVT actuators have limited impact on the behavior of the intake manifold pressure. Rather, by looking at the VVT actuators positions (Figure 3.12(d) and Figure 3.12(e)), one can see that the proposed controller significantly modifies the position of the two actuators, especially the intake. In fact, the intake VVT actuator is controlled at its upper bound, while the exhaust VVT actuator is controlled below its reference position. Physically, the overlap is minimized to limit IGR. In addition,

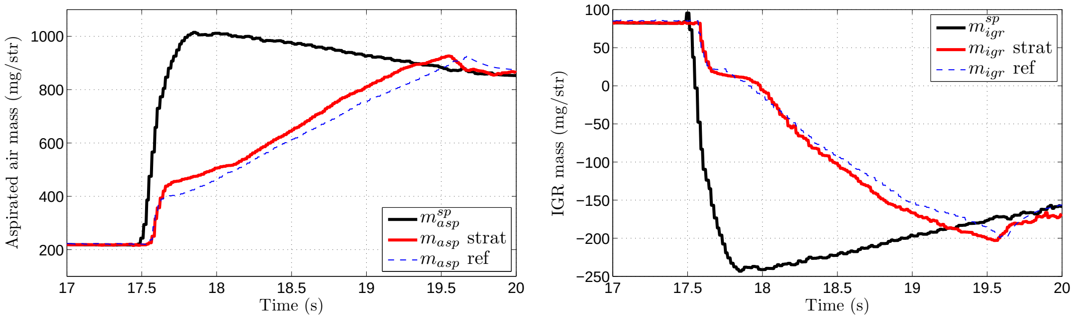

(a) Aspirated air mass (b) IGR mass

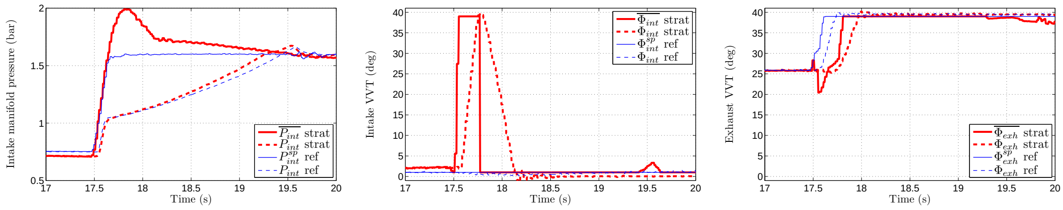

(c) Intake manifold pressure (d) Intake VVT actuator position (e) Exhaust VVT actuator position

Figure 3.12: On-board experimental results from a vehicle equipped with a four-cylinder turbocharged VVT SI engine. Large torque tip-in. Comparison between proposed strategy ("strat") and classical strategy ("ref"). The requested transient corresponds to a target point where the overlap is maximum ($\Phi_{int} = 0$). But, during the transient, the proposed controller temporarily minimizes the overlap until the turbocharging conditions are met (it limits IGR to admit more fresh air into the cylinder). This yields a substantial improvement of the dynamic response.

the response of the aspirated air mass is accelerated using the proposed strategy.

The remainder of the transient is from 17.8 s to 20 s, where the engine is now operating under turbocharged conditions. During this phase, the intake pressure is higher than the exhaust pressure, which allows a certain quantity of air to go directly to the exhaust. The VVT actuators completely change their positions, and go to their opposite extrema. Physically, this maximizes the overlap and scavenges fresh air to the exhaust in order to remove internal burned gases from the cylinder. This has two beneficial effects. First, more air is introduced into the cylinder. Secondly, as a higher gas flow rate reaches the turbine, the compressor of the turbocharger is accelerated more, and the intake manifold pressure is boosted. Notice that this behavior is independent from the fact that the intake manifold pressure set points, P_{int}^{sp} and $\overline{P_{int}}$, are different in the two strategies, since the throttle and the wastegate are saturated in both cases.

Figure 3.13 displays the set point for the engine torque output and the responses obtained for each controller. One can clearly see that the proposed control strategy permits to shorten the response time by approximately 20%.

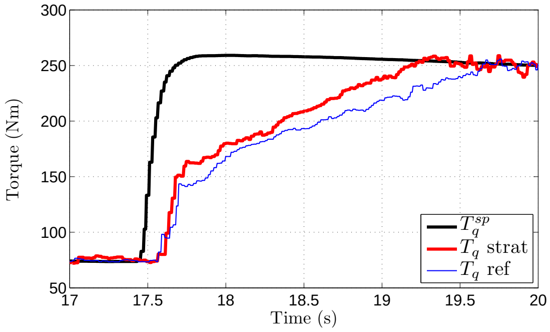

Figure 3.13: On-board experimental results from a vehicle equipped with a four-cylinder turbocharged VVT SI engine. Large torque tip-in. Comparison between proposed strategy ("strat") and classical strategy ("ref") on the torque production.

3.4 Conclusion on the obtained results

A control strategy for the air path of turbocharged SI engines equipped with dual independent VVT actuators has been presented.

The control objectives are defined to be the aspirated fresh air mass and the IGR mass. These variables exactly correspond to the outputs of the breathing model designed in Chapter 2. This model has been proven to have interesting invertibility properties. Then, a control strategy has been developed. It is an add-on to an existing control strategy. It fully exploits this invertible model. The strategy permits to control the masses of both the aspirated air and the IGR. As a result, it accelerates the response of the overall system by coordinating two variables acting on the breathing process, i.e. the intake manifold pressure and the positions of the VVT actuators. It is important to note that the same control strategy operates under both atmospheric and turbocharging conditions, even though the fast and slow variables of the system are not the same in these two operating areas. As the coordination implies an interconnection, the stability has been analyzed theoretically using a generalized small-gain theorem.

The strategy has been tested first on a test bench, and then on-board a vehicle. The experimental results stress the relevance of the control strategy under both atmospheric and turbocharging conditions. A significant reduction of the response time of the air path can be observed, along with an improvement of the engine torque output. Some additional experimental results are given in Appendix A, B and C.

Chapter 4

Case study 2: VLD Diesel engines control

In this chapter, a controller is proposed to handle air path transients of VLD equipped CI engines. Following the approach advocated in this thesis and exposed in Chapter 1, this controller focuses on compensating the difference of response times of the various dynamics of the system. The considered engine setup is pictured in Figure 4.1.

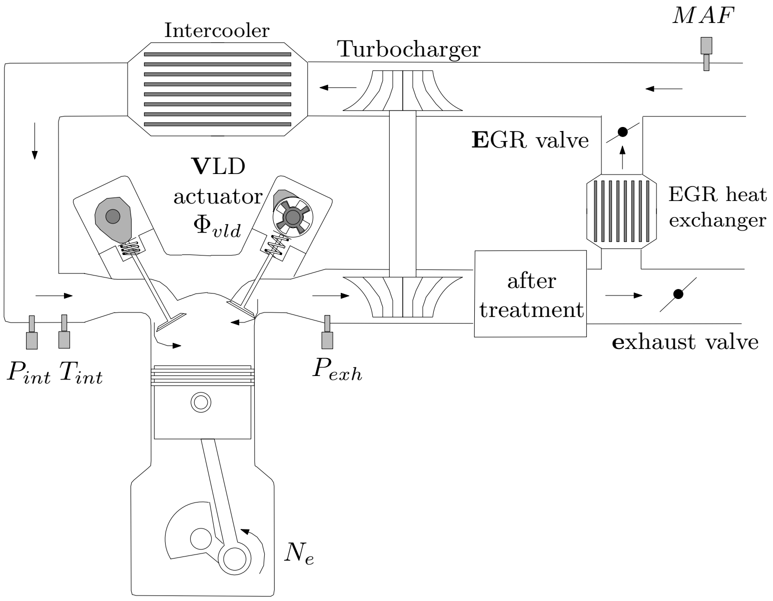
Intercooler
Turbocharger
MAF
EGR valve
VLD
actuator
Φ_{vld}
EGR heat
exchanger
after
treatment
exhaust valve
P_{int} T_{int}
P_{exh}
N_e

Figure 4.1: Schematic illustration of a turbocharged VLD-equipped engine. The intake manifold pressure and temperature P_{int} and T_{int}, the exhaust manifold pressure P_{exh} and the mass air flow at the intake MAF are measured by sensors. Φ_{vld} is the position of the VLD actuator.

In CI engines, while the torque production is guaranteed by the fuel injection control system, NO_x emissions are managed through the cylinder composition. Indeed, as was shown in Chapter 1, the NO_x emissions are closely related to the *in-cylinder BGR* (Burned Gas Rate). Interestingly, controlling this quantity permits to move forward in the direction of combustion control. In engines without any VLD capability, because of the absence of any internal EGR, this variable is simply controlled through the intake manifold BGR (which is supposed to be equal to the in-cylinder BGR). For this purpose, several controllers have been proposed in the literature, see e.g. [28], [7], [18] or [83].

To obtain an accurate control of the in-cylinder composition, the model presented in Chapter 2 is used. It permits to relate the high-level control variable (in-cylinder BGR) and the low-level variables (intake manifold BGR and VLD actuator position). The proposed strategy coordinates the two low-level control subsystems (intake manifold BGR and VLD actuator) to improve the in-cylinder BGR response, and, then, to control the pollutant emissions. When the intake manifold BGR is too slow to converge to its optimal point, the controller adjusts the VLD actuator position set point to speed up the air-feeding process, so that the in-cylinder BGR is satisfied. Explicitly, the set point for the low-level VLD controller is determined in real time, based on an estimate of the intake manifold BGR (several observers can be used to estimate this variable, as are proposed in [9], [84] and the references therein).
In details, the control of the in-cylinder BGR is done to the detriment of the in-cylinder temperature. Indeed, actuating the VLD actuator to compensate for the sluggishness of the intake manifold BGR induces a warm up of the in-cylinder mixture (because hot exhaust gases are aspirated). To limit this increase of in-cylinder temperature (which can be the culprit for smoke emissions), the control strategy saturates the VLD actuator trajectory, which is then bounded by a user-prescribed value.

The derivation of this model-based controller is now detailed.

4.1 System modeling

The proposed controller is designed using the engine breathing model (2.20) of Chapter 2. Contrary to the SI case previously treated, the variable to control (the in-cylinder BGR, X_{ivc}) is not directly given by the breathing model (2.20). Indeed, the presence of burned gases in the intake flow (because of external EGR) and the presence of fresh air in the exhaust flow (because of lean combustion) requires to account for intake and exhaust flows compositions, X_{int} and X_{exh}. Moreover, the in-cylinder temperature results from the blend of the intake and exhaust temperatures, T_{int} and

T_{exh}. Because no exhaust BGR and temperature measurements are available, only a simple combustion model is derived. Figure 4.2 presents the input and output variables of the breathing model.

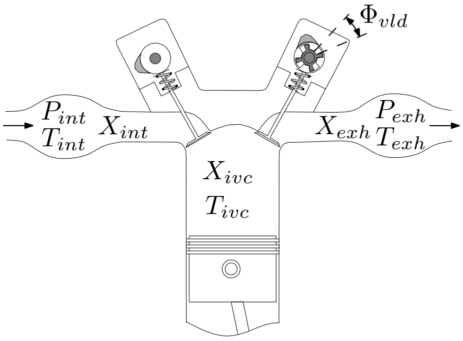

Figure 4.2: CI engine in-cylinder variables as a function of cylinder bounding conditions.

4.1.1 Aspirated masses model

The quantities of aspirated masses from the intake (which is composed of fresh air and burned gases coming from external EGR), and from the exhaust (which is composed of fresh air and burned gases coming from internal EGR) are determined from the thermal conditions of the intake and exhaust manifolds (pressure, P_{int} and P_{exh}, and temperature, T_{int} and T_{exh}), the engine speed, N_e, and the positions of the VLD actuator, Φ_{vld}. A detailed model has been presented in Section 2.3.2. In the present situation, it writes

$$\begin{cases} m_{asp}^{int} = \alpha_1 \dfrac{P_{int} V_{ivc}}{R T_{int}} - \alpha_2 \dfrac{P_{exh}}{R T_{int}} V_{evc}(\Phi_{vld}) \\ m_{asp}^{exh} = \alpha_2 \dfrac{P_{exh}}{R T_{exh}} V_{evc}(\Phi_{vld}) \end{cases} \tag{4.1}$$

where α_1 and α_2 are known functions of N_e (this dependency is omitted hereafter for sake of conciseness). V_{ivc} is the cylinder volume at intake valve closing (ivc). Similarly, V_{evc} is the cylinder volume at exhaust valve closing (evc). It is a function of the VLD actuator position, Φ_{vld} (see Figure D.2(b)).

4.1.2 In-cylinder composition and temperature model

In the following, the ivc is considered as a discrete event indexed by the k variable. Figure 4.3 presents the steps of modeling.

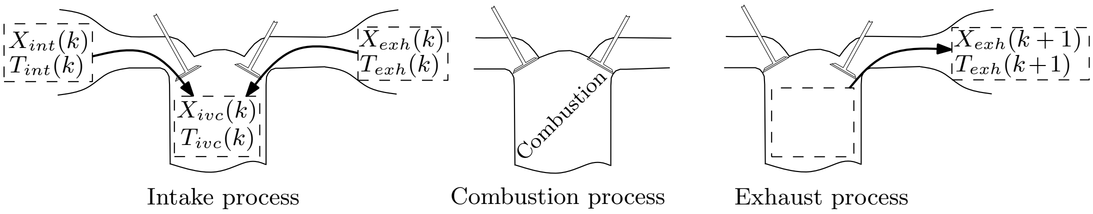

Figure 4.3: Detail of the discrete intake-combustion-exhaust process. First, the in-cylinder BGR and temperature at the discrete time k are determined from the intake and exhaust manifold quantities at instant k. Then, combustion occurs. Finally, the residual gases are expelled from the cylinder during the exhaust stroke, defining the exhaust conditions (BGR and temperature) at the discrete time $k+1$.

Conditions at intake valve closing (ivc)

The in-cylinder BGR at ivc is equal to the mass-weighted average of the BGR of the flows contributing to the total trapped mass

$$X_{ivc}(k) = \frac{X_{int}(k)m_{asp}^{int}(k) + X_{exh}(k)m_{asp}^{exh}(k)}{m_{asp}^{int}(k) + m_{asp}^{exh}(k)} \tag{4.2}$$

Similarly, the in-cylinder temperature at ivc is assumed to be equal to the mass-weighted average (see [15] or [12] for example)

$$T_{ivc}(k) = \frac{T_{int}(k)m_{asp}^{int}(k) + T_{exh}(k)m_{asp}^{exh}(k)}{m_{asp}^{int}(k) + m_{asp}^{exh}(k)} \tag{4.3}$$

Exhaust burned gas rate modeling Assuming complete and lean combustion, the exhaust burned gas rate only depends on the composition inside the cylinder before the combustion (at ivc), and on the quantity of injected fuel. Note m_{air}, m_{bg} and m_f the quantity of in-cylinder fresh air, burned gas and fuel before combustion (instant k) respectively. Then, the burned gas fraction *after* combustion (at the discrete time $k+1$) writes

$$X_{exh}(k+1) = \frac{m_{bg}(k) + (\mathrm{AFR}_s + 1)\cdot m_f(k)}{m_{air}(k) + m_{bg}(k) + m_f(k)} \tag{4.4}$$

where AFR_s is the stoichiometric air/fuel ratio. Using model (4.2) and definition (2.3) (noting $m_{ivc} = m_{asp}^{int} + m_{asp}^{exh}$ as the in-cylinder total mass), one has

$$X_{exh}(k+1) = \frac{m_{ivc}(k)}{m_{ivc}(k) + m_f(k)}\left(X_{ivc}(k) + \frac{(\mathrm{AFR}_s + 1)\cdot m_f(k)}{m_{ivc}(k)}\right) \tag{4.5}$$

Now, the definition of the total in-cylinder mass is used, rewriting equation (2.5) to obtain

$$m_{ivc}(k) = \alpha_1 \frac{P_{int}(k)V_{ivc}}{RT_{ivc}(k)} \tag{4.6}$$

Finally, assuming that the multiplicative ratio $m_{ivc}/(m_{ivc}+m_f)$ is close to 1 (it is always higher than 0.98 in the operating range under consideration) and substituting (4.6) into (4.5), one obtains

$$X_{exh}(k+1) = X_{ivc}(k) + \frac{(\mathrm{AFR}_s + 1) \cdot m_f(k)R}{\alpha_1 P_{int}(k)V_{ivc}} T_{ivc}(k) \tag{4.7}$$

This modeled exhaust BGR dynamics (4.7) can be compared to experimental fuel/air ratio measurements obtained on a test bench (the sensor is located downstream the turbine). Figure 4.4 illustrates the good fit (at steady state) of the model over the whole engine operating range (notice that the transient behavior cannot be compared to real data because there is no high frequency measurement in the exhaust manifold of the considered engine).

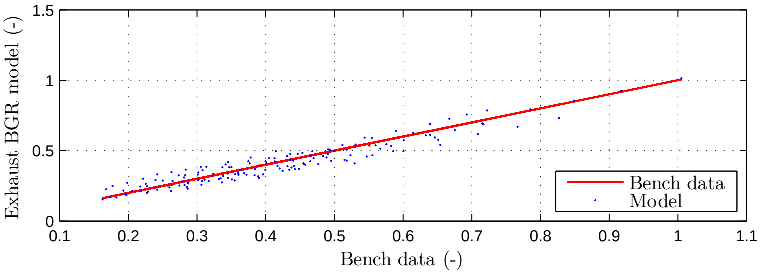

Figure 4.4: Comparisons between modeled and experimental exhaust BGR over the whole engine operating range. Experimental data obtained at test bench on a 4-cylinder CI engine equipped with VLD actuator and LP EGR capability.

Exhaust temperature modeling Figure 4.5 pictures the exhaust temperature modeling. Assuming an adiabatic compression (from *ivc* to *bc*, where *bc* refers to before combustion), an instantaneous heat release (from *bc* to *ac*, where *ac* refers to after combustion), and a polytropic expansion (from *ac* to *evo*, where *evo* refers to

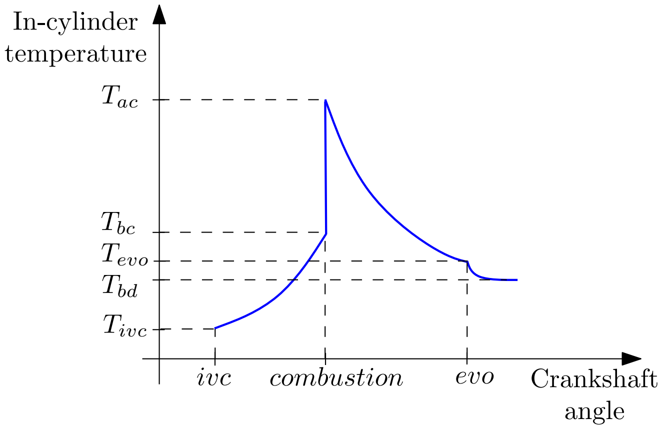

Figure 4.5: Detail of the exhaust temperature model.

exhaust valve opening), the following equalities hold

$$\begin{aligned}T_{ivc}V_{ivc}^{\gamma-1} = T_{bc}V_{comb}^{\gamma-1} &\text{ , and } P_{ivc}V_{ivc}^{\gamma} = P_{bc}V_{comb}^{\gamma}\\ T_{ac} = T_{bc} + \frac{Q_{LHV}m_f}{c_v m_{ivc}} &\text{ , and } \frac{P_{ac}}{T_{ac}} = \frac{P_{bc}}{T_{bc}}\\ T_{ac}V_{comb}^{\gamma-1} = T_{evo}V_{evo}^{\gamma-1} &\text{ , and } P_{ac}V_{comb}^{\gamma} = P_{evo}V_{evo}^{\gamma}\end{aligned} \tag{4.8}$$

where V_{comb} refers to the in-cylinder volume when the combustion starts, γ is the specific heats ratio (here, this ratio is assumed constant), and c_v is the volume specific heat (which is also assumed to be constant). After *evo*, the exhaust temperature of the gas leaving the cylinder during the exhaust blowdown is given by the adiabatic expansion of the gas from the combustion chamber to the exhaust manifold,

$$T_{bd} = T_{evo}\left(\frac{P_{exh}}{P_{evo}}\right)^{\frac{\gamma-1}{\gamma}} \tag{4.9}$$

where T_{bd} refers to the exhaust temperature during the exhaust blowdown. Using (4.8) into (4.9), and replacing m_{ivc} by its expression (4.6), one obtains

$$T_{bd} = T_{ivc}\left(\frac{P_{exh}}{\alpha_1 P_{int}}\right)^{\frac{\gamma-1}{\gamma}}\left(1+\mu_1\frac{RQ_{LHV}m_f}{\alpha_1 c_v V_{ivc}P_{int}}\right)^{\frac{1}{\gamma}}$$

where $\mu_1 = \left(\frac{V_{comb}}{V_{ivc}}\right)^{\gamma-1}$. To simplify the model, V_{comb} can be taken as a function of the in-cylinder BGR at *ivc* considering the impact of the BGR on the combustion temperature. Finally, taking into account the heat losses in the exhaust runner (as is done in [67], e.g.), the dynamics of the temperature in the exhaust manifold can be written as

$$T_{exh}(k+1) = \mu_2 T_{ivc}(k) \left(\frac{P_{exh}(k)}{\alpha_1 P_{int}(k)}\right)^{\frac{\gamma-1}{\gamma}} \left(1 + \mu_1 \frac{RQ_{LHV} m_f(k)}{\alpha_1 c_v V_{ivc} P_{int}(k)}\right)^{\frac{1}{\gamma}} \tag{4.10}$$

where $\mu_2 < 1$ is a positive constant. The modeled exhaust temperature (4.10) can be compared against experimental measurements from a test bench. Figure 4.6 stresses the good representativeness of this model at steady-state over the whole engine operating range (notice that the transient behavior cannot be compared with real data because there is no high frequency measurement in the exhaust manifold).

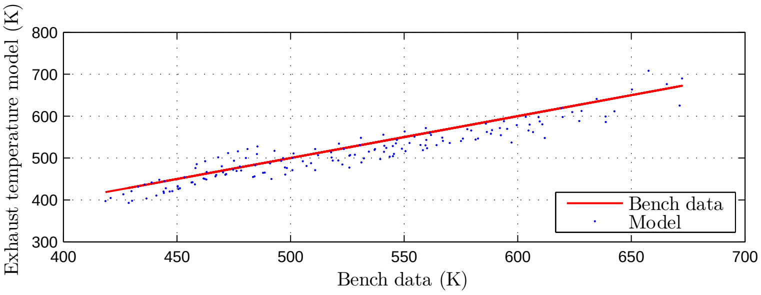

Figure 4.6: Comparisons between modeled and experimental exhaust temperature over the whole engine operating range. Experimental data obtained at test bench on a 4-cylinder CI engine equipped with VLD actuator and LP EGR capability.

4.1.3 Model summary

Figure 4.7 summarizes the relationship of the variables in the considered model (4.1)-(4.2)-(4.3)-(4.7)-(4.10). The quasi-static cylinder filling model (4.1) concerns two variables: the masses aspirated from the intake and from the exhaust as functions of the VLD actuator position, the engine speed, and the intake and exhaust manifold variables. Then, the in-cylinder composition and temperature model consists of a dilution model presented in (4.2) and (4.3) to reconstruct the in-cylinder BGR and temperature at *ivc*. Finally, the exhaust model derived in (4.7) and (4.10) is based on a simplified combustion model to estimate the exhaust composition and temperature.

4.1.4 Control-oriented rewriting of the model

Let $\Omega_{X_{exh}}$, $\Omega_{T_{exh}}$, $\Omega_{X_{ivc}}$ and $\Omega_{T_{ivc}}$ be the sets of practically feasible values of the exhaust BGR, exhaust temperature, in-cylinder BGR and temperature, respectively. Let us introduce the mappings $\xi : \Omega_{X_{ivc}} \times \Omega_{T_{ivc}} \to \Omega_{X_{exh}}$ and $\theta : \Omega_{T_{ivc}} \to \Omega_{T_{exh}}$ such that the exhaust BGR and the temperature dynamics given by models (4.7) and (4.10)

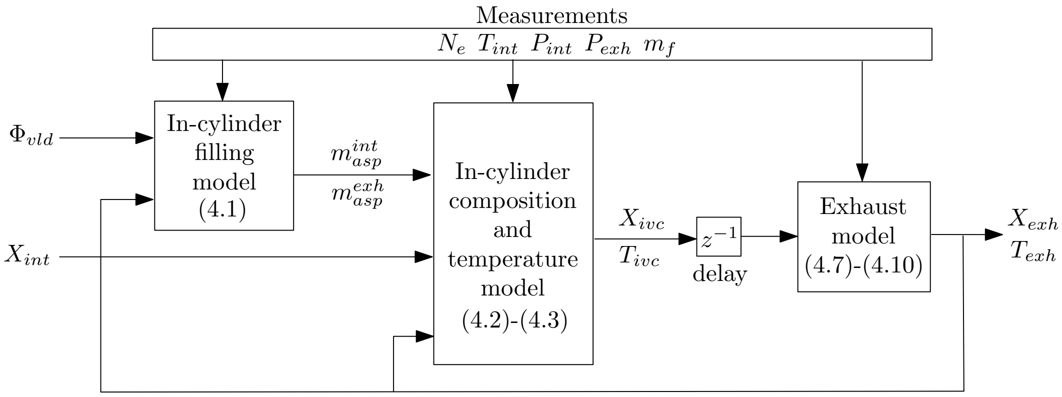
Measurements
N_e T_{int} P_{int} P_{exh} m_f
Φ_{vld}
In-cylinder filling model (4.1)
m_{asp}^{int}
m_{asp}^{exh}
X_{int}
In-cylinder composition and temperature model (4.2)-(4.3)
X_{ivc}
T_{ivc}
z^{-1}
delay
Exhaust model (4.7)-(4.10)
X_{exh}
T_{exh}

Figure 4.7: Schematic view of the in-cylinder BGR and temperature model.

write

$$\begin{cases} X_{exh}(k) \triangleq \xi(X_{ivc}(k-1), T_{ivc}(k-1)) \\ T_{exh}(k) \triangleq \theta(T_{ivc}(k-1)) \end{cases} \tag{4.11}$$

Again, notice that the discrete-time nature of system (4.11) stems from the valves closings which isolate the cylinder from the rest of the engine. Exhaust variables are depending on the in-cylinder variables of the previous combustion. Let $\Omega_{\Phi_{vld}}$ be the set of practically feasible values of the VLD actuator position. Let $f : \mathbb{R}^2 \rightarrow \mathbb{R}$ be a mapping representing the in-cylinder fraction of gases coming from the internal EGR (Ω_{iegr} being the set of practically feasible values of the function f)

$$f(\Phi_{vld}(k), \theta(T_{ivc}(k-1))) \triangleq \frac{m_{asp}^{exh}(k)}{m_{asp}^{int}(k) + m_{asp}^{exh}(k)} \tag{4.12}$$

Using mapping (4.12) into models (4.2) and (4.3) leads to the following dynamics

$$\begin{cases} X_{ivc}(k) = f(\Phi_{vld}(k), \theta(T_{ivc}(k-1)))\xi(X_{ivc}(k-1), T_{ivc}(k-1)) \\ \qquad\qquad + (1 - f(\Phi_{vld}(k), \theta(T_{ivc}(k-1))))X_{int}(k) \\ T_{ivc}(k) = f(\Phi_{vld}(k), \theta(T_{ivc}(k-1)))\theta(T_{ivc}(k-1)) \\ \qquad\qquad + (1 - f(\Phi_{vld}(k), \theta(T_{ivc}(k-1))))T_{int}(k) \end{cases} \tag{4.13}$$

Model properties

Owing to the structure of V_{evc} as function of Φ_{vld}, the function f defined in (4.12), which appears as a weight in the balance equations (4.13), possesses some interesting invertibility properties. In particular, the following partial-invertibility property holds.

Proposition 4.1.

For all $(T_{ivc}, X_{iegr}) \in \Omega_{T_{ivc}} \times \Omega_{iegr}$*, there exists a unique* $\Phi_{vld} \in \Omega_{\Phi_{vld}}$ *such that* $f(\Phi_{vld}, \theta(T_{ivc})) = X_{iegr}$*. inverse function* $\mathcal{F} : \Omega_{iegr} \times \Omega_{T_{exh}} \rightarrow \Omega_{\Phi_{vld}}$ *is defined such that for all* $T_{ivc} \in \Omega_T$*,*

$$f(\mathcal{F}(X_{iegr}, \theta(T_{ivc})), \theta(T_{ivc})) = X_{iegr} \tag{4.14}$$

Proof 4.1.

Let $\zeta : \mathbb{R}^2 \times \mathbb{R} \rightarrow \mathbb{R}$ be a class C^1 mapping such that $\zeta(\theta(T_{ivc}), X_{iegr}, \Phi_{vld}) = f(\Phi_{vld}, \theta(T_{ivc})) - X_{iegr}$. By definition, there exist a point $(\theta(T^0_{ivc}), X^0_{iegr}, \Phi^0_{vld}) \in W$ where W is an open set of $\mathbb{R}^3$ such that $\zeta(\theta(T^0_{ivc}), X^0_{iegr}, \Phi^0_{vld}) = 0$ (reference steady-state point). Figure 4.8 shows that at every engine operating point,

$$\left.\frac{\partial \zeta}{\partial \Phi_{vld}}\right|_{\theta(T^0_{ivc}), X^0_{iegr}, \Phi^0_{vld}} \neq 0$$

Then, from the implicit function theorem, there exist an open set $U = \Omega_{T_{exh}} \times \Omega_{iegr} \subset \mathbb{R}^2$, an open set $V = \Omega_{\Phi_{vld}} \subset \mathbb{R}$, and a class C^1 mapping $\mathcal{F} : U \rightarrow V$ such that

- for all $(\theta(T_{ivc}), X_{iegr}, \Phi_{vld}) \in U \times V$, one has

$$\zeta(\theta(T_{ivc}), X_{iegr}, \Phi_{vld}) = 0 \;\Rightarrow\; \Phi_{vld} = \mathcal{F}(\theta(T_{ivc}), X_{iegr})$$

- for all $(\theta(T_{ivc}), X_{iegr}, \Phi_{vld}) \in U$, one has

$$\zeta(\theta(T_{ivc}), X_{iegr}, \mathcal{F}(\theta(T_{ivc}), X_{iegr})) = 0$$

Then, from the definition of the function ζ, the proposition follows. ■

In practice, a VLD actuator can only admit bounded values. The inversion formula appearing in (4.14) may produce infeasible values that need to be saturated before they can be used as input signals to the VLD control system.

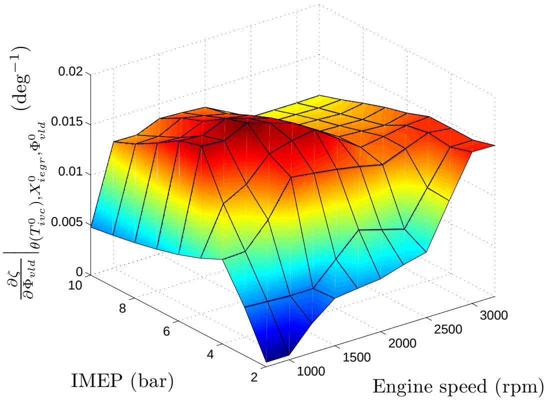

Figure 4.8: Numerical investigation of the sufficient condition for the implicit function theorem at each engine operating point.

4.2 Proposed control strategy

4.2.1 In-cylinder set points

The control objective is a set point to be tracked by the in-cylinder BGR, considering bounds on the in-cylinder temperature. Certainly, the in-cylinder BGR and temperature are equivalent, at steady state, to the VLD actuator position and the intake manifold BGR. However, during transients, it seems irrelevant to give the VLD actuator precise position set points based on static look-up tables which implicitly assume that the system is at rest. As already discussed at the beginning of the chapter, during these transient phases, instead of the VLD position, the actual control objective should be the in-cylinder BGR, because it directly impacts on the combustion, and, therefore, on pollutant emissions.

X^{sp}_{ivc} and T^{sp}_{ivc} are defined as the set points for the in-cylinder BGR and temperature given by the model (4.13), and by lookup tables experimentally derived through a steady-state calibration on a test bench (giving set points for the intake manifold BGR and VLD actuator position). Using (4.13), the set points are obtained by solving the following equations

$$\begin{cases} X^{sp}_{ivc} = f(\Phi^{sp}_{vld}, \theta(T^{sp}_{ivc}))\xi(X^{sp}_{ivc}, T^{sp}_{ivc}) + (1 - f(\Phi^{sp}_{vld}, \theta(T^{sp}_{ivc})))X^{sp}_{int} \\ T^{sp}_{ivc} = f(\Phi^{sp}_{vld}, \theta(T^{sp}_{ivc}))\theta(T^{sp}_{ivc}) + (1 - f(\Phi^{sp}_{vld}, \theta(T^{sp}_{ivc})))T_{int} \end{cases} \tag{4.15}$$

The solution to these two equations can be analytically obtained because the system (4.15) is triangular. In practice, one can first compute the in-cylinder temperature set point T^{sp}_{ivc} by solving the second equation of system (4.15), using the function f defined in (4.12) and the aspirated masses model (4.1). Then, one can compute the in-cylinder BGR set point X_{ivc}^{sp} by substituting the obtained value of T_{ivc}^{sp} in the first equation of (4.15). In real applications, measurements are used in these computations (intake manifold pressure and temperature, exhaust manifold pressure and engine speed).

The two control inputs, the intake manifold BGR, and the valve gear phasing have an impact on the outputs, X_{ivc} and T_{ivc}. It is then possible to achieve accurate control by inverting the model (4.13) of the in-cylinder BGR and temperature.

4.2.2 Coordination strategy

It is proposed to use the inverse model (4.14) outlined previously in Section 4.1.4 to compute set points for the low-level controllers. To account for the discussed slow response of the intake BGR subsystem, the two subsystems are coordinated by replacing the intake BGR target set point with a real-time estimation.

From an in-cylinder BGR set point X_{ivc}^{sp}, a VLD actuator position set point $\overline{\Phi_{vld}}$ is computed by inverting the dynamic model (4.13), using the function $\mathcal{F}$ defined in (4.14). In this formula, an estimate of the intake manifold BGR, X_{int} (several observers can be used to estimate this variable, as are proposed in [9], [84] and the references therein) is used. This gives

$$\overline{\Phi_{vld}}(k) = \mathcal{F}\left(\frac{X_{ivc}^{sp}(k) - X_{int}(k)}{\xi(X_{ivc}^{sp}(k-1), T_{ivc}^{sp}(k-1)) - X_{int}(k)}, \theta(T_{ivc}^{sp}(k-1))\right) \tag{4.16}$$

Notice that T_{ivc}^{sp} is used in place of its estimate T_{ivc} for sake of robustness. This permits to avoid creating a feedback loop coming from the estimation in the control law. For the set points computation (4.15), the same measured variables (intake manifold pressure and temperature, exhaust manifold pressure and engine speed) is used in the control strategy (4.16). In this way, there is no mismatch between the set points computation and the control law.

To limit the impact of the control strategy (4.16) onto the in-cylinder temperature (i.e. to limit smoke emissions), a saturation can be considered in the VLD actuator position trajectory generation. Let δ_T be the acceptable temperature overrun. A bound on the trajectory writes

$$\overline{\Phi_{vld}}(k) < \mathcal{F}\left(\frac{T_{ivc}^{sp}(k) + \delta_T - T_{int}(k)}{\theta(T_{ivc}^{sp}(k-1) + \delta_T) - T_{int}(k)}, \theta(T_{ivc}^{sp}(k-1) + \delta_T)\right) \tag{4.17}$$

Notice that there is no need to limit undershoots of in-cylinder temperature since they do not increase pollutant emissions.

In practical applications, the position of the valve gear is actuated by means of electronically controlled hydraulic devices. No details of low-level VLD controllers are given; the interested reader can refer to [18] or [8], for example.

4.2.3 Block structure

The presented control law (4.16)-(4.17) can be implemented under the form of the global closed-loop control scheme pictured in Figure 4.9. The set points formulas (4.15) and the control strategy are implemented in the high-level controller block. This block feeds the low-level controller handling the VLD actuator. Estimation of the intake manifold BGR (X_{int}) is used in the high-level controller to coordinate the low-level controllers by means of the reference signal $\overline{\Phi_{vld}}$ determined according to (4.16)-(4.17).

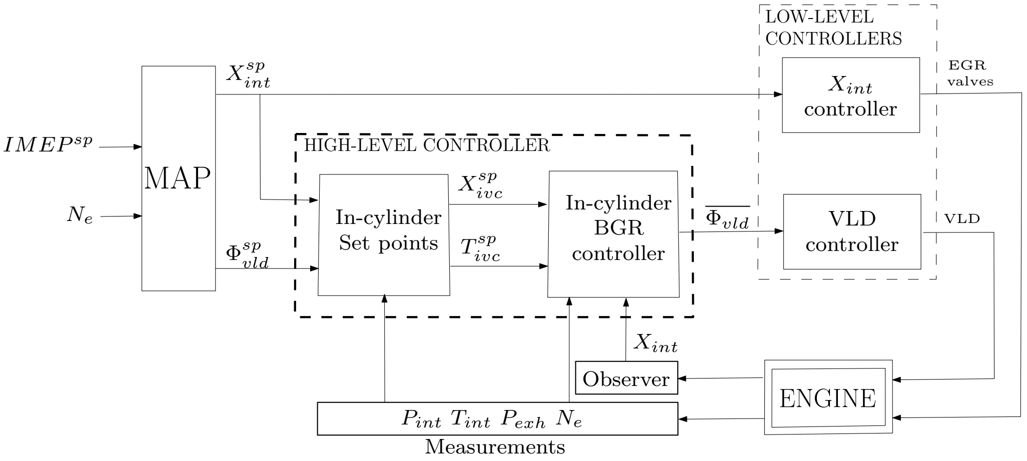
LOW-LEVEL CONTROLLERS
X^{sp}_{int}
EGR valves
X_{int} controller
$IMEP^{sp}$
MAP
N_e
Φ^{sp}_{vld}
HIGH-LEVEL CONTROLLER
In-cylinder Set points
X^{sp}_{ivc}
T^{sp}_{ivc}
In-cylinder BGR controller
$\overline{\Phi_{vld}}$
VLD controller
VLD
X_{int}
Observer
ENGINE
P_{int} T_{int} P_{exh} N_e
Measurements

Figure 4.9: Control scheme. The in-cylinder set points X^{sp}_{ivc} and T^{sp}_{ivc} are given in Section 4.2.1. The high-level controller coordinates the low-level controllers using the control law presented in Section 4.2.2 to determine VLD actuator trajectory $\overline{\Phi_{vld}}$.

In the control strategy, the cylinder filling model is inverted in order to satisfy the high-level requirements during transients. In this way, potential modeling errors can be canceled and do not alter engine working during steady-state conditions. However, as a feedback loop has been introduced in the control strategy, stability of the system can be questioned.

4.2.4 Stability analysis

The closed loop discrete-time dynamics consisting of the model (4.13) and the coordinated controller (4.16) is now studied. Note $\boldsymbol{x} \triangleq [X_{ivc}\ T_{ivc}]^T$ the states of the system.

System (4.13) rewrites

$$\begin{cases} x_1(k) = f(\Phi_{vld}(k), \theta(x_2(k-1)))\xi(x_1(k-1), x_2(k-1)) \\ \qquad\qquad + (1 - f(\Phi_{vld}(k), \theta(x_2(k-1))))X_{int}(k) \\ x_2(k) = f(\Phi_{vld}(k), \theta(x_2(k-1)))\theta(x_2(k-1)) \\ \qquad\qquad + (1 - f(\Phi_{vld}(k), \theta(x_2(k-1))))T_{int}(k) \end{cases} \tag{4.18}$$

Equivalently, the error dynamics is now studied.

Error system

The control law (4.16) is such that the following relation holds (using the property (4.14))

$$f(\overline{\Phi_{vld}}(k), \theta(x_2^{sp})) = \frac{x_1^{sp} - X_{int}(k)}{\xi(x_1^{sp}, x_2^{sp}) - X_{int}(k)}$$

This leads to

$$x_1^{sp} = f(\overline{\Phi_{vld}}(k), \theta(x_2^{sp}))\xi(x_1^{sp}, x_2^{sp}) + (1 - f(\overline{\Phi_{vld}}(k), \theta(x_2^{sp})))X_{int}(k) \tag{4.19}$$

Then, note $\tilde{x} \triangleq x - x^{sp}$ the error between the state and its set point. Comparing (4.18) and (4.19) gives

$$\begin{aligned} \tilde{x}_1(k) = {} & f(\Phi_{vld}(k), \theta(x_2(k-1)))\xi(x_1(k-1), x_2(k-1)) \\ & - f(\overline{\Phi_{vld}}(k), \theta(x_2^{sp}(k-1)))\xi(x_1^{sp}, x_2^{sp}) \\ & - X_{int}(k)\left(f(\Phi_{vld}(k), \theta(x_2(k-1))) - f(\overline{\Phi_{vld}}(k), \theta(x_2^{sp}))\right) \end{aligned} \tag{4.20}$$

The (fast) VLD actuator dynamics is now neglected, i.e. $\Phi_{vld} = \overline{\Phi_{vld}}$. Then, linearizing equation (4.20) leads to

$$\tilde{x}_1(k) \simeq a(k)\tilde{x}_1(k-1) + b(k)\tilde{x}_2(k-1) \tag{4.21}$$

where

$$a(k) = f(\overline{\Phi_{vld}}(k), \theta(x_2^{sp})) \left.\frac{\partial \xi}{\partial x_1}\right|_{x_1^{sp}, x_2^{sp}} \tag{4.22a}$$

$$b(k) = \left.\frac{\partial f}{\partial x_2}\right|_{\overline{\Phi_{vld}}(k), x_2^{sp}} \cdot (\xi(x_1^{sp}, x_2^{sp}) - X_{int}(k)) + f(\overline{\Phi_{vld}}(k), \theta(x_2^{sp})) \left.\frac{\partial \xi}{\partial x_2}\right|_{x_1^{sp}, x_2^{sp}} \tag{4.22b}$$

On the other hand, the difference between equations (4.18) and (4.15) gives

$$\begin{aligned}\tilde{x}_2(k) = {} & f(\Phi_{vld}(k), \theta(x_2(k-1)))\theta(x_2(k-1)) - f(\Phi_{vld}^{sp}, \theta(x_2^{sp}))\theta(x_2^{sp}) \\ & - T_{int}(k)(f(\Phi_{vld}(k), \theta(x_2(k-1))) - f(\Phi_{vld}^{sp}, \theta(x_2^{sp})))\end{aligned} \tag{4.23}$$

Let $\tilde{\Phi}_{vld} \triangleq \overline{\Phi_{vld}} - \Phi_{vld}^{sp} = \Phi_{vld} - \Phi_{vld}^{sp}$ be the error between the VLD actuator position and its set point coming from a look-up table (see Figure 4.9). Then, linearizing equation (4.23) leads to

$$\tilde{x}_2(k) \simeq c(k)\tilde{x}_2(k-1) + (\theta(x_2^{sp}) - T_{int}(k)) \left.\frac{\partial f}{\partial \Phi_{vld}}\right|_{\Phi_{vld}^{sp}, x_2^{sp}} \tilde{\Phi}_{vld}(k) \tag{4.24}$$

where

$$c(k) = f(\Phi_{vld}^{sp}, \theta(x_2^{sp})) \left.\frac{\partial \theta}{\partial x_2}\right|_{x_2^{sp}} + (\theta(x_2^{sp}) - T_{int}(k)) \left.\frac{\partial f}{\partial x_2}\right|_{\Phi_{vld}^{sp}, x_2^{sp}} \tag{4.25}$$

To express the VLD actuator position error $\tilde{\Phi}_{vld}$ as a function of the intake manifold BGR, the difference between equation (4.19) and in-cylinder BGR set point definition (4.15) is computed. This gives the following equation

$$\begin{aligned}& f(\overline{\Phi_{vld}}(k), \theta(x_2^{sp}))\xi(x_1^{sp}, x_2^{sp}) - f(\Phi_{vld}^{sp}, \theta(x_2^{sp}))\xi(x_1^{sp}, x_2^{sp}) \\ & - (f(\overline{\Phi_{vld}}(k), \theta(x_2^{sp}))X_{int}(k) - f(\Phi_{vld}^{sp}, \theta(x_2^{sp}))X_{int}^{sp}) + X_{int}(k) - X_{int}^{sp}(k) = 0\end{aligned} \tag{4.26}$$

Let $\tilde{X}_{int} \triangleq X_{int} - X_{int}^{sp}$ be the error between the intake manifold BGR and its look-up table set point (see Figure 4.9). Then, assuming slow variations of x^{sp}, linearizing equation (4.26) leads to

$$\tilde{\Phi}_{vld}(k) \simeq \frac{f(\Phi_{vld}^{sp}, \theta(x_2^{sp})) - 1}{\xi(x_1^{sp}, x_2^{sp}) - X_{int}^{sp}} \left(\left.\frac{\partial f}{\partial \Phi_{vld}}\right|_{\Phi_{vld}^{sp}, x_2^{sp}} \right)^{-1} \tilde{X}_{int}(k) \tag{4.27}$$

Finally, gathering error equations (4.21) and (4.24), and replacing (4.27) in (4.24) yields the following discrete-time linear time-varying forced error system

$$\begin{cases} \tilde{x}_1(k) = a(k)\tilde{x}_1(k-1) + b(k)\tilde{x}_2(k-1) \\ \tilde{x}_2(k) = c(k)\tilde{x}_2(k-1) + d(k)\tilde{X}_{int}(k) \end{cases} \tag{4.28}$$

where

$$d(k) = (\theta(x_2^{sp}) - T_{int}(k)) \left(f(\Phi_{vld}^{sp}, \theta(x_2^{sp})) - 1\right) \left(\xi(x_1^{sp}, x_2^{sp}) - X_{int}^{sp}\right)^{-1} \tag{4.29}$$

The stability of this system is now studied.

Stability of the unforced system

The approach of Jiang in [31] is followed to study the stability of the discrete event system in a ISS way. Before proving stability of the forced system (4.28), consider the following result about stability of discrete-time cascade systems inspired by the continuous case proposed in [34].

Lemma 4.1.

Consider the cascade (unforced) discrete-time system

$$\boldsymbol{x}_1(k+1) = f_1(\boldsymbol{x}_1(k), \boldsymbol{x}_2(k)) \tag{4.30}$$

$$\boldsymbol{x}_2(k+1) = f_2(\boldsymbol{x}_2(k)) \tag{4.31}$$

with state $\boldsymbol{x} \triangleq [\boldsymbol{x}_1 \ \boldsymbol{x}_2]^T \in \mathbb{R}^{n_1} \times \mathbb{R}^{n_2}$*, for some* n_1 *and* n_2*, and for each time instant* $k \in \mathbb{Z}^+$*.* $f_1 : \mathbb{R}^{n_1} \times \mathbb{R}^{n_2} \to \mathbb{R}^{n_1}$ *and* $f_2 : \mathbb{R}^{n_2} \to \mathbb{R}^{n_2}$ *are continuous. If the system (4.30), with* $\boldsymbol{x}_2$ *as input, is ISS (Input-to-State Stable in the sense of [31]) and the origin of (4.31) is UGAS (Uniformly Globally Asymptotically Stable), then the origin of the cascade system (4.30) and (4.31) is globally uniformly asymptotically stable.*

Proof 4.2.

The proof follows along the line of [34]. By assumption, let $k_0 > 0$ be the initial time. The solutions of (4.30) and (4.31) satisfy

$$\|\boldsymbol{x}_1(k)\| \leq \beta_1(\|\boldsymbol{x}_1(s)\|, k-s) + \gamma_1\left(\sup_{s \leq n \leq k} \|\boldsymbol{x}_2(n)\|\right) \tag{4.32}$$

$$\|\boldsymbol{x}_2(k)\| \leq \beta_2(\|\boldsymbol{x}_2(s)\|, k-s) \tag{4.33}$$

globally, where $k \geq s \geq k_0$, β_1, β_2 are class $\mathcal{KL}$ functions, and γ_1 is a class $\mathcal{K}$ function. Apply (4.32) with $s = (k+k_0)/2$ to obtain

$$\|\boldsymbol{x}_1(k)\| \leq \beta_1\left(\left\|\boldsymbol{x}_1\left(\frac{k+k_0}{2}\right)\right\|, \frac{k-k_0}{2}\right) + \gamma_1\left(\sup_{\frac{k+k_0}{2} \leq n \leq k} \|\boldsymbol{x}_2(n)\|\right) \tag{4.34}$$

To estimate $\boldsymbol{x}_1((k+k_0)/2)$, apply (4.32) with $s = k_0$ and k replaced by $(k+k_0)/2$ to obtain

$$\left\| \boldsymbol{x}_1 \left(\frac{k+k_0}{2} \right) \right\| \leq \beta_1 \left(\|\boldsymbol{x}_1(k_0)\|, \frac{k-k_0}{2} \right) + \gamma_1 \left(\sup_{k_0 \leq n \leq \frac{k+k_0}{2}} \|\boldsymbol{x}_2(n)\| \right) \tag{4.35}$$

Using (4.33), one obtains

$$\sup_{k_0 \leq n \leq \frac{k+k_0}{2}} \|\boldsymbol{x}_2(n)\| \leq \beta_2 \left(\|\boldsymbol{x}_2(k_0)\|, 0 \right) \tag{4.36}$$

$$\sup_{\frac{k+k_0}{2} \leq n \leq k} \|\boldsymbol{x}_2(n)\| \leq \beta_2 \left(\|\boldsymbol{x}_2(k_0)\|, \frac{k-k_0}{2} \right) \tag{4.37}$$

Substituting (4.35) through (4.37) into (4.34), and using the inequalities

$$\|\boldsymbol{x}_1(k_0)\| \leq \|\boldsymbol{x}(k_0)\|, \ \|\boldsymbol{x}_2(k_0)\| \leq \|\boldsymbol{x}(k_0)\|, \ \|\boldsymbol{x}(k_0)\| \leq \|\boldsymbol{x}_1(k_0)\| + \|\boldsymbol{x}_2(k_0)\|$$

yields

$$\|\boldsymbol{x}(k)\| \leq \beta(\|\boldsymbol{x}(k_0)\|, k-k_0)$$

where

$$\beta(r,s) = \beta_1 \left(\beta_1 \left(r, \frac{s}{2} \right) + \gamma_1(\beta_2(r,0)), \frac{s}{2} \right) + \gamma_1 \left(\beta_2 \left(r, \frac{s}{2} \right) \right) + \beta_2(r,s)$$

It can be readily verified that β is a class $\mathcal{KL}$ function for all $r \geq 0$. Hence, the origin of (4.30) and (4.31) is globally uniformly asymptotically stable. ■

To prove stability of the error system (4.28), the following unforced system is first considered

$$\begin{cases} \tilde{x}_1(k) = a(k)\tilde{x}_1(k-1) + b(k)\tilde{x}_2(k-1) \\ \tilde{x}_2(k) = c(k)\tilde{x}_2(k-1) \end{cases} \tag{4.38}$$

Then, following result about the stability of discrete-time cascade systems is used. Analyzing the stability of the cascade system (4.38) through Lemma 4.1 leads to the following proposition.

Proposition 4.2.
The origin of the unforced cascade system (4.38) is Uniformly Globally Asymptotically Stable (UGAS).

Proof 4.3.

One begins with the subsystem $\tilde{x}_2$. The solution of the discrete equation reads

$$\tilde{x}_2(k) = \left(\prod_{i=1}^{k} c(i)\right) \tilde{x}_2(0)$$

Then, the following inequality holds

$$\|\tilde{x}_2(k)\| \leq \left(\sup_{i\in[1;k]} \|c(i)\|\right)^k \|\tilde{x}_2(0)\|$$

Figure 4.10 pictures the function $\|c\|$ given by (4.25). It shows that over the whole engine operating range, $\|c\|$ remains below to 1. Then, for all $k \in \mathbb{Z}^+$, $\|c(k)\| < 1$. Applying the ISS definition given in [31] to the zero-input subsystem in $\tilde{x}_2$, the latter is deduced to be UGAS.

One now focuses on the subsystem $\tilde{x}_1$. The solution of the discrete equation reads

$$\tilde{x}_1(k) = \left(\prod_{i=1}^{k} a(i)\right) \tilde{x}_1(0) + \sum_{j=1}^{k} \left(b(j)\tilde{x}_2(j-1) \prod_{i=j+1}^{k} a(i)\right) \tag{4.39}$$

The second term of the right-hand side of Eq. (4.39) can be bounded by

$$\begin{aligned}
&\left\|\sum_{j=1}^{k} \left(b(j)\tilde{x}_2(j-1) \prod_{i=j+1}^{k} a(i)\right)\right\| \\
&\qquad \leq \sup_{i\in[1;k]} \|b(i)\| \sup_{i\in[0;k-1]} \|\tilde{x}_2(i)\| \sum_{j=1}^{k} \left(\sup_{i\in[j+1;k]} \|a(i)\|\right)^{k-j} \\
&\qquad \leq \sup_{i\in[1;k]} \|b(i)\| \sup_{i\in[0;k-1]} \|\tilde{x}_2(i)\| \sum_{j=0}^{k-1} \left(\sup_{i\in[0;k-1]} \|a(i)\|\right)^{j}
\end{aligned}$$

Using the definition of the geometric series, the following inequality holds

$$\|\tilde{x}_1(k)\| \leq \left(\sup_{i\in[1;k]} \|a(i)\|\right)^k \|\tilde{x}_1(0)\| + \gamma(a_{[k-1]}, b_{[k-1]}) \sup_{i\in[0;k-1]} \|\tilde{x}_2(i)\|$$

where $\gamma(a_{[k-1]}, b_{[k-1]}) = \sup_{i\in[1;k]} \|b(i)\| \frac{1-\left(\sup_{i\in[0;k-1]}\|a(i)\|\right)^k}{1-\left(\sup_{i\in[0;k-1]}\|a(i)\|\right)}$. Classically, $a_{[k-1]}$ (respectively $b_{[k-1]}$) denotes the truncation of a (b) at $k-1$.

On the one hand, parameter $\|a\|$ is clearly below 1. Indeed, (4.22a) can be simplified because $\left.\frac{\partial \xi}{\partial x_1}\right|_{x_1^{sp}, x_2^{sp}} = 1$ (see (4.7)) and function f represents the fraction of the in-cylinder gases coming from the exhaust (see (4.12)). On the other hand, the parameter $\|b\|$ is bounded as is evidenced by its expression (4.22b). Indeed, it is only a function of the engine operating point and of the intake manifold BGR X_{int} which is a bounded variable.

Then, for all $k \in \mathbb{Z}^+$, $\|a(k)\| < 1$ and $\sup_{i\in[1;k]} \|b(i)\| < \infty$. Applying the ISS definition given in [31] to the subsystem in $\tilde{x}_1$, one deduces that the latter is ISS.

Finally, the subsystem in $\tilde{x}_1$, with $\tilde{x}_2$ as input, is ISS and the origin of the subsystem in $\tilde{x}_2$ is UGAS. Then, applying Lemma 4.1, the origin of the cascade system (4.38) is UGAS. ■

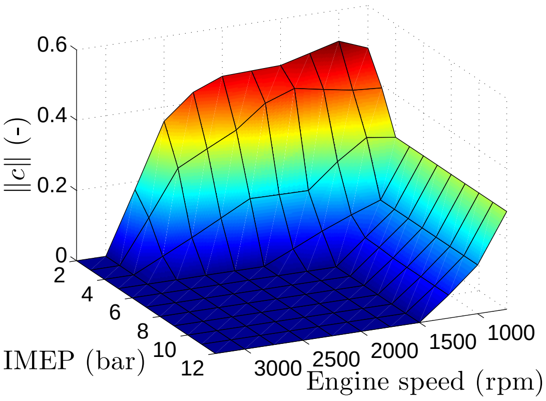

Figure 4.10: Parameter $\|c\|$ over the engine operating range.

Stability of the forced system

Let $\tilde{\boldsymbol{x}} = [\tilde{x}_1 \; \tilde{x}_2]^T$. Now, the following cascade system which is a simple rewriting of the forced dynamics (4.28) is considered

$$\begin{cases} \tilde{\boldsymbol{x}}(k) = \boldsymbol{M}_1(k)\tilde{\boldsymbol{x}}(k-1) + \boldsymbol{M}_2(k)\tilde{X}_{int}(k) \\ \tilde{X}_{int}(k) = h(\tilde{X}_{int}(k-1)) \end{cases} \tag{4.40}$$

where $\boldsymbol{M}_1(k) \triangleq \begin{pmatrix} a(k) & b(k) \\ 0 & c(k) \end{pmatrix}$, $\boldsymbol{M}_2(k) \triangleq \begin{pmatrix} 0 \\ d(k) \end{pmatrix}$, and h is a mapping giving the intake manifold BGR error dynamics. As the low-level intake BGR controller is not the topic of this work, here it is only assumed that the controller is efficient and that the error system is UGAS [7]. Therefore, $\tilde{X}_{int}(k)$ converges to zero as $k \to \infty$.

Analyzing the stability of the cascade system (4.40) leads to the following proposition.

Proposition 4.3.
The origin of the cascade system (4.40) is Uniformly Globally Asymptotically Stable (UGAS).

Proof 4.4.
One focuses on the dynamics of $\tilde{\boldsymbol{x}}$, and, first, consider the following unforced system

$$\boldsymbol{x}(k) = \boldsymbol{M}_1(k)\tilde{\boldsymbol{x}}(k-1) \tag{4.41}$$

From Proposition 4.2, the unforced system (4.41) is UGAS. Then, from [34, Lemma 4.5] there exist a class $\mathcal{KL}$ function β such that for every $\boldsymbol{x}(k_0)$

$$\|\boldsymbol{x}(k)\| \leq \beta\left(\|\boldsymbol{x}(k_0)\|, k-k_0\right), \quad \forall k \geq k_0 \geq 0 \tag{4.42}$$

Now, consider the following forced system

$$\boldsymbol{x}(k) = \boldsymbol{M}_1(k)\tilde{\boldsymbol{x}}(k-1) + \boldsymbol{M}_2(k)u(k) \tag{4.43}$$

The input matrix $\|\boldsymbol{M}_2\| = \|d\|$ is bounded as is evidenced by its expression (4.29). Indeed, it depends on the engine operating point, and on the intake temperature T_{int} which is a bounded variable. Then, from (4.42) and from the linearity of (4.43), there exists a class $\mathcal{K}$ function γ such that

$$\|\boldsymbol{x}(k)\| \leq \beta\left(\|\boldsymbol{x}(k_0\|, k-k_0\right) + \gamma\left(\sup_{k_0 \leq s \leq k} \|u(s)\|\right)$$

Then, from Definition 2, the system (4.43) is ISS.

Finally, the dynamics of $\tilde{\boldsymbol{x}}$, with $\tilde{X}_{int}$ as input, is ISS and the origin of the subsystem $\tilde{X}_{int}$ is UGAS. Then, applying Lemma 4.1, the origin of the cascade system (4.40) is UGAS. ■

4.3 Experimental results

Now, the control technique proposed in Section 4.2 is evaluated on an experimental test bench.

4.3.1 Engine setup

The engine used throughout the experiments is a 1.6 L four-cylinder direct injection HCCI-LTC CI engine. The second valve lift is provided by a Mechadyne$^{\mathrm{TM}}$ system [40] allowing a second lift between 0 and 4 mm. External EGR is carried out by a low-pressure circuit. The engine specifications are given in Table 4.1.

Engine type	Renault H9M
Number of cylinders	4
Bore × Stroke	79 × 81.5 mm
Compression ratio	16:1
Engine Displacement	1.6 Liters
Injection	Piezo
Exhaust valve closing (first lift)	17 degATDC
Re-breathing lift closing	20 (no re-opening) / 60 degATDC

Table 4.1: Experimental CI engine setup

4.3.2 Intake manifold BGR variation

The first sequence of experimental tests considers an intake manifold BGR variation, while trying to keep a constant in-cylinder BGR. The goal of such an experiment is to validate the model and the control strategy under steady-state conditions. In Figure 4.11, the solid blue curves designate the reference control strategy (named “ref”, presented in Section 1.3.4), and the dashed red curves refer to the proposed control strategy (noted “strat”, presented in Section 4.2.2).

Figure 4.11(a) reports the exhaust valve position variation trajectory that are imposed in both cases. Figure 4.11(c) presents the resulting intake manifold BGR response. Note that the mismatch between the two curves arises from the differences in VLD positions between the two strategies. Figure 4.11(d) gives the VLD actuator trajectory. In the reference strategy, the VLD actuator is set to its position mapped according to the engine operating point. In the proposed strategy, the VLD actuator trajectory (given by the control law (4.16)) moves away from its reference position to satisfy the in-cylinder BGR demand. Figure 4.11(e) shows that the in-cylinder BGR request is kept constant during the whole test (except around 120 s because of the VLD actuator saturation). Figure 4.11(f) stresses that the VLD actuator position variations lead to strong in-cylinder temperature variations. Finally, Figure 4.11(b) presents the

NO$_x$ emissions obtained using the two strategies. The proposed strategy succeeds in keeping the emissions constant.

This experiment highlights two facts. First, the in-cylinder BGR is the relevant control variable for NO$_x$ emissions control purposes. Second, the designed in-cylinder composition model is consistent with reality.

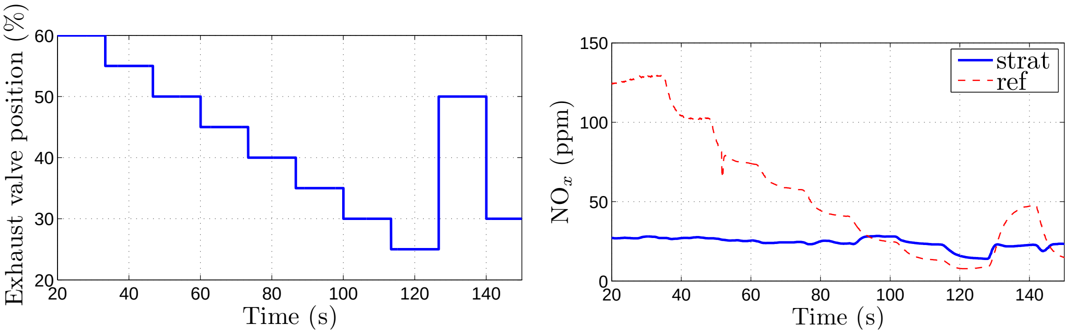

(a) Exhaust valve position (b) NO$_x$ emissions

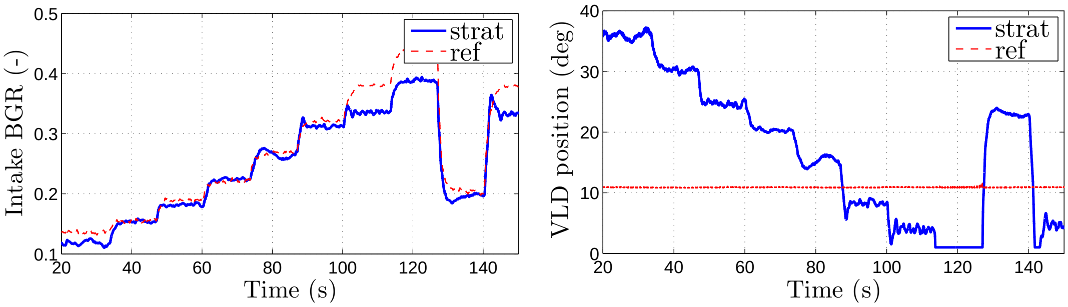

(c) Intake BGR (d) VLD actuator position

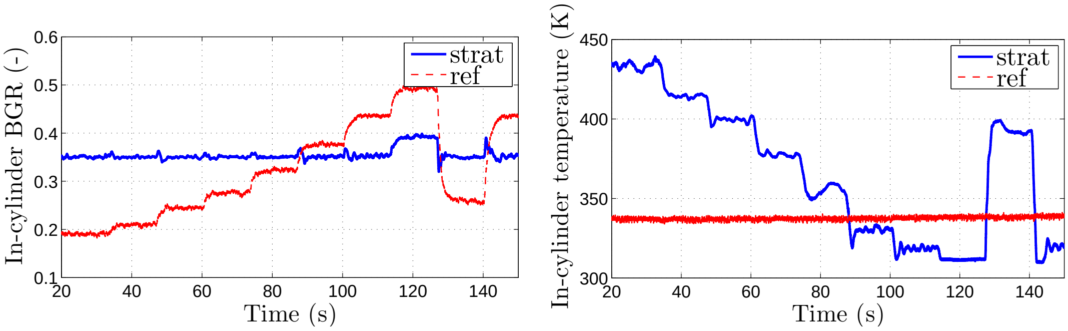

(e) In-cylinder BGR (f) In-cylinder temperature

Figure 4.11: Test-bench results for a four-cylinder CI engine for exhaust valve position variations at constant speed of 1500 rpm with and without the proposed control strategy. The controller succeeds in keeping the in-cylinder BGR constant, and; consequently; the NO$_x$ emissions.

In Figure 4.12, the NO_x emissions and the middle of combustion (referred to as CA_{50}) variations are analyzed, in comparison with the reference operating point. It is seen that with a VLD compensation, NO_x emissions and CA_{50} are kept around their reference values.

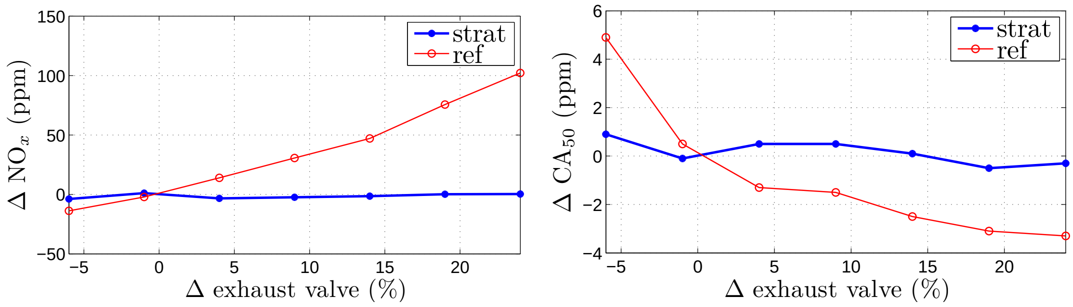

(a) NO_x emissions

(b) Middle of combustion

Figure 4.12: Variation of NO_x emissions and middle of combustion (CA_{50}) relative to an exhaust valve position variation. Point $(0, 0)$ refers to the reference engine operating point.

4.3.3 Torque transients

The second sequence of experimental tests consists of torque trajectories composed of increasing and decreasing torque requests. These experiments are conducted at a constant engine speed of 1500 rpm (Figure 4.13) and 1000 rpm (Figure 4.14), respectively. In both cases, the reference control strategy (named “ref”) and the proposed control strategy (named “strat”) are compared.

The following comments hold for Figure 4.13 and Figure 4.14 as well. The low-level control variables (the intake BGR and the VLD actuator) are given in the two middle figures. The intake manifold BGR is controlled by its low-level controller. It behaves similarly with the two different control strategies (“ref” and “strat”, respectively). Yet, the VLD actuator trajectories are strongly different in the two cases. Indeed, using the reference controller, the VLD trajectory Φ_{vld}^{sp} is only based on a static look-up table depending on the engine operating point. By contrast, in the proposed strategy, the VLD trajectory $\overline{\Phi_{vld}}$ is continuously updated during transients to satisfy the in-cylinder BGR objective. This can be seen in the bottom-left figure where the in-cylinder BGR tracks well its set point (which is not the case for the reference controller). Simultaneously, the in-cylinder temperature drifts away from its set point due to the change in the EGR/IEGR trade-off. Finally, the top-right figures give results on NO_x

emissions. One can see that the whole system tends to move closer to the steady-state conditions with the proposed trajectory. This permits to prevent the undesired NO_x emissions peaks during torque tips-in (especially during increasing intake manifold BGR demands).

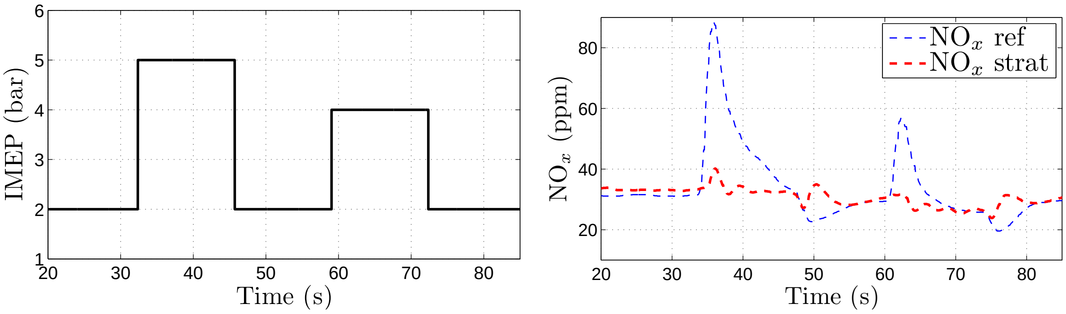

(a) IMEP trajectory

(b) NO_x emissions

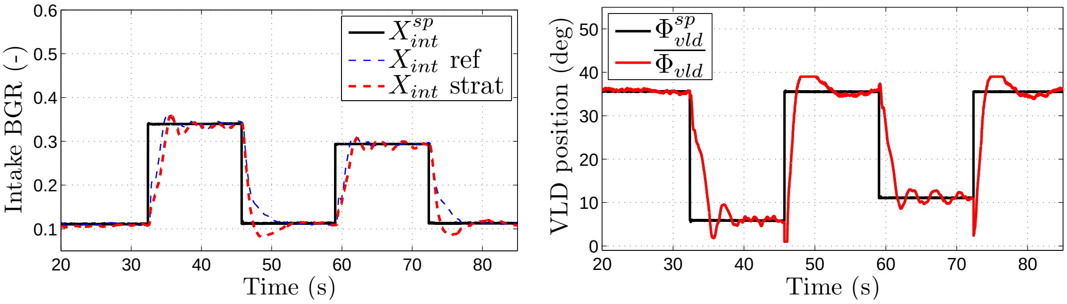

(c) Intake BGR

(d) VLD actuator position

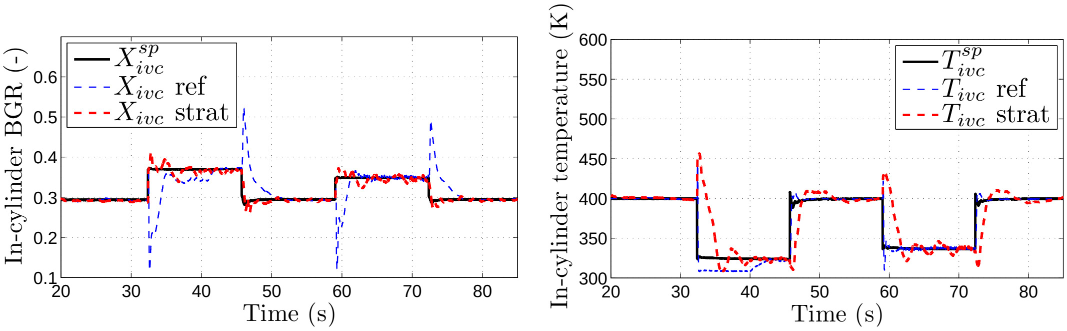

(e) In-cylinder BGR

(f) In-cylinder temperature

Figure 4.13: Test-bench results for a four-cylinder CI engine for step torque demand at constant speed of 1500 rpm with and without the proposed control strategy. The controller succeeds in tracking the in-cylinder BGR set point. Consequently, the NO_x emissions peaks are reduced.

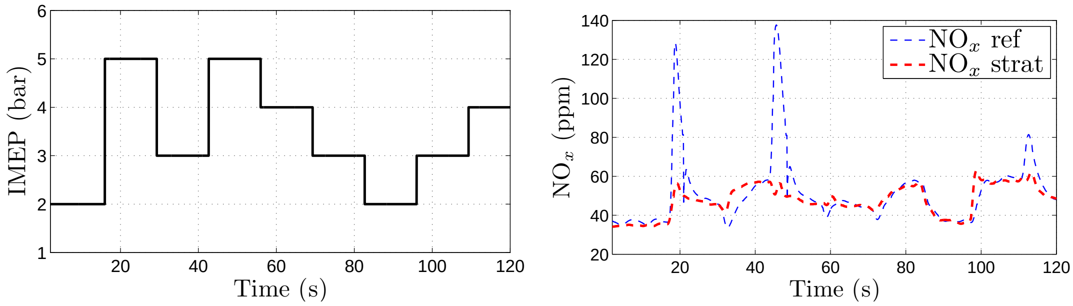

(a) IMEP trajectory (b) NO$_x$ emissions

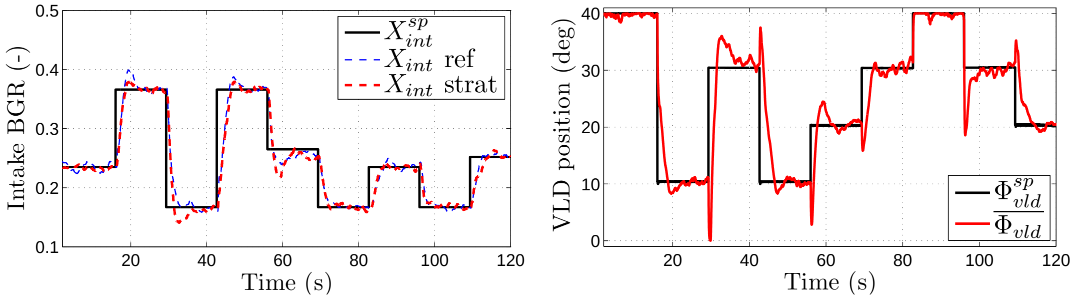

(c) Intake BGR (d) VLD actuator position

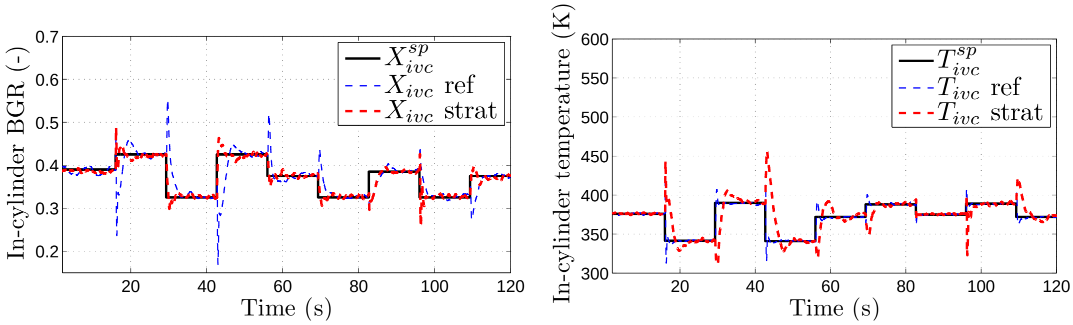

(e) In-cylinder BGR (f) In-cylinder temperature

Figure 4.14: Test-bench results for a four-cylinder CI engine for step torque demand at constant speed of 1000 rpm with and without the proposed control strategy. The controller succeeds in tracking the in-cylinder BGR set point. Consequently, the NO$_x$ emissions peaks are reduced.

In Figure 4.15, the impact of the in-cylinder temperature increase during transients on the smoke emissions is analyzed. The experiment is realized at 1000 rpm, and the torque transients correspond to a part of the experiments in Figure 4.14. Figure 4.15(b), Figure 4.15(c) and Figure 4.15(d) show the VLD actuator trajectory, the NO$_x$ emissions, and the smoke emissions (through the opacity measurement) respectively. The four curves in the figures represent the reference strategy (“ref”), the proposed strategy without any in-cylinder temperature excursion limitation ("no sat"), the proposed strategy with an in-cylinder temperature excursion limitation of 50 K ("$\delta T = 50$"), and the proposed strategy with an in-cylinder temperature excursion limitation of 25 K ("$\delta T = 25$"). These results show that, without taking into account the in-cylinder temperature excursions, the smoke emissions are increased with the proposed strategy. Nevertheless, the saturated control strategy (control law (4.16)-(4.17)) permits to limit the in-cylinder temperature excursions, and so the smoke emission, while keeping a large part of the NO_x emissions gains.

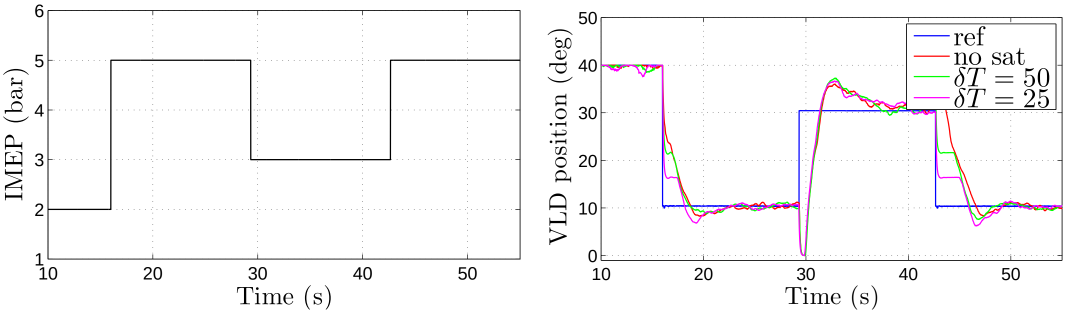

(a) IMEP trajectory (b) VLD actuator position

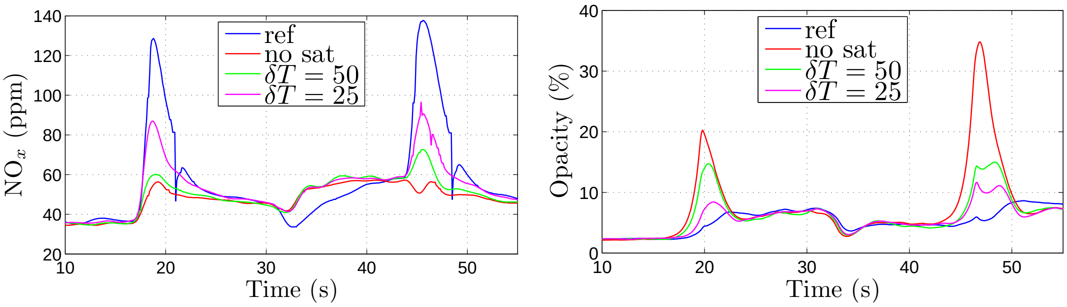

(c) NO_x emissions (d) Opacity emissions

Figure 4.15: Test-bench results for a four-cylinder CI engine for step torque demand at constant speed of 1000 rpm with and without the proposed control strategy. Taking into account an in-cylinder temperature limitation in the control strategy permits to decrease the losses in smoke emissions while keeping the gains in NO_x emissions.

4.3.4 ECE driving cycle

To obtain estimates of the emissions actually produced under representative driving conditions, experiments were conducted on a dynamic test bench. The goal of the dynamic test bench is to reproduce the vehicle behavior. In that case, the engine powers a drive train physical simulator reproducing the behavior of the clutch, the transmission, a vehicle model, and a driver model (considered as controlling the position of the acceleration pedal) sending a torque request to the engine control unit.

Figure 4.16 reports results on a urban driving cycle (ECE), which is a part of the New European driving cycle (NEDC). Figure 4.16(a) gives the vehicle speed and engine speed. Figure 4.16(b) and Figure 4.16(c) show the VLD trajectories and the NO_x emissions for both reference and proposed control strategies. NO_x emissions are reduced during large transients.

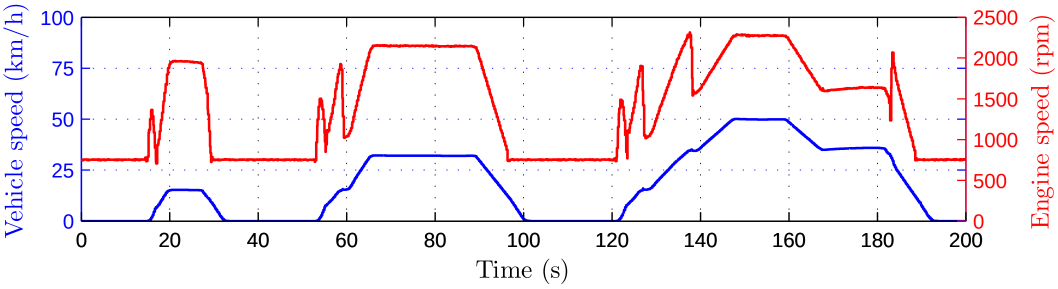

(a) Vehicle and engine speed

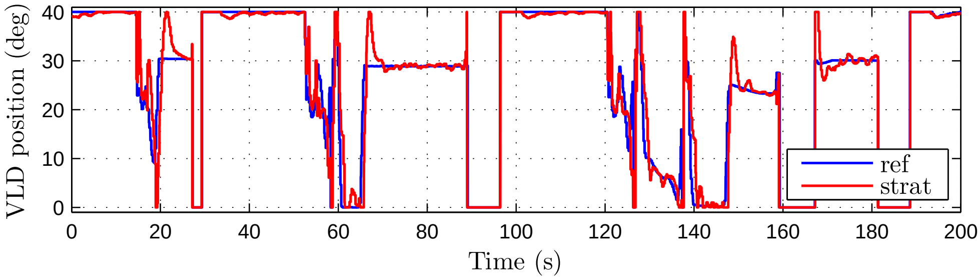

(b) VLD actuator position

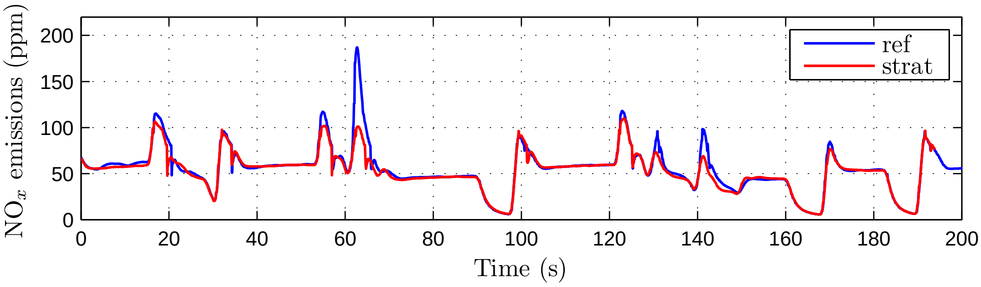

(c) NO_x emissions

Figure 4.16: Test-bench results for a four-cylinder CI engine for an ECE driving cycle with and without the proposed control strategy. NO_x emissions are reduced during transients.

4.4 Conclusion on the obtained results

A control strategy specifically designed to handle transients of turbocharged CI engines equipped with VLD actuator and LP EGR loop has been presented.

To reduce pollutant emissions, the BGR contained in the combustion chamber at *ivc* is controlled. A model of in-cylinder BGR and temperature has been presented. It uses the breathing model designed in Chapter 2 completed by a dilution and a simple combustion model. This model is shown to have interesting invertibility properties from which a control strategy has been developed. It is an add-on to an existing control strategy. The strategy permits to accelerate the in-cylinder BGR response by coordinating two variables acting on the breathing process, i.e. the intake manifold BGR and the positions of the VLD actuator. To account for in-cylinder temperature excursions during transients, the VLD control law is saturated. Because the coordination implies a cascaded discrete-time system, the stability has been theoretically analyzed using the ISS theory.

The strategy has been tested on a test bench. The experimental results have stressed the relevance of the control strategy. A significant reduction of the NO_x emissions during transients has been obtained.

Chapter 5

Conclusions and perspectives

Over the last years, variable valve actuation devices have proved their beneficial impact on consumption and pollutant emissions of internal combustion engines. By modifying the valves lift profiles, they permit to control the engine breathing in order to optimize the cylinder filling. This optimization is designed for steady-state conditions. Because of the difference of response times of the subsystems involved in the cylinder filling process (intake manifold quantities and VVA actuators), the transients may be impaired. In this work, a cylinder filling control strategy is presented, based on the coordination of the low-level subsystems. In this proposed strategy, the VVA devices is used in a very active way, enjoying their privileged position at the vicinity of the cylinder. It is however important to notice that the strategy is only apparent during transients and does not have any effect on the optimized (in terms of consumption and pollutant emissions) steady-state operating points.

5.1 Main contributions

In this manuscript, several contributions has been developed. They are now shortly recalled.

i) Cylinder filling model for VVA equipped engines (Chapter 2). A mean-value model of the cylinder filling process in engines equipped with VVA devices has been proposed. From thermodynamics laws, engine geometrical data and valves lifts profiles, this analytic model estimates the masses of gas entering into the cylinder. Two cases of study have been analyzed: a double VVT on a SI engine and a second exhaust valve re-opening capability on a CI engine. Experimental results have shown a good representativeness of the model compared to test bench data.

ii) Cylinder filling control of VVT SI engines (Chapter 3). A control strategy has been presented to enhance transient behavior of VVT turbocharged SI engines. The strategy is based on the coordination of the two subsystems that drive the cylinder filling, i.e. the intake manifold pressure and the VVT actuators. For that, the developed analytic cylinder filling model has been used to control both the aspirated air mass (image of the torque), and the mass of gas coming from the internal gas recirculation (additional control objective representing either the cylinder burned gas mass or the scavenged fresh air mass, depending on the operating area). The same control strategy operates under both atmospheric and turbocharging conditions, even though the fast and slow variables of the system are not the same in these two operating areas. Extensive experimental results have stressed the relevance of the control strategy under both atmospheric and turbocharging conditions. The strategy succeeds in improving transient responses. Under atmospheric conditions, the aspirated air mass is accelerated and the burned gas mass is managed. Under turbocharging conditions, accelerating the scavenging process permits to improve torque response time by 20%.

iii) Cylinder filling control of VLD Diesel engines (Chapter 4). A control strategy has been presented to enhance the transient behavior of Diesel engines equipped with a second exhaust valve lift capability. Again, the strategy is based on the coordination of the two subsystems driving the cylinder filling, i.e. the intake manifold BGR and the VLD actuator. Thanks to the cylinder filling model, the control strategy permits to guarantee an accurate control of the in-cylinder BGR, using the VLD actuator to compensate the sluggishness of the external EGR circuit. Extensive experimental results have stressed the relevance of the control strategy. The strategy succeeds in improving transient responses. As a result, NO_x emissions are largely reduced during transients.

iv) Intake manifold pressure and AFR controllers of SI engines (Appendix A, B and C). In addition to the above-presented high-level controller, some low-level controllers have been proposed too. First, as the intake manifold pressure is the most important variable for aspirated air mass control in SI engines, it is necessary to provide an accurate control. A trajectory-tracking based controller have been designed in this thesis. Experimental results have stressed the efficiency of such a controller. Second, because of emissions standards, the AFR has to be accurately kept to the stoichiometric value. In this thesis, an original method of controlling the AFR has been proposed, simplifying the usual control scheme. Experimental results have stressed the efficiency of such a controller. It is important to notice that these low-level controllers have been used and participate to the good results in the experiments relating to Chapter 3.

5.2 Perspectives

To conclude this thesis, several possible future directions in the field of engine control are sketched, which could benefit from the proposed work.

The proposed cylinder filling model developed in this thesis has been tested for two particular applications (VVT SI engine and VLD CI engine). Thanks to its physics-based design, this model is expected to be relevant for other type of application (e.g. in camless engines). Further, even if the model is not used for control purposes, it is nevertheless of interest to have an efficient estimation of the aspirated air mass in view of accurately controlling the AFR in SI applications.

The proposed control strategy permits to manage the cylinder filling quantities. It could be used in unusual working conditions. For example, for the VVT SI case study, instead of using specific VVT actuators positions look-up tables for cold start (which requires extensive calibration tests), one can simply act on the burned gas mass set point (by weighting it with the cool temperature for example to ease the start of the engine). A similar approach could be considered for the VLD CI engine too. Modifying the trade off between the exhaust EGR and IEGR would permit to accelerate the catalyst light-off during cold starts (instead of using specific VLD actuator position look-up tables for cold start).

Some other VVA equipped engine applications can take advantage of the proposed strategy. The first example is EGR equipped VVT SI engines. In this application, on top of coordinating the intake pressure with the VVT actuators, one has to add the EGR in the coordination to obtain the correct cylinder filling during transients. A second example is turbocharged camless engines. In this application, the intake pressure is always slow (no throttle) and the valve actuation is very fast because it consists in electromagnetic actuators. Then compensation of the pressure sluggishness can be considered to realize the torque demand. Moreover, one can use the fact that the valve actuation in camless engine has a very larger range then VVT actuators, and then can bring more benefits during transients. Finally, one can consider also VVT CAI engines. Here, the objective is to control the in-cylinder temperature to control the combustion. It is then important to coordinate the exhaust EGR and the VVA actuator in order to avoid misfires. Further studies are necessary to treat this case, but, certainly, the same methodology can be exploited.

Finally, other applications can take advantage of the proposed strategy, even if the engine under consideration is not equipped with any VVA capability. More and more engine applications are composed of subsystems with various response times. Some particular examples are Diesel engines equipped with both high and low pressure EGR loops or hybrid vehicles where the two torque sources (electric and thermal) have not the same response time. These are perspective to explore in the future.

Appendix A

Intake manifold pressure controller for SI engines

A.1 Introduction

Chapter 3 has shown that coordinating the low-level controllers (intake manifold pressure and VVT actuators positions) permit to reach better performances in SI engines. Coordination strategy is based on the fact that low-level subsystems have different time scales. On the one hand, during turbocharged conditions, VVT actuators positions subsystem is much faster than the intake manifold subsystem because of the turbocharger inertia. On the other hand, VVT actuators positions subsystem is quite slow compared to the intake manifold subsystem during atmospheric conditions. It is however only the case if there is an efficient intake manifold pressure controller. Some controllers have been proposed in the literature. In [33], a state feedback control based on a linearized model is presented. The system nonlinearities have been accounted for in [35] and [14]. In the first, a fuzzy control strategy is presented. In the second, an internal model control strategy based on static model inversion is proposed.

In this chapter, an intake manifold pressure controller is proposed using the throttle actuator and considering the VVT actuators as measured disturbances. The intake dynamics is modeled as a first order system, using the breathing model of Chapter 2 related to the VVT actuators, and one bias that stands for errors in experimentally determined look-up table of the throttle actuator is considered. Provided that this bias is known, a one-dimensional actuated dynamics is obtained, for which the motion planning and trajectory-tracking problems are already solved. From a more realistic standpoint, a compensation of this bias can be obtained by use of an integral term. Experimental results prove the relevance of this approach.

A.2 System modeling

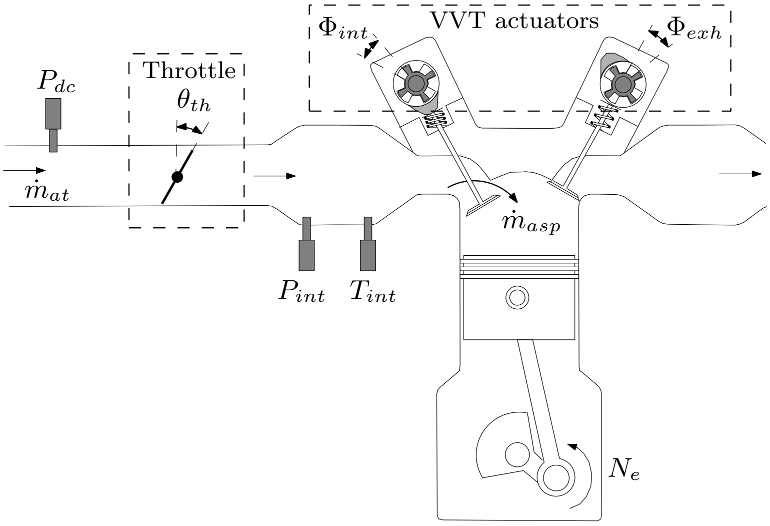

Figure A.1: $\dot{m}_{at}$ and $\dot{m}_{asp}$ are the non-measured inlet and aspirated air mass flows respectively. Downstream compressor pressure, P_{dc}, intake manifold pressure and temperature, P_{int} and T_{int}, and engine speed, N_e, are measured by sensors. θ_{th}, Φ_{int} and Φ_{exh} are the actuators angle positions.

A.2.1 Balance in the intake manifold

Consider the air path of an SI engine equipped with VVT actuators as depicted in Figure A.1. In this configuration, i.e. with internal exhaust gas recirculation, the air path has a very simple structure. It can be modeled by an intake manifold which has an inlet flow (controlled by the throttle) and an outlet flow (impacted on by the VVT actuators). The intake manifold is considered to have a constant volume, V_{int}, in which the thermodynamic state (pressure, temperature, and composition) is assumed to be spatially homogeneous. Also, time variations of the temperature are neglected in this volume (following [3] and [21]), i.e. $\dot{T}_{int} = 0$. Under these assumptions, a mass balance in the intake manifold gives

$$\dot{P}_{int} = \alpha_{int}(\dot{m}_{at} - \dot{m}_{asp}) \tag{A.1}$$

where $\alpha_{int} \triangleq RT_{int}/V_{int}$. Both P_{int} and T_{int} are measured by sensors located in the intake manifold. $\dot{m}_{at}$ is the intake mass air flow. Correspondingly, $\dot{m}_{asp}$ is the mass air flow aspirated into the cylinders.

Intake mass air flow

The intake mass air flow, $\dot{m}_{at}$, can be modeled in the form

$$\dot{m}_{at} = Area_{th} \cdot f(P_{int}) \tag{A.2}$$

where $Area_{th}$ is the effective opening area of the throttle. The mass flow rate per unit area, $f(P_{int})$, is given in [24], in the form

$$f(P_{int}) = \frac{P_{dc}}{\sqrt{RT_{int}}} \begin{cases} \left(\frac{P_{int}}{P_{dc}}\right)^{\frac{1}{\gamma}} \sqrt{\frac{2\gamma}{\gamma-1}\left(1-\left(\frac{P_{int}}{P_{dc}}\right)^{\frac{\gamma-1}{\gamma}}\right)} & \text{, if } \left(\frac{P_{int}}{P_{dc}}\right) > r_c \\ \sqrt{\gamma\left(\frac{2}{\gamma+1}\right)^{\frac{\gamma+1}{\gamma-1}}} & \text{, otherwise} \end{cases} \tag{A.3}$$

where P_{dc} is the measured downstream compressor pressure, γ is the ratio of specific heat capacities in the intake manifold and $r_c = (2/(\gamma+1))^{\gamma/(\gamma-1)}$ denotes the critical pressure ratio. The effective area of the throttle is usually modeled with a polynomial function of the angular position of the actuator, i.e. $Area_{th} = \mathcal{A}(\theta_{th})$. Figure A.2 presents the modeled and experimental opening areas of the throttle as a function of the angular position of the actuator.

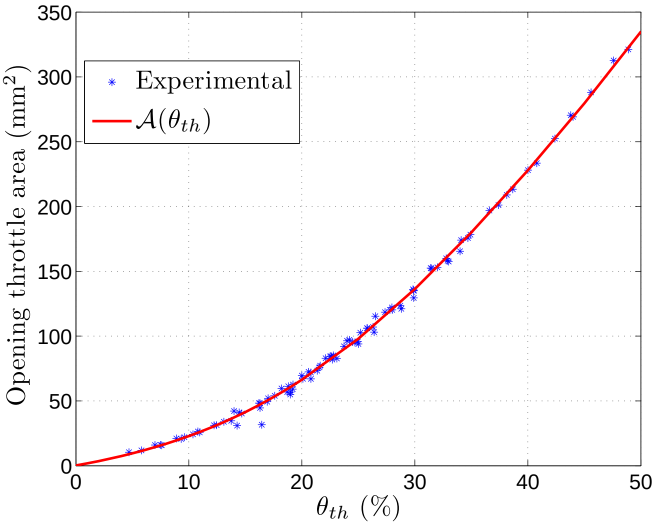

Figure A.2: Experimental comparison between the modeled and measured throttle opening area.

As the model (A.2) is not perfect, one can add a modeling error term ϵ_{th}, leading to the following relation:

$$Area_{th} f(P_{int}) = \mathcal{A}(\theta_{th}) f(P_{int}) + \epsilon_{th} \tag{A.4}$$

Aspirated mass air flow

Following [24], the mass air flow through the inlet valves can be modeled in the form

$$\dot{m}_{asp} = \eta_{vol} \beta_{int} P_{int} \tag{A.5}$$

where $\beta_{int} \triangleq (V_d/RT_{int})(N_e/120)$ and η_{vol} is the volumetric efficiency. Then, identifying (A.5) and aspirated mass model (2.18) given in Chapter 3, one can derive a model of the volumetric efficiency,

$$\eta_{vol} = \alpha_1 \frac{V_{ivc}(\Phi_{int})}{V_d} - \frac{RT_{int}}{P_{int} V_d} \left(\alpha_2 \frac{\mathrm{OF}(\Phi_{exh} - \Phi_{int})}{N_e} + \alpha_3 V_{evc}(\Phi_{exh}) \right)$$

For the rest, it is noted $\eta_\Delta(P_{int}) \triangleq \eta_{vol}$ with $\Delta \triangleq (N_e, T_{int}, \Phi_{int}, \Phi_{exh})$.

A.2.2 State space model and physical assumptions

Using the balance equation in the intake manifold (A.1) and the expressions of the intake mass flows (A.2) and (A.5), the intake manifold pressure dynamics writes

$$\dot{P}_{int} = \alpha_{int} (\mathcal{A}(\theta_{th}) f(P_{int}) + \epsilon_{th} - \eta_\Delta(P_{int}) \beta_{int} P_{int}) \tag{A.6}$$

Let $x \triangleq P_{int}$, $b \triangleq \epsilon_{th}$ and $u \triangleq \theta_{th}$ to denote the state and the control variable of the system, respectively. The measurement is $y \triangleq x$. Gathering (A.6), (A.5), and (A.4) together, one can write

$$\left\{ \begin{array}{rcl} \dot{x} & = & \alpha_{int}(\mathcal{A}(u) f(x) + b - \eta_\Delta(x) \beta_{int} x) \\ \dot{b} & = & 0 \\ y & = & x \end{array} \right. \tag{A.7}$$

By definition (A.3), $f : \mathbb{R} \to \mathbb{R}$ is a positive decreasing function. Physically, $\eta_\Delta : \mathbb{R} \to \mathbb{R}$ is a positive increasing function.

Due to physical limitations of the engine, the constants α_{int} and β_{int} are positively bounded. One note $\alpha_{int} \in [\underline{\alpha_{int}}, \overline{\alpha_{int}}] > 0$ and $\beta_{int} \in [\underline{\beta_{int}}, \overline{\beta_{int}}] > 0$. Further, the volumetric efficiency η is also positively bounded, i.e. $\eta_\Delta(x) \in [\underline{\eta}; \overline{\eta}]$. Its derivative η'_Δ is also strictly positive (one can refer to Figure 3.4) and bounded.

A.3 Reference trajectory

The pressure reference trajectory is directly given by the high-level controller through equation (3.12). Let x^r be the pressure reference trajectory reading

$$x^r = F(\Phi_{int}, \Phi_{exh}, m_{asp}^{sp}) \tag{A.8}$$

where Φ_{int} and Φ_{exh} are the measured intake and exhaust VVT actuators positions respectively. The air path has a first-order dynamics (A.7). Therefore, the intake manifold pressure trajectory must be differentiable at least once. In practice, this minimal smoothness requirement is guaranteed by a low-pass filtering of the torque set point T_q^{sp} and thus the aspirated air mass set point. Since F is a continuous function (see proposition 3.1), x^r has the same continuity and differentiability properties as m_{asp}^{sp}, Φ_{int} and Φ_{exh}.

A.4 Trajectory-tracking strategy

A.4.1 Open-loop control when the bias is known

The system (A.7) is fully actuated and invertible. Provided that the bias b is equal to zero, one can easily compute an open-loop control law for any smooth trajectory. This is, in theory, sufficient to guarantee tracking, owing to the open-loop stability of (A.7). Consider the following open-loop control law:

$$u^r = \mathcal{A}^{-1}\left(\frac{1}{f(x)}\left(\frac{\dot{x}^r}{\alpha_{int}} + \eta_\Delta(x^r)\beta_{int}x^r\right)\right) \tag{A.9}$$

Then the following proposition holds.

Proposition A.1.
Consider a perfect system (A.7) with $b = 0$ and some smooth reference trajectory x^r. The open-loop control law (A.9) guarantees that the tracking error exponentially converges towards 0 when $t \to \infty$.

Proof A.1.

After substitution in (A.7), one obtains

$$\dot{x} = \dot{x}^r + \alpha_{int}\beta_{int}(\eta_\Delta(x^r)x^r - \eta_\Delta(x)x) \tag{A.10}$$

Let $e \triangleq x - x^r$ be the error between the measurement and the reference pressure. Let $h : \mathbb{R} \to \mathbb{R}$ be the increasing continuous function on $\mathcal{I} = \left[x^{\min}; x^{\max}\right]$ defined by $h_\Delta(x) \triangleq \eta_\Delta(x)x$. From the intermediate value theorem, there exists one real c in $[\underline{x};\overline{x}] \subset \mathcal{I}$, where $\underline{x} = \min(x, x^r)$ and $\overline{x} = \max(x, x^r)$, such that

$$h_\Delta(\underline{x}) - h_\Delta(\overline{x}) = h'_\Delta(c)(\underline{x} - \overline{x}) \tag{A.11}$$

In (A.11), c depends on $x(t)$ and $x^r(t)$. More precisely, it can be represented as a time-varying function, depending on the initial condition of x that shall be denoted λ. Using (A.11) in (A.10), one obtains

$$\dot{e} = -\alpha_{int}\beta_{int}h'_\Delta(c(t,\lambda))e$$

Yet, $h'_\Delta(c(t,\lambda)) = \eta'_\Delta(c(t,\lambda))c(t,\lambda) + \eta_\Delta(c(t,\lambda)) \geq \underline{\eta}$ thanks to bounds given in § A.2.2. Finally, positiveness of the terms α_{int} and β_{int} yields the exponential convergence of e towards 0. ■

A.4.2 Closed-loop control in the case of unknown bias

In a more realistic setup, assume that the bias b is not equal to zero. To compensate for this missing information, one add an integral term to the feedback law, aimed at tracking the reference trajectory x^r. This leads us to consider the following control law:

$$u^{sp} = \mathcal{A}^{-1}\left(\mathcal{A}(u^r) - \frac{1}{\alpha_{int}f(x)}\left(k_p(x - x^r) + k_i\int_0^t (x - x^r)dt\right)\right) \tag{A.12}$$

where k_p and k_i are strictly positive constants. Tracking of the trajectory using the control law (A.12) leads to the following proposition.

Proposition A.2.
Consider system (A.7) and some smooth reference trajectory x^r. The closed-loop control law (A.12) guarantees that the tracking error exponentially converges towards 0 when $t \to \infty$.

Proof A.2.
After substitution of (A.12) in (A.7), one obtains

$$\dot{x} = \dot{x}^r - k_p(x - x^r) - k_i\int_0^t (x - x^r)dt + \alpha_{int}b + \alpha_{int}\beta_{int}(\eta_\Delta(x^r)x^r - \eta_\Delta(x)x)$$

Note $e \triangleq x - x^r$ the error between the measurement and the reference pressure, and I the integral term, i.e. $\dot{I} = -k_ie$. Using (A.11), the error dynamics can be written under the state space form

$$\left\{\begin{array}{l}\dot{e} = -(k_p + \alpha_{int}\beta_{int}h'_{\Delta}(c(t,\lambda)))e + I + \alpha_{int}b \\ \dot{I} = -k_i e\end{array}\right. \tag{A.13}$$

Consider the variable (which can be interpreted as the asymptotic value of the integrator, once convergence is proven)

$$\omega = -\alpha_{int}b \tag{A.14}$$

and note $\tilde{I} = I - \omega$. The error dynamics (A.13) takes the form of a parameterized Linear Time-Varying (LTV) multivariable system,

$$\dot{X}_c = \mathcal{A}(t,\lambda)X_c \tag{A.15}$$

with $X_c \triangleq \begin{pmatrix} e & \tilde{I}\end{pmatrix}^T$ and

$$\mathcal{A}(t,\lambda) \triangleq \begin{pmatrix} -k_p - \alpha_{int}\beta_{int}h'_{\Delta}(c(t,\lambda)) & 1 \\ -k_i & 0 \end{pmatrix}$$

In (A.15), the matrix $\mathcal{A}(t,\lambda)$ is impacted by the control gains k_p and k_i. To prove convergence of the pressure to the reference trajectory, it is shown that (A.15) is λ-Uniformly Globally Exponentially Stable (λ-UGES). For that, the following important result about stability of a class of parameterized LTV systems studied in [57] is used.

Theorem A.1 (λ-UGES of parameterized LTV systems, Loría-Panteley [57]). *Consider the parameterized LTV multivariable system (A.16) under the following form*

$$\begin{pmatrix}\dot{e} \\ \dot{\theta}\end{pmatrix} = \begin{pmatrix} A(t,\lambda) & B(t,\lambda)^T \\ -C(t,\lambda) & 0 \end{pmatrix}\begin{pmatrix} e \\ \theta\end{pmatrix} \tag{A.16}$$

where $e \in \mathbb{R}^n$, $\theta \in \mathbb{R}^m$, $A(t,\lambda) \in \mathbb{R}^{n\times n}$, $B(t,\lambda) \in \mathbb{R}^{m\times n}$, $C(t,\lambda) \in \mathbb{R}^{m\times n}$, $\lambda \in \mathcal{D} \subset \mathbb{R}^l$, *and* n, m, l *are some integers. Assume that the following two properties hold.*

Assumption A.1.
There exists $\phi_M > 0$ *such that for all* $t \geq 0$ *and for all* $\lambda \in \mathcal{D}$, $\max\left\{\|B(t,\lambda)\|, \left\|\frac{\partial B(t,\lambda)}{\partial t}\right\|\right\} \leq \phi_M$.

Assumption A.2.
There exist symmetric matrices $P(t,\lambda)$ *and* $Q(t,\lambda)$ *such that*

$$\begin{cases} C(t,\lambda)^T & = P(t,\lambda)B(t,\lambda)^T \\ -Q(t,\lambda) & = A(t,\lambda)^T P(t,\lambda) + P(t,\lambda)A(t,\lambda) + \dot{P}(t,\lambda) \end{cases}$$

There exists p_m*,* q_m*,* p_M *and* $q_M > 0$ *such that, for all* $(t,\lambda) \in \mathbb{R}_{\geq 0} \times \mathcal{D}$*,* $p_m I \leq P(t,\lambda) \leq p_M I$ *and* $q_m I \leq Q(t,\lambda) \leq q_M I$*.*

Then, the system is λ*-UGES if and only if* $B(t,\lambda)$ *is* λ*-uniform persistency of excitation, i.e. there exists* μ*,* $T > 0$ *such that* $\int_t^{t+T} B(\tau,\lambda)B(\tau,\lambda)^T d\tau \geq \mu I \quad \forall t$*.*

Consider system (A.15) with $\mathcal{D} = \mathbb{R}$, $n = 1$, $m = 1$. One has $A(t,\lambda) = -k_p - \alpha_{int}\beta_{int}h'_\Phi(c(t,\lambda))$, $B(t,\lambda) = 1$ and $C(t,\lambda) = k_i$. Then, Assumption A.1 is easily enforced with $\phi_M = 1$.

Moreover, let $P(t,\lambda) = k_i$ and $Q(t,\lambda) = 2k_i(k_p + \alpha_{int}\beta_{int}h'_\Phi(c(t,\lambda)))$ with k_p, k_i, α_{int}, $\beta_{int} > 0$. By noticing that $h'_\Phi(c(t,\lambda))$ is bounded, it follows that Assumption A.2 is also verified. Finally, the λ-uniform persistency of excitation is readily proven with $\mu = T = 1$.

It can be concluded that the parameterized LTV multivariable system (A.15) is λ-UGES. ■

A.5 Experimental tip-in on test bench

A.5.1 Implementation

The global control scheme is summarized in Figure A.3. The air path controller uses the motion-planning control strategy presented in Section A.4. The reference trajectory of the pressure P^r_{int}, computed in the coordination block, is used in a dynamic model inversion to determine the feedforward control law θ^r_{th} described in Section A.4.1. Finally, a PI controller is added to the structure to provide further accuracy and robustness. Its implementation is given in Section A.4.2 and computes the throttle-opening set point θ^{sp}_{th}.

A.5.2 Torque transients at test bench

The control strategy presented in this section was tested on an experimental test bench. The engine in consideration is a 1.8L SI engine equipped with dual independent VVT actuators. Figure A.4 and Figure A.5 represent two torque trajectories at 2000 rpm and 1500 rpm respectively. In both cases, the three top figures give the set points

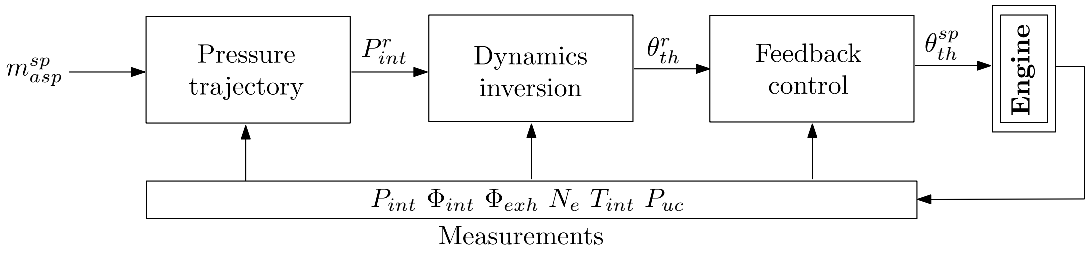

Figure A.3: Intake manifold pressure control scheme based on a trajectory-tracking strategy.

and measurements (or estimation in the case of the aspirated air mass) of the aspirated air mass, the intake manifold pressure and the throttle actuator position. The two bottom figures give more detail on a particular transient to highlight the contribution of the proposed strategy.

At first view, looking at Figure A.4(b) and Figure A.5(b), the tracking of the pressure trajectory is good. It implies a good aspirated air mass tracking (Figure A.4(a) and Figure A.5(a)) that is beneficial in terms of torque production and air/fuel ratio control (see Appendix C). This tracking is ensured by the accurate control of the throttle presented in Figure A.4(c) and Figure A.5(c). The large peaks in the actuator trajectories follows from the slow dynamics of the downstream compressor pressure that establishes with a large response time.

If one zooms in on a large transient, the beneficial impact of the proposed control strategy is seen in the intake manifold pressure response on Figure A.4(d) and Figure A.5(d). Indeed, looking at Figure A.4(e) and Figure A.5(e), it can be seen that the feedforward term θ_{th}^{r} using the derivative of the pressure trajectory $\dot{P}_{int}^{r}$ (see (A.9)) boosts the throttle position set point thanks to the small overshoot observed at time 13.2 s and 41.2 s respectively. The integral term in the feedback strategy (A.12) permits to remove the pressure tracking error.

A.5.3 Torque transient on vehicle

The control strategy presented in this section was also tested on a vehicle. The engine in consideration uses the same engine as depicted before. Figure A.6 give some results during the vehicle take off. Figure A.6(a) represents the aspirated air mass set point and its estimation, Figure A.6(b) gives the intake and exhaust VVT actuators positions set points and measurements to stress that they are moving during the transient. Finally, Figure A.6(c) and Figure A.6(d) represent the intake manifold pressure and throttle trajectories. It can be seen that the intake manifold pressure trajectory

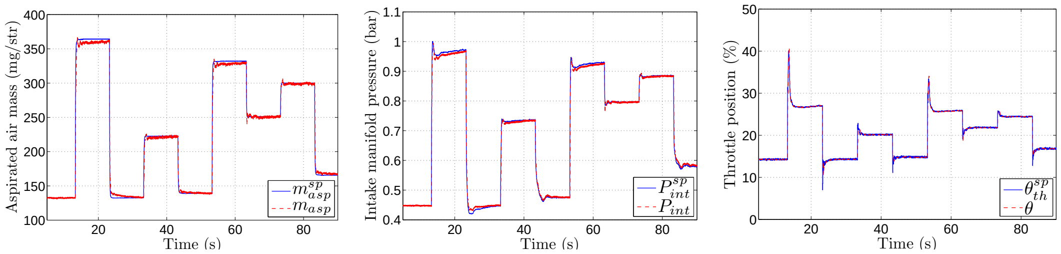

(a) Aspirated air mass (b) Intake manifold pressure (c) Throttle position

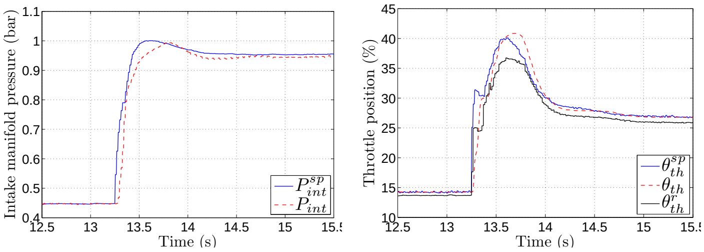

(d) Intake manifold pressure (e) Throttle position

Figure A.4: Experimental results for a four-cylinder SI engine at constant engine speed (2000 rpm). Torque trajectory (Nm): $30 - 120 - 30 - 70 - 40 - 110 - 80 - 100 - 50$.

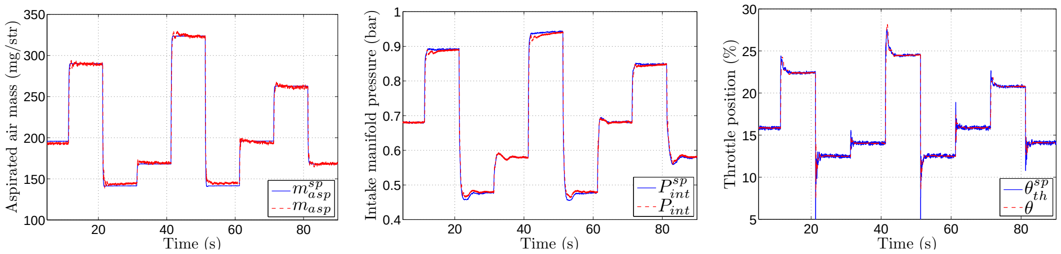

(a) Aspirated air mass (b) Intake manifold pressure (c) Throttle position

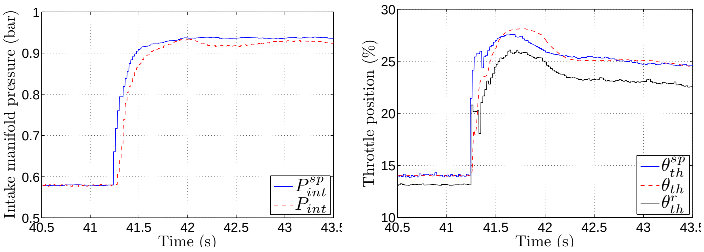

(d) Intake manifold pressure (e) Throttle position

Figure A.5: Experimental results for a four-cylinder SI engine at constant engine speed (1500 rpm). Torque trajectory (Nm): $60 - 100 - 40 - 50 - 110 - 40 - 60 - 90 - 50$.

tracking is very efficient thanks to the throttle control strategy. The VVT actuators, seen as measured disturbances in the control strategy, do not impact on the aspirated air mass tracking. In addition, like during torque transients at test bench, the feedforward control law boosts the pressure response during the transient at about 3.4 s.

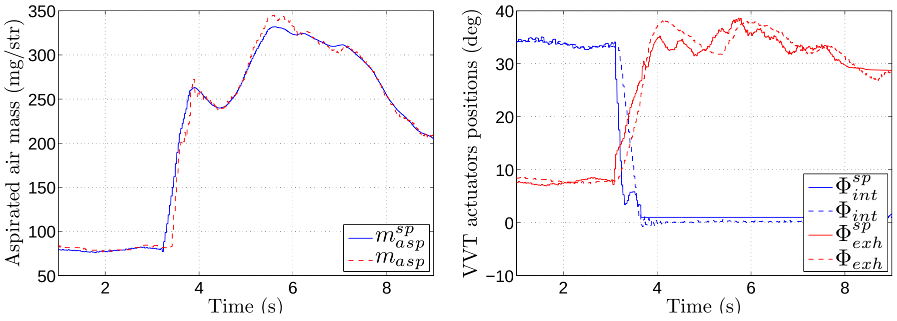

(a) Aspirated air mass (b) VVT actuators positions

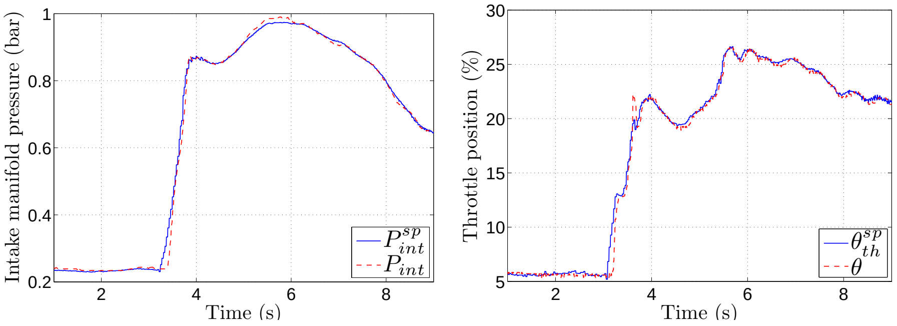

(c) Intake manifold pressure (d) Throttle position

Figure A.6: Experimental results for a four-cylinder SI engine on vehicle during take off.

A.6 Conclusion

An intake manifold pressure controller based on a trajectory-tracking strategy has been presented. The pressure trajectory is defined in the high-level controller presented in Chapter 3. Using a simple mass balance model in the intake manifold, a feedforward throttle control law can be computed. Then, in order to account for modeling errors, a feedback loop using intake manifold pressure measurement is considered. Convergence of the pressure towards its reference trajectory is analyzed using an important theoretical result about time-varying systems. Finally, experimental results obtained at test bench show the good results obtained by the proposed strategy.

Appendix B

Usage of a mass air flow sensor

B.1 Introduction

In some applications, a Mass Air Flow (MAF) sensor can be added at the intake of the engine as pictured on Figure B.1. Despite the additional cost, it permits to increase robustness of the aspirated mass estimation. Indeed, breathing model errors can be compensated using such a measurement as proposed in [3, 20, 78]. In this appendix, it is proposed to account for this additional measurement in the aspirated air mass control. The control strategy presented in Appendix A is slightly modified by adding a bias term into the volumetric efficiency law. This term is estimated by a nonlinear observer and prove convergence of the designed observer-controller.

B.2 System modeling

B.2.1 Balance in the intake manifold

Let us consider the same first order dynamics model than in Appendix A. Thanks to the presence of the mass air flow sensor, the throttle air mass flow $\dot{m}_{at}$ is approximated as the mass air flow measurement, $\dot{m}_{MAF}$. Moreover, considering breathing model uncertainties (see Figure 2.9), one can add a bias $\delta\eta$ to compensate for modeling errors (as well as for varying exhaust pressure conditions) in the aspirated air mass flow equation (A.5),

$$\dot{m}_{asp} = (\eta_{\Delta}(P_{int}) + \delta\eta)\beta_{int}P_{int} \tag{B.1}$$

The bias $\delta\eta$ is completely unknown when it represents the modeling error in the volumetric efficiency. Following ideas of [3] and [78], one assume a constant bias, i.e. $\dot{\delta\eta} = 0$.

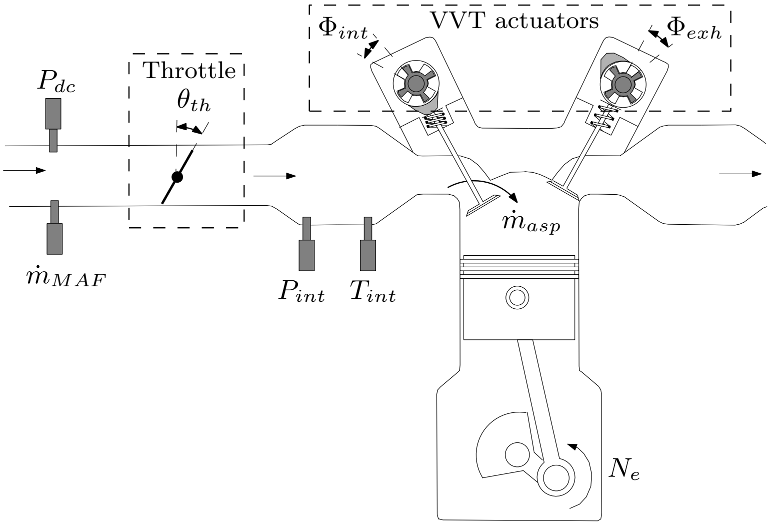

Figure B.1: $\dot{m}_{asp}$ is the non-measured aspirated air mass flow. Intake mass air flow, $\dot{m}_{MAF}$, downstream compressor pressure, P_{dc}, intake manifold pressure and temperature, P_{int} and T_{int}, and engine speed, N_e, are measured by sensors. θ_{th}, Φ_{int} and Φ_{exh} are the actuators angle positions.

B.2.2 State space model and physical assumptions

One use $x \triangleq P_{int}$, $b \triangleq [\epsilon_{th} \;\; \delta\eta]^T$ and $u \triangleq \theta_{th}$ to denote the state and the control variable of the system, respectively. The measurements are $y_1 \triangleq x$ and $y_2 \triangleq \dot{m}_{MAF}$. Using (B.1) into (A.7), the state space model reads

$$\left\{ \begin{array}{lcl} \dot{x} & = & \alpha_{int}(\mathcal{A}(u)f(x) + b_1 - (\eta_\Delta(x) + b_2)\beta_{int}x) \\ \dot{b}_1 & = & 0 \\ \dot{b}_2 & = & 0 \\ y_1 & = & x \\ y_2 & = & \mathcal{A}(u)f(x) + b_1 \end{array} \right. \tag{B.2}$$

In addition to assumptions given in Section A.2.2, the volumetric efficiency η is bounded, i.e. $(\eta_\Delta(x) + b_2) \in \left[\underline{\eta}; \overline{\eta}\right]$. Its derivative η'_Δ is also positive and bounded.

B.3 Reference trajectory

The mass air flow sensor can be used as a feedback information for the aspirated air mass control. Instead of computing the aspirated air mass set point with the breathing model (see (3.11)), one can directly derive an aspirated air mass look-up table using the torque and the engine speed as inputs and the MAF information as output, i.e.

$m_{asp}^{sp} = \text{map}(T_q^{sp}, N_e)$. Now, if one notes $m_{asp} = f_{\delta_\eta}(P_{int}, \Phi_{int}, \Phi_{exh})$ as the perfect model for the aspirated air mass, then one can easily see that the intake pressure trajectory computed by the coordination strategy (3.12) will lead to a static error

$$m_{asp} = f_{\delta_\eta}(F(\Phi_{int}, \Phi_{exh}, m_{asp}^{sp}), \Phi_{int}, \Phi_{exh}) \neq m_{asp}^{sp}$$

where F corresponds to the invert function of f (corresponding to $\delta\eta = 0$). In order to compensate for this steady-state error, the modeling error in the computation of the intake manifold pressure trajectory has to be taken into account,

$$x^{sp} = F_{b_2}(\Phi_{int}, \Phi_{exh}, m_{asp}^{sp}) \tag{B.3}$$

In this way, one can ensure the following equality during steady-state conditions

$$m_{asp} = f_{b_2}(F_{b_2}(\Phi_{int}, \Phi_{exh}, m_{asp}^{sp}), \Phi_{int}, \Phi_{exh}) = m_{asp}^{sp}$$

The bias b_2 is unknown, and the trajectory x^{sp} cannot be explicitly computed. To compensate for this lack of information, an observer is needed to reconstruct b_2 in order to be able to compute the pressure reference trajectory reading

$$x^r = F_{\hat{b}_2}(\Phi_{int}, \Phi_{exh}, m_{asp}^{sp}) \tag{B.4}$$

In the following, it is assumed that, as a consequence of the discussed properties of the reference trajectories derivation, x^r is smooth and bounded and that $\dot{x}^r$ is bounded. The mentioned observer is presented in the next section.

B.4 Trajectory-tracking strategy

B.4.1 Observer design

To compensate for the missing information, an observer is used to provide an estimate of b_2. A nonlinear observer based on pressure measurement can be considered in the form

$$\left\{ \begin{array}{rcl} \dot{\hat{x}} & = & \alpha_{int}(y_2 - (\eta_\Delta(x) + \hat{b}_2)\beta_{int}\hat{x}) + L_1(x - \hat{x}) \\ \dot{\hat{b}}_2 & = & -L_2(x - \hat{x}) \end{array} \right. \tag{B.5}$$

where $(L_1, L_2) \in (\mathbb{R}^+ \setminus \{0\})^2$. Let $\tilde{x} \triangleq x - \hat{x}$ and $\tilde{b}_2 \triangleq b_2 - \hat{b}_2$ be the state errors. Then, error system writes

$$\left\{ \begin{array}{rcl} \dot{\tilde{x}} & = & -\alpha_{int}\beta_{int}((\eta_\Delta(x) + b_2)\tilde{x} + \hat{x}\tilde{b}_2) - L_1\tilde{x} \\ \dot{\tilde{b}}_2 & = & L_2\tilde{x} \end{array} \right. \tag{B.6}$$

There, importance of using the air mass flow measurement y_2 instead of the throttle flow $\mathcal{A}(u)f(x)$ in the observer structure can be seen. Thanks to this arbitrary choice in the observer design, the y_2 term is canceled out in the error system (B.6) and the control variable u does not appear anymore. Observer design and controller design can be treated separately. Gains are chosen as follows

$$L_1 = \alpha_{int}\beta_{int} l_1 \quad \text{and} \quad L_2 = \alpha_{int}\beta_{int}\hat{x} l_2$$

where l_1 and l_2 are positive constants. With this choice, the error system writes

$$\left\{ \begin{array}{rcl} \dot{\tilde{x}} & = & -\alpha_{int}\beta_{int}(\eta_\Delta(x) + b_2 + l_1)\tilde{x} - \alpha_{int}\beta_{int}\hat{x}\tilde{b}_2 \\ \dot{\tilde{b}}_2 & = & \alpha_{int}\beta_{int}\hat{x} l_2 \tilde{x} \end{array} \right. \tag{B.7}$$

One can not prove the observer convergence before presenting the intake manifold pressure control law. However, for the moment, one can bound the observer errors $\tilde{x}$ and $\tilde{b}_2$. Consider

$$V(\tilde{x}, \tilde{b}_2) \triangleq \frac{1}{2}\|\tilde{x}\|^2 + \frac{1}{2l_2}\left\|\tilde{b}_2\right\|^2 \tag{B.8}$$

Differentiation with respect to time leads to

$$\begin{array}{rcl} \dot{V}(\tilde{x}, \tilde{b}_2) & = & \tilde{x}\dot{\tilde{x}} + \frac{1}{l_2}\tilde{b}_2\dot{\tilde{b}}_2 \\ & = & -\alpha_{int}\beta_{int}(\eta_\Delta(x) + b_2 + l_1)\tilde{x}^2 \leq 0 \end{array}$$

Semi-negativeness of this last expression is directly obtained from assumptions given in Section A.2.2 and Section B.2.2, together with $l_1 > 0$. Since V is decreasing, then $\tilde{x}$ and $\tilde{b}_2$ are bounded. One notes

$$\|\tilde{x}\|_\infty < \infty \text{ and } \left\|\tilde{b}_2\right\|_\infty < \infty \tag{B.9}$$

B.4.2 Closed loop control law

The same control law as in Section A.4.2 is designed, except that the missing information b_2 has to be compensated for. The closed-loop control law is given by

$$u^{sp} \quad = \quad \mathcal{A}^{-1}\left(\mathcal{A}(u^r) - \tfrac{1}{\alpha_{int} f(x)}\left(k_p(x-x^r) + k_i \int_0^t (x-x^r)dt\right)\right) \tag{B.10}$$

where the open-loop control law writes

$$u^r = \mathcal{A}^{-1}\left(\frac{1}{f(x)}\left(\frac{\dot{x}^r}{\alpha_{int}} + (\eta_\Delta(x^r) + \hat{b}_2)\beta_{int} x^r\right)\right) \tag{B.11}$$

In the next section, the stability of the observer-controller (B.5)-(B.10) is analyzed.

B.4.3 Convergence proof of the observer-controller

After substitution of (B.10) in (B.2), one obtains

$$\begin{aligned}\dot{x} \quad &= \quad \dot{x}^r - k_p(x-x^r) - k_i \int_0^t (x-x^r)dt + \alpha_{int} b_1 \\ &\quad\quad +\alpha_{int}\beta_{int}((\eta_\Delta(x^r) + \hat{b}_2)x^r - (\eta_\Delta(x) + b_2)x)\end{aligned}$$

Note $e \triangleq x - x^r$ the error between the measurement and the reference pressure, and I the integral term, i.e. $\dot{I} = -k_i e$. Using (A.11), the error dynamics can be written under the state space form

$$\begin{cases} \dot{e} = -(k_p + \alpha_{int}\beta_{int}(h'_\Delta(c(t,\lambda)) + b_2))e + I - \alpha_{int}(\beta_{int} x^r \tilde{b}_2 - b_1) \\ \dot{I} = -k_i e \end{cases} \tag{B.12}$$

Consider the variable (which can be interpreted as the asymptotic value of the integrator, once convergence is proven)

$$\omega = \alpha_{int}(\beta_{int} x^r \tilde{b}_2 - b_1) \tag{B.13}$$

and note $\tilde{I} = I - \omega$. The error dynamics (B.12) takes the form of a forced parameterized Linear Time-Varying (LTV) multivariable system,

$$\dot{X}_c = \mathcal{A}(t,\lambda)X_c + v(t) \tag{B.14}$$

with $X_c \triangleq \left(e \ \tilde{I}\right)^T$, $v(t) \triangleq (0 \ \dot{\omega})^T$ and

$$\mathcal{A}(t,\lambda) \triangleq \begin{pmatrix} -k_p - \alpha_{int}\beta_{int}(h'_{\Delta}(c(t,\lambda)) + b_2) & 1 \\ -k_i & 0 \end{pmatrix}$$

In (B.14), the matrix $\mathcal{A}(t,\lambda)$ is impacted by the control gains k_p and k_i, while the forcing term $v(t)$ is due to observation error. To prove convergence of the pressure to the reference trajectory (which is the main objective), it is shown that (B.14) is λ-Uniformly Globally Asymptotically Stable (λ-UGAS). First, the parameterized LTV multivariable unforced system is analyzed

$$\dot{X}_c = \mathcal{A}(t,\lambda)X_c \tag{B.15}$$

The use of Theorem A.1 easily permits to show the following proposition.

Proposition B.1.

The unforced system (B.15) is Uniformly Globally Exponentially Stable (λ-UGES).

For the forced system (B.14), some decay property of the forcing term $v(t)$ permits to show the following proposition.

Proposition B.2.

The forced system (A.15) is λ-Uniformly Globally Asymptotically Stable (λ-UGAS). The tracking error asymptotically converges towards 0 when $t \to \infty$.

Proof B.1.

Consider the forced system (A.15). The analytic solution of the differential equation is

$$X_c(t) = \phi(t,0,\lambda)X_c(0) + \int_0^t \phi(t,\tau,\lambda)v(\tau)d\tau$$

where ϕ is the transition matrix of the system. Since system (B.15) is λ-UGES (proposition B.1), there exists $k,\gamma > 0$, independent of λ, such that $\forall t,\tau > 0$, $\|\phi(t,\tau,\lambda)\| \leq ke^{-\gamma(t-\tau)}$. Then, a bound on $X_c(t)$ can be easily obtained by

$$\begin{aligned} \|X_c(t)\| &\leq ke^{-\gamma t}\|X_c(0)\| + \textstyle\int_0^t ke^{-\gamma(t-\tau)}\|v(\tau)\| d\tau \\ &\leq ke^{-\gamma t}\|X_c(0)\| + \mathcal{I}_1(t_1,t) + \mathcal{I}_2(t_1,t) \end{aligned}$$

where $\mathcal{I}_1(t_1,t) = k\int_0^{t_1} e^{-\gamma(t-\tau)}\left\|v(\tau)\right\|d\tau$ and $\mathcal{I}_2(t_1,t) = k\int_{t_1}^{t} e^{-\gamma(t-\tau)}\left\|v(\tau)\right\|d\tau$ and $0 \leq t_1 \leq t$. One can separately evaluate the two quantities $\mathcal{I}_1$ and $\mathcal{I}_2$.

$$\begin{array}{rcl}
\mathcal{I}_1(t_1,t) & = & k\int_0^{t_1} e^{-\gamma(t-t_1)}e^{-\gamma(t_1-\tau)}\left\|v(\tau)\right\|d\tau \\
 & \leq & \frac{k}{\gamma}e^{-\gamma(t-t_1)}\left\|v\right\|_\infty(1-e^{-\gamma t_1}) \\
\mathcal{I}_2(t_1,t) & = & k\int_{t_1}^{t} e^{-\gamma(t-\tau)}\left\|v(\tau)\right\|d\tau \\
 & \leq & k\sup_{\tau\in[t_1;+\infty[}\left\|v(\tau)\right\|\int_{t_1}^{t} e^{-\gamma(t-\tau)}d\tau \\
 & \leq & \frac{k}{\gamma}\sup_{\tau\in[t_1;+\infty[}\left\|v(\tau)\right\|
\end{array}$$

To obtain a bound on X_c, one uses $t_1 = \frac{t}{2}$ and derive

$$\left\|X_c(t)\right\| \leq ke^{-\gamma t}\left\|X_c(0)\right\| + \frac{k}{\gamma}\left\|v\right\|_\infty(e^{-\gamma\frac{t}{2}} - e^{-\gamma t}) + \frac{k}{\gamma}\sup_{\tau\in[\frac{t}{2};+\infty[}\left\|v(\tau)\right\| \tag{B.16}$$

Thanks to this inequality, convergence of $X_c(t)$ towards 0 can be guaranteed, provided the following two conditions hold

$$\left\{\begin{array}{rcll}
\left\|v\right\|_\infty & < & \infty & \text{(a)} \\
\lim_{t\to\infty}\sup_{\tau\in[\frac{t}{2};+\infty[}\left\|v(\tau)\right\| & = & 0 & \text{(b)}
\end{array}\right.$$

Is is now proved that this is indeed the case. The norm of the forcing term can be computed from (B.13),

$$\left\|v(t)\right\| = \left\|\dot{\omega}(t)\right\| = \alpha_{int}\beta_{int}\left\|\dot{x}^r(t)\tilde{b}_2(t) + x^r(t)\dot{\tilde{b}}_2(t)\right\| \tag{B.17}$$

From the observer dynamics (B.7), one has $\dot{\tilde{b}}_2(t) = \alpha_{int}\beta_{int}\hat{x}(t)l_2\tilde{x}(t)$. In addition, note $\hat{x}(t) \triangleq x(t) - \tilde{x}(t)$, then

$$\begin{array}{rcl}
\left\|v(t)\right\| & = & \alpha_{int}\beta_{int}\left\|\dot{x}^r\tilde{b}_2 + \alpha_{int}\beta_{int}l_2x^rx\tilde{x} - \alpha_{int}\beta_{int}l_2x^r\tilde{x}^2\right\| \\
 & \leq & q(t) + l_2r(t) + l_2s(t)\left\|x\right\|
\end{array} \tag{B.18}$$

with $q(t) \triangleq \alpha_{int}\beta_{int}\left\|\dot{x}^r\right\|\left\|\tilde{b}_2\right\|$, $r(t) \triangleq \alpha_{int}^2\beta_{int}^2\left\|x^r\right\|\left\|\tilde{x}\right\|^2$ and $s(t) \triangleq \alpha_{int}^2\beta_{int}^2\left\|x^r\right\|\left\|\tilde{x}\right\|$. Yet, $\tilde{b}_2$ and $\tilde{x}$ are bounded, as is known from (B.9) and, by assumption, x^r and $\dot{x}^r$ are also bounded. It can easily be deduced that $q(t)$, $r(t)$ and $s(t)$ are also bounded, $\left\|q\right\|_\infty < \infty$, $\left\|r\right\|_\infty < \infty$ and $\left\|s\right\|_\infty < \infty$. Further, to guarantee that (a) holds, it is proved that x is also bounded. Conservatively, (B.16) yields

$$\left\|X_c(t)\right\| \leq ke^{-\gamma t}\left\|X_c(0)\right\| + \frac{k}{\gamma}(1 + e^{-\gamma\frac{t}{2}} - e^{-\gamma t})\left\|v\right\|_\infty$$

Using (B.18) one obtains

$$\begin{aligned}&\|X_c(t)\|\\&\qquad\leq ke^{-\gamma t}\|X_c(0)\|+\frac{k}{\gamma}(1+e^{-\gamma\frac{t}{2}}-e^{-\gamma t})(\|q\|_\infty+l_2\|r\|_\infty+l_2\|s\|_\infty\|x\|_\infty)\end{aligned} \tag{B.19}$$

Yet, $\|x\|=\|x^r+e\|\leq\|x^r\|+\|e\|\leq\|x^r\|+\|X_c\|$ and then, simply,

$$\|x\|_\infty\leq\|x^r\|_\infty+\|X_c\|_\infty \tag{B.20}$$

From (B.20), inequality (B.19) leads to

$$\|X_c\|_\infty \quad\leq\quad k\|X_c(0)\|+\tfrac{2k}{\gamma}(\|q\|_\infty+l_2\|r\|_\infty+l_2\|s\|_\infty\|X_c\|_\infty+l_2\|s\|_\infty\|x^r\|_\infty)$$

and, finally, to

$$\|X_c\|_\infty\left(1-l_2\tfrac{2k}{\gamma}\|s\|_\infty\right)\leq k\|X_c(0)\|+\tfrac{2k}{\gamma}(\|q\|_\infty+l_2\|r\|_\infty+l_2\|s\|_\infty\|x^r\|_\infty) \tag{B.21}$$

Bounds on $\|\tilde{x}\|_\infty$ and $\left\|\tilde{b}_2\right\|_\infty$ can be obtained from the definition of the candidate Lyapunov function (B.8) and its decreasingness. In facts, one easily derives

$$\begin{aligned}\|\tilde{x}\|_\infty &\leq \sqrt{\|\tilde{x}(0)\|^2+\tfrac{1}{l_2}\left\|\tilde{b}_2(0)\right\|^2}\\ \text{and}\quad \left\|\tilde{b}_2\right\|_\infty &\leq \sqrt{l_2\|\tilde{x}(0)\|^2+\left\|\tilde{b}_2(0)\right\|^2}\end{aligned} \tag{B.22}$$

Let us study inequality (B.21) when l_2 tends towards 0. On the left hand-side, one has

$$\lim_{l_2\to 0} l_2\frac{2k}{\gamma}\|s\|_\infty=0$$

while, on the right hand-side,

$$\begin{aligned}&\lim_{l_2\to 0}(\|q\|_\infty+l_2\|r\|_\infty+l_2\|s\|_\infty\|x^r\|_\infty)\\&\quad=\alpha_{int}\beta_{int}\|\dot{x}^r\|_\infty\left\|\tilde{b}_2\right\|_\infty+\alpha_{int}^2\beta_{int}^2\|x^r\|_\infty\left\|\tilde{b}_2(0)\right\|_\infty^2\end{aligned}$$

Then, for l_2 small enough, one can derive another more conservative inequality

$$\tfrac{1}{2}\|X_c\|_\infty\leq k\|X_c(0)\|+\tfrac{4k}{\gamma}\left(\alpha_{int}\beta_{int}\|\dot{x}^r\|_\infty\left\|\tilde{b}_2\right\|_\infty+\alpha_{int}^2\beta_{int}^2\|x^r\|_\infty\left\|\tilde{b}_2(0)\right\|_\infty^2\right)$$

It follows that $\|X_c\|_\infty < \infty$, and, from (B.20),

$$\|x\|_\infty < \infty \tag{B.23}$$

The condition (a) is easily obtained from (B.23) and (B.18). Let us now focus on the second condition (b). Inequality (B.22) shows that both $\tilde{x}$ and $\tilde{b}_2$ are bounded (as it is already known from the function V property). Further, it can be deduced from (B.7) and (B.23) that $\dot{\tilde{x}}$ is also bounded. Then, $\tilde{x}$ is uniformly continuous. In addition, positiveness of (B.8) brings

$$\begin{array}{rcl} V(\tilde{x}(0), \tilde{b}_2(0)) & \geq & -\int_0^t \dot{V}(\tilde{x}(t), \tilde{b}_2(t))dt \\ & \geq & \int_0^t \alpha_{int}\beta_{int}(\eta_\Delta(x) + b_2 + l_1)\tilde{x}^2 dt \end{array}$$

Let $\overline{C} \triangleq \overline{\alpha_{int}}\overline{\beta_{int}}(\overline{\eta} + l_1) > 0$, then $\int_0^t \tilde{x}^2 dt \leq \frac{V(\tilde{x}(0), \tilde{b}_2(0))}{\overline{C}}$. Thus, $\tilde{x}$ is square integrable, and, from the uniform continuity of $\tilde{x}^2$ (because $\tilde{x}$ is uniformly continuous), one can deduce that $\tilde{x}^2$ tends towards 0 when $t \to \infty$,

$$\lim_{t\to\infty} \tilde{x}(t) = 0 \tag{B.24}$$

From (B.7), one deduces that

$$\lim_{t\to\infty} \dot{\tilde{b}}_2(t) = 0 \tag{B.25}$$

In addition, a further time differentiation of $\dot{\tilde{x}}$ leads to

$$\begin{array}{rcl} \ddot{\tilde{x}} & = & -\alpha_{int}\beta_{int}((\eta_\Delta(x) + b_2 + l_1)\dot{\tilde{x}} + \tilde{x}\dot{x}\eta'_\Delta(x) \\ & & +(\dot{x} - \dot{\tilde{x}})\tilde{b}_2 + (x - \tilde{x})\dot{\tilde{b}}_2) \end{array}$$

Yet, $\tilde{x}$ and $\tilde{b}_2$ are bounded, while $\eta_\Delta(x) + b_2 + l_1$, and $\eta'_\Delta(x)$ are also bounded by assumption (see Section B.2.2). Then, from (B.7), $\dot{\tilde{x}}$ is bounded. Moreover, using the expression of $\dot{\tilde{b}}_2$, considering (B.23) and recalling that $\dot{x} = \dot{x}^r + \dot{e}$, it is deduced that $\ddot{\tilde{x}}$ is bounded. As $\dot{\tilde{x}}$ is uniformly continuous and using (B.24), $\lim_{t\to\infty} \dot{\tilde{x}}(t) = 0$ is obtained from Barbalat's lemma ([34], Lemma 8.2). Finally, from (4.28),

$$\lim_{t\to\infty} \tilde{b}_2(t) = \lim_{t\to\infty} \frac{\dot{\tilde{x}} + \alpha_{int}\beta_{int}(\eta_\Delta(x) + b_2 + l_1)\tilde{x}}{\alpha_{int}\beta_{int}(x - \tilde{x})} = 0 \tag{B.26}$$

Gathering (B.25) and (B.26) and recalling that, by assumption, x^r and $\dot{x}^r$ are both bounded, then, from (B.17), the condition (b) is obtained. Finally, one can conclude with the following proposition. ■

B.4.4 Conclusion on air mass control

It has been shown that the closed-loop control law allows to address the tracking of the pressure trajectory, i.e.

$$\lim_{t\to\infty} |x^r(t) - x(t)| = 0 \tag{B.27}$$

Moreover, using (B.3) and (B.4), convergence of the bias observation error (B.26) leads to the convergence of the generated trajectory towards the expected trajectory,

$$\lim_{t\to\infty} |x^{sp}(t) - x^r(t)| = 0 \tag{B.28}$$

From (B.27) and (B.28), one can conclude on the convergence of the pressure to the expected pressure trajectory,

$$\lim_{t\to\infty} |x^{sp}(t) - x(t)| = 0 \tag{B.29}$$

Recalling that pressure and air mass in the cylinder are related by $m_{asp}^{sp} = f_{b_2}(x^{sp}, \Phi_{int}, \Phi_{exh})$ and $m_{asp} = f_{\hat{b}_2}(x, \Phi_{int}, \Phi_{exh})$, using (B.26) and (B.29), one obtains

$$\lim_{t\to\infty} \left| m_{asp}^{sp}(t) - m_{asp}(t) \right| = 0$$

Then the following proposition holds,

Proposition B.3.
The observer-controller (B.5)-(B.10) guarantees the tracking of the air mass trajectory.

B.5 Experimental tip-in on test bench

B.5.1 Implementation

The global control scheme is summarized in Figure B.2. The air path controller uses the motion-planning control strategy presented in Section B.4.2. The observer estimating the breathing modeling error feeds the intake manifold pressure trajectory and the dynamics model inversion blocks. The rest of the control strategy is consistent with the one of Appendix A.

B.5.2 Torque transients

The control strategy presented in this section was tested on an experimental test bench. The engine in consideration is a 1.8L SI engine equipped with dual independent

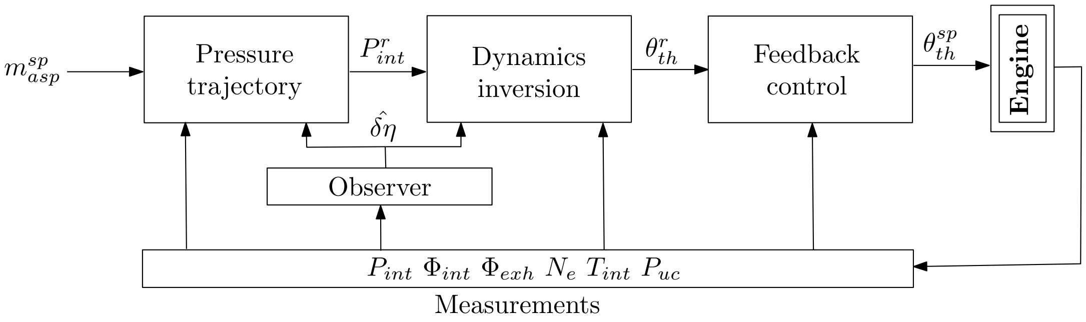

Figure B.2: The intake manifold pressure control is modified by the term $\hat{\delta\eta}$ (estimated by an observer) that permits to compensate for the breathing model uncertainties (this figure can be compared to Figure A.3).

VVT actuators. Figure B.3 and Figure B.4 represent two torque trajectories at 2000 rpm and 1500 rpm respectively. In both cases, the figures give the set point, estimation and measurement of the aspirated air mass, the set point and measurement of the intake manifold pressure.

The results follow to the same control strategy as in Appendix A, except that a feedback term given by the MAF measurement is used in the aspirated air mass estimation. Figure B.3(b) and Figure B.4(b) show that the estimated aspirated air mass converges towards its set point as well as the measured MAF data under steady-state conditions. We can see in Figure B.3(b) and Figure B.4(b) the slow adaptation in the intake pressure trajectory to compensate for the aspirated mass modeling errors. Figure B.3(c) and Figure B.4(c) give the observed volumetric efficiency error computed by the observer designed in Section B.4.1.

B.6 Conclusion

In this Appendix, the control strategy presented in Appendix A has been slightly modified to account for a mass air flow sensor that can be used in the engine set up. This additional sensor permits to give a feedback information in aspirated air mass control. An observer is proposed to compensate for the breathing modeling errors and is used in the pressure trajectory computation. Then the pressure controller design uses this information in the throttle control law. It complicates the theoretical convergence analysis because of the presence of an additional forcing term function of the observer convergence error. Finally, experimental results show convergence of the aspirated air mass toward MAF signal under steady-state conditions.

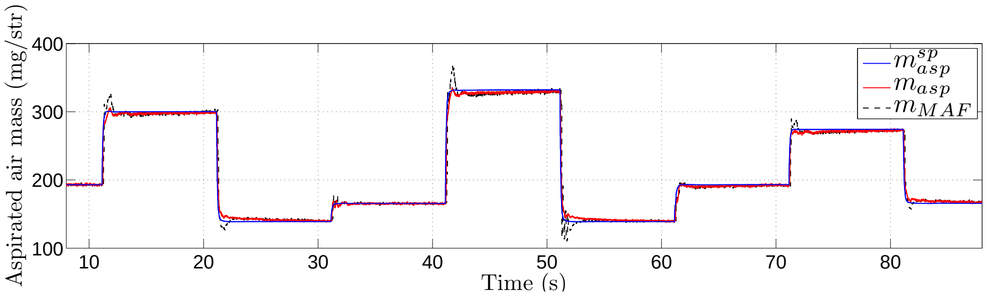

(a) Aspirated air mass

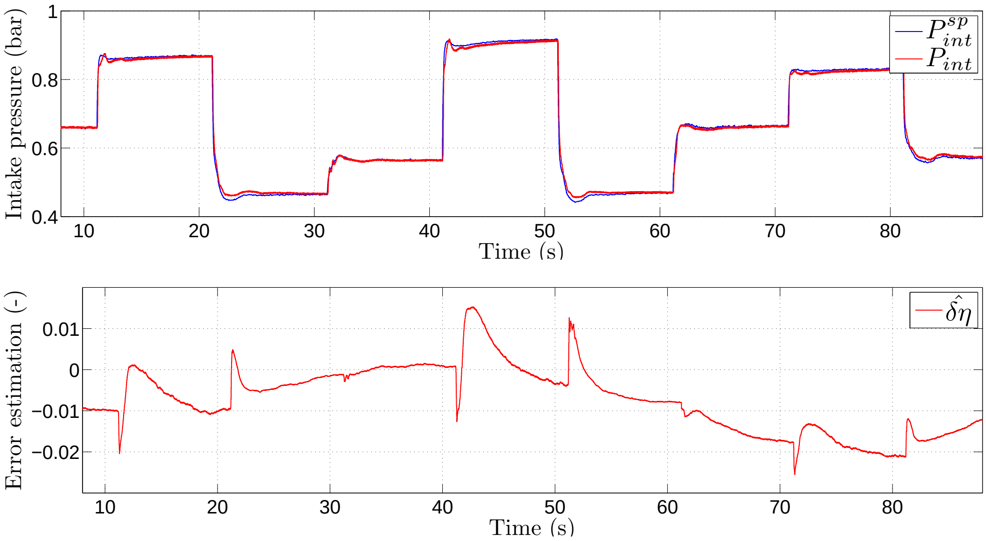

Figure B.3: Experimental results for a four-cylinder SI engine at constant engine speed (2000 rpm). Torque trajectory (Nm): $60 - 100 - 40 - 50 - 110 - 40 - 60 - 90 - 50$.

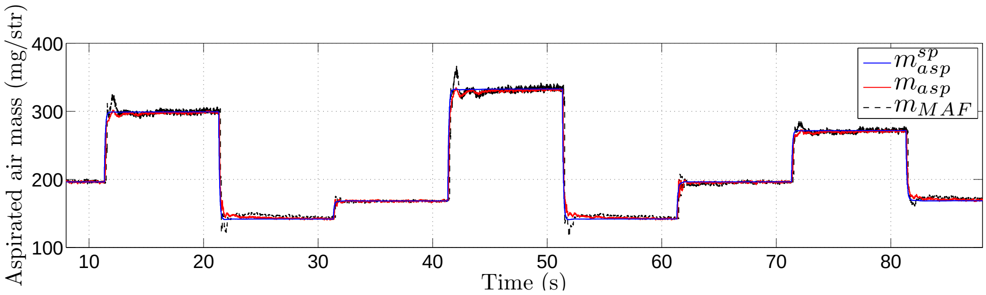

(a) Aspirated air mass

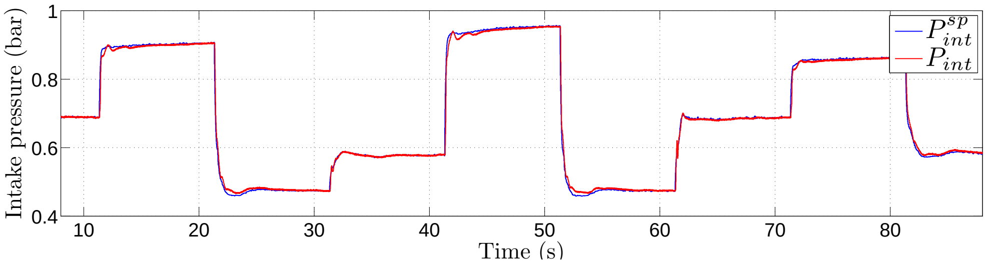

(b) Intake manifold pressure

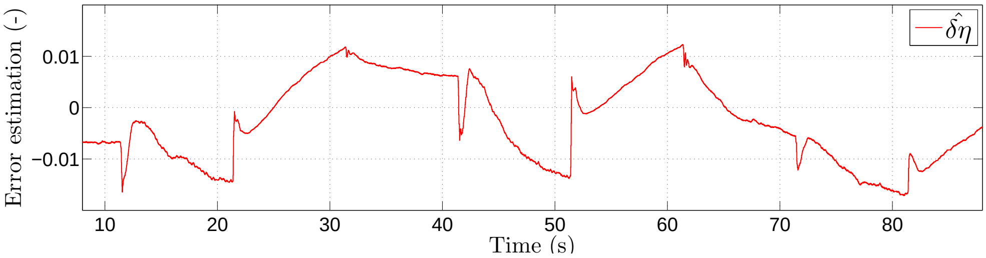

Figure B.4: Experimental results for a four-cylinder SI engine at constant engine speed (1500 rpm). Torque trajectory (Nm): $60 - 100 - 40 - 50 - 110 - 40 - 60 - 90 - 50$.

Appendix C

Air/Fuel Ratio controller for SI engines

C.1 Introduction

On SI engines, three-way catalysts (TWC) are used to reduce the pollutant emissions created by the combustion. This device located at the exhaust of the engine has three simultaneous tasks: reduction of NO_x, oxidation of CO and oxidation of unburned HC. These three reactions occur most efficiently when the catalytic converter receives exhaust from an engine running near from the stoichiometric point. This is about 14.6 parts air to 1 part fuel, by weight, for gasoline. Figure C.1 gives the catalyst efficiency according to the Air/Fuel Ratio (AFR)[1] . Within a narrow AFR band surrounding stoichiometry, conversion of all three pollutants is nearly complete. However, outside of that band, conversion efficiency falls off very rapidly. An accurate control of the AFR is then necessary [21, 36].

C.2 Existing control strategy

The AFR management classically consists of a feedback loop (from the oxygen sensor situated at the engine exhaust) [22, 81] associated with a feedforward term to limit AFR fluctuations during torque transients [11, 20]. The AFR controller acts upon the reference fuel mass which is sent to the injection system. The feedforward control law is designed according to a prediction of the air mass in the cylinders[2] (in [11],

---

[1] Noting m_{asp} and m_f the aspirated air mass and injected fuel mass, the AFR is defined by $\text{AFR} \triangleq \frac{1}{14.6}\frac{m_{asp}}{m_f}$.

[2] Noting m_f^{ff} and m_{asp}^{pred} the injection feedforward set point and the predicted aspirated air mass respectively, it follows $m_f^{ff} \triangleq \frac{1}{\text{AFR}_s} m_{asp}^{pred}$ where AFR_s is the stoichiometric AFR.

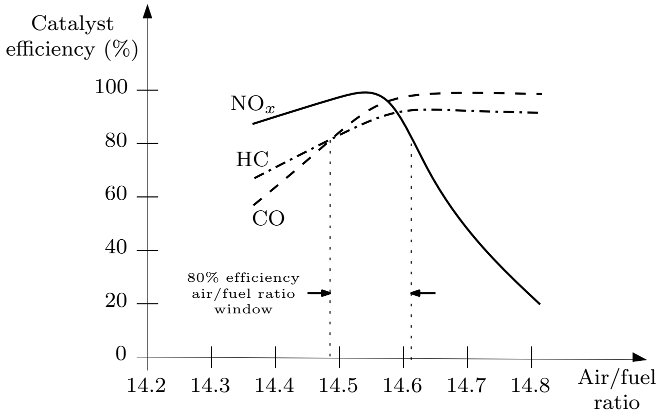

Figure C.1: Three-way catalytic converter efficiency.

the authors present a large study about injection delays in the AFR control loop that force using a prediction of the aspirated air mass). Such a control scheme is given in Figure C.2.

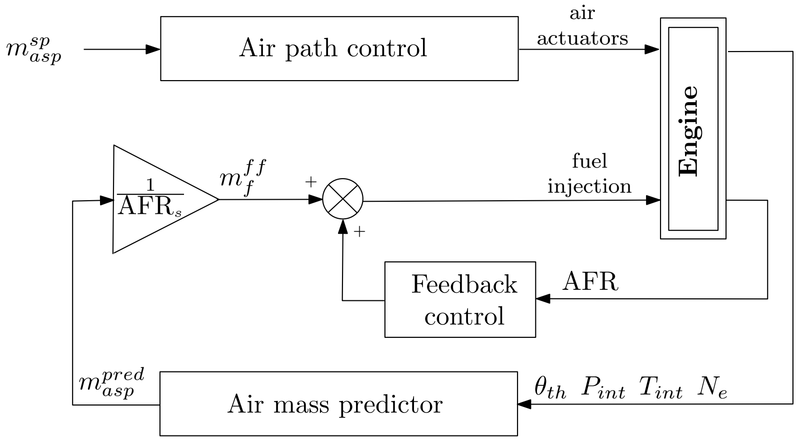
m_{asp}^{sp}
Air path control
air actuators
Engine
$\frac{1}{\text{AFR}_s}$
m_f^{ff}
+
+
fuel injection
Feedback control
AFR
m_{asp}^{pred}
Air mass predictor
θ_{th} P_{int} T_{int} N_e

Figure C.2: AFR classical control scheme. A prediction of the aspirated air mass is used to compute an injected fuel mass feedforward term. This term is completed by a feedback loop using the AFR measurement.

C.3 Proposed alternative control strategy

In the previous chapters, an accurate control of the aspirated air mass has been proposed, even in presence of disturbing VVT actuators. Provided a good aspirated air mass set point tracking, an alternative solution that deeply simplifies the AFR control strategy is proposed. Here, only the feedforward control term is focused on and no modification of the feedback term is made. Instead of computing a predicted aspirated air mass (which becomes complicated due to the multiplicity of the air path actuators), it is assumed that the reference signal for the aspirated air mass is tracked. The proposed control scheme is given in Figure C.3. The aspirated air mass set point is given for the feedforward fuel injection term computation. At the same time, this signal is delayed (to account for the previously discussed injection delays)[3] before entering in the air path control block.

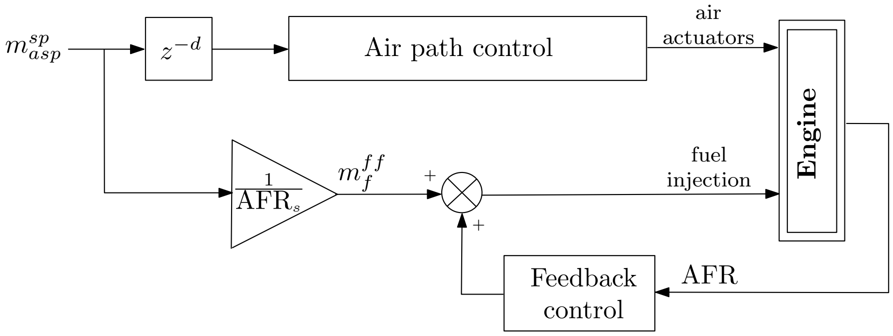

Figure C.3: AFR proposed control scheme.

C.4 Experimental results

The presented AFR control strategy have been test on experimental test bench and on vehicle. The engine under consideration is presented in Section 3.3.1.

C.4.1 Test bench results

The first experiment is about torque transients at constant engine speed (2000 rpm) at test bench. Here, the proposed strategy is validated and compared with a classical strategy. One use the name “strat” to denote the strategy presented above, and “ref” to denote the classical control strategy presented in [43]. This second strategy is based on an aspirated air mass prediction for AFR control. Figure C.4 presents the results for the torque response (Figure C.4(a)) and AFR management (Figure C.4(b)). AFR management is better with the proposed control strategy. Let $e \triangleq \mathrm{AFR}^{sp} - \mathrm{AFR}$ define the error between the stoichiometric AFR and the measured value, and consider the two performance metrics $\|e\|_2$ and $\|e\|_\infty$. Table C.1 compares the two controllers when used with the transients presented in Figure C.4. The good AFR control follows from the good aspirated air mass tracking (air path control details are given in Figure A.4).

---

[3] Notice that this delay introduced between the driver’s pedal command and the air path actuators is short enough to be imperceptive to the driver.

Performance metric	Classical AFR control	Proposed AFR control
	(“ref”)	(“strat”)
$\|e\|_2$	2.8731	1.3932
$\|e\|_\infty$	0.1882	0.0814

Table C.1: Comparison of controller performance.

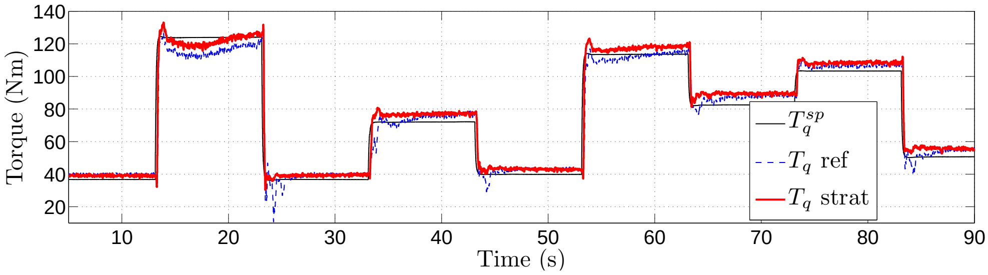

(a) Torque

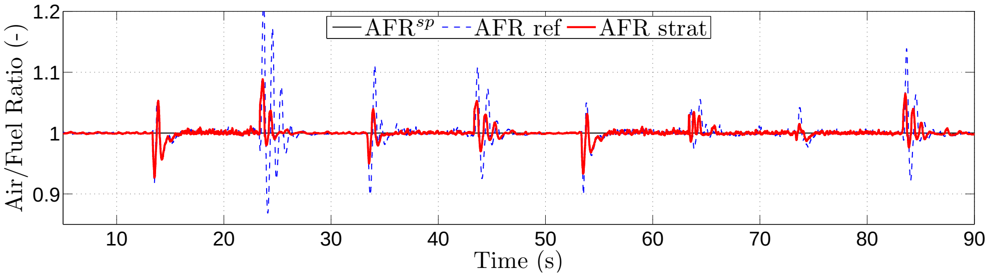

(b) Air/Fuel Ratio

Figure C.4: Experimental results for a four-cylinder SI engine at constant engine speed (2000 rpm). Comparison of torque and AFR control between two control strategies.

C.4.2 Vehicle results

The two following experiments follow from vehicle results. Figure C.5 and Figure C.6 are typical vehicle situations referring to gear change and take off respectively. In both figures are presented torque, aspirated air mass, intake manifold pressure and AFR tracking. First, a good tracking of the aspirated air mass is permitted by the coordinated control strategy presented in Chapter 3. The low-level intake manifold pressure controller behaves well because of the trajectory-tracking based strategy presented in Appendix A. Finally, for these reasons, the feedforward given to the AFR controller is good and then the AFR peaks are limited during transients. Note that the AFR set point change corresponds to a gear change.

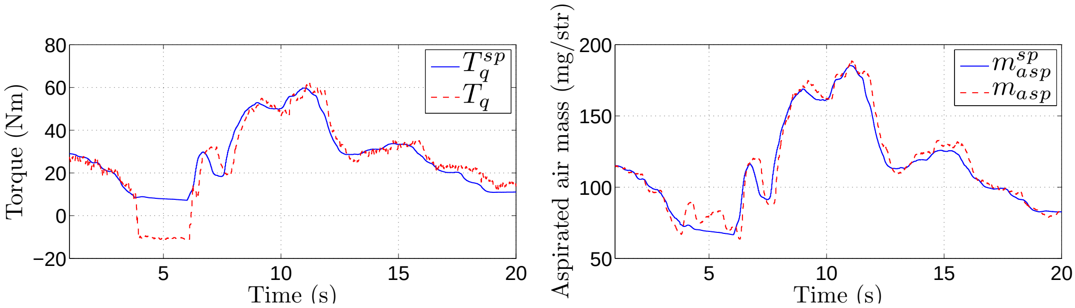

(a) Torque

(b) Aspirated air mass

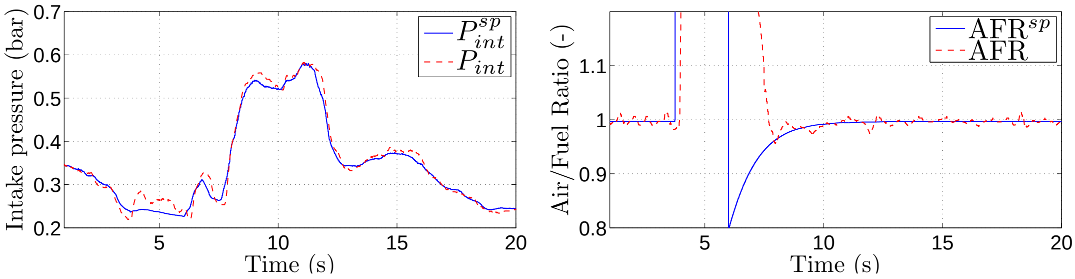

(c) Intake manifold pressure

(d) Air/Fuel Ratio

Figure C.5: Experimental results during a vehicle gear change. AFR controller succeeds in keeping the AFR near from the stoichiometric value.

C.5 Conclusion

An alternative AFR control strategy has been presented. It is proposed to give aspirated air mass set point instead of prediction to the injection feedforward control scheme. On top of simplifying the control scheme, it permits to increase robustness of the control strategy (by avoiding using measurements in the injection feedforward term). It is obvious that this AFR strategy works if the aspirated air mass controller well tracks its set point. Experimental results at test bench and on vehicle show good results of the strategy.

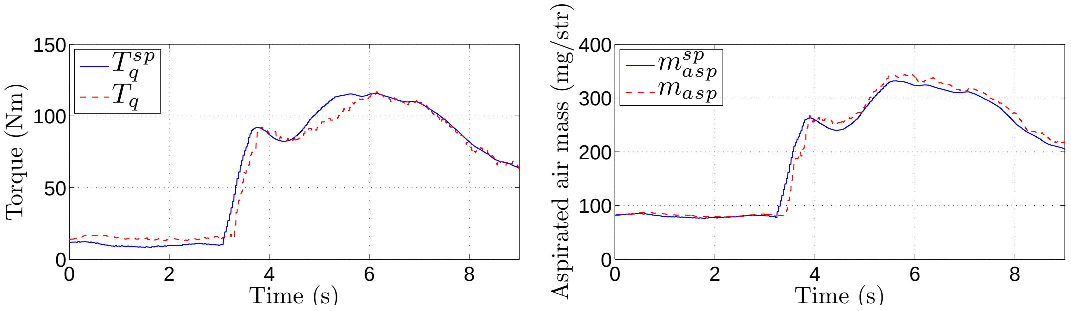

(a) Torque (b) Aspirated air mass

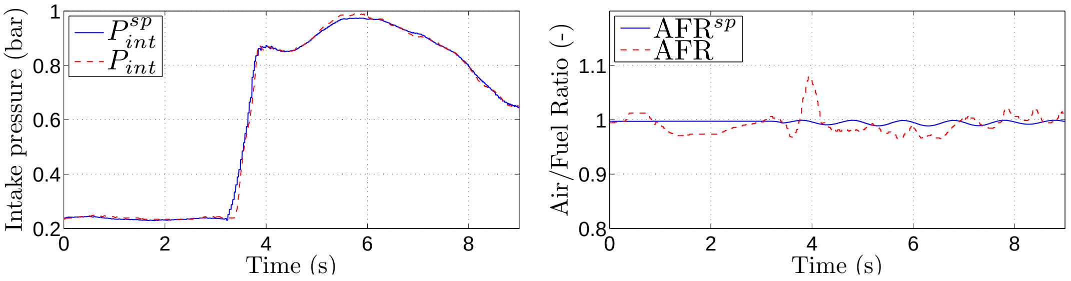

(c) Intake manifold pressure (d) Air/Fuel Ratio

Figure C.6: Experimental results during a vehicle take off. AFR controller succeeds in keeping the AFR near from the stoichiometric value.

Appendix D

Static positioning of the VVA actuators

D.1 Static positioning of the VVT actuators

Figure D.1(a) and Figure D.1(c) represent the look-up tables that give exhaust and intake VVT actuators positions on the whole engine operating range, respectively. Figure D.1(b) shows the impact of the exhaust and intake VVT actuators on the valves phasing. It shows that a large overlap is particularly used at part and high load in order to permit to trap burned gases and to scavenge fresh air respectively (as explained earlier). The overlap is reduced at low load to avoid combustion instabilities.

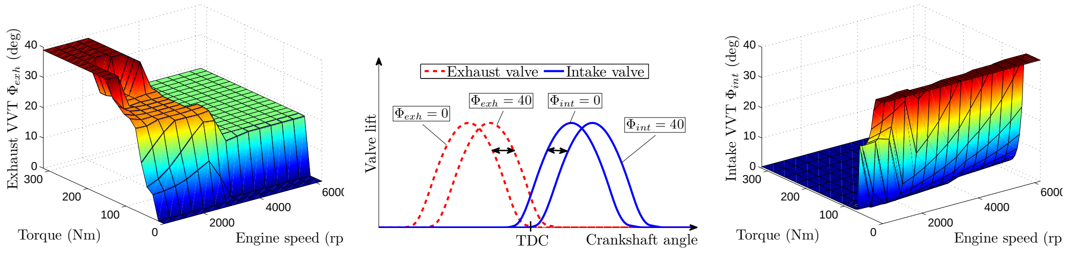

(a) Exhaust VVT look-up table.

(b) Intake and exhaust VVT actuators control the valves phasing.

(c) Intake VVT look-up table.

Figure D.1: Static positioning of the VVT actuators (Φ_{int} and Φ_{exh} stand for intake and exhaust actuators respectively) as functions of the engine operating points.

D.2 Static positioning of the VLD actuator

Figure D.2(a) represents the look-up table that gives the VLD actuator position on the whole engine operating range. Figure D.2(b) shows the impact of the VLD actuator on the second exhaust valve lift. It clearly appears that the second valve lift is particularly used ($\Phi_{vva} > 0$) at low and partial load to compensate for too low exhaust temperatures obtained with only external EGR.

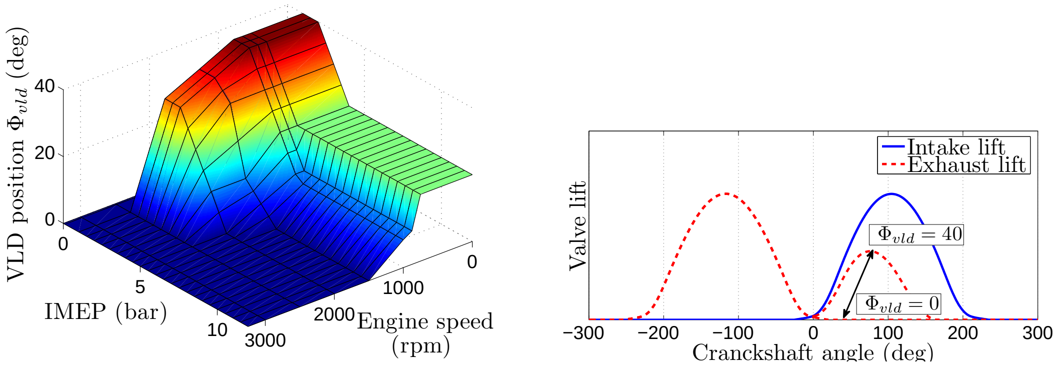

(a) Look-up table giving VLD actuator position in regards to the engine operating point.

(b) VLD actuator controls the exhaust valve lift re-opening.

Figure D.2: Static positioning of the VLD actuator (Φ_{vld} stands for the VLD position) in regards to the engine operating points.

Appendix E

Publications

E.1 Conference papers

[56] T. Leroy, J. Chauvin, N. Petit, and G. Corde. Motion planning control of the airpath of an SI engine with valve timing actuators. In *Proc. of International Federation of Automatic Control (IFAC) Symposium on Advances in Automotive Control*, volume 5, 2007

[48] T. Leroy, J. Chauvin, F. Le Berr, A. Duparchy, and G. Alix. Modeling fresh air charge and residual gas fraction on a dual independant variable valve timing SI engine. In *Proc. of the Society of Automotive Engineering World Congress*, number 2008-01-0983, 2008

[50] T. Leroy, J. Chauvin, and N. Petit. Airpath control of a SI engine with variable valve timing actuators. In *Proc. of the American Control Conference*, 2008

[51] T. Leroy, J. Chauvin, and N. Petit. Controlling air and burned gas masses of turbocharged VVT SI engines. In *Proc. of the 47th IEEE Conference on Decision and Control*, 2008

[46] T. Leroy, M. Bitauld, J. Chauvin, and N. Petit. In-cylinder burned gas rate estimation and control on VVA Diesel engines. In *Proc. of the Society of Automotive Engineering World Congress*, number 2009-01-0366, 2009

[52] T. Leroy, J. Chauvin, and N. Petit. Controlling in-cylinder composition on turbocharged variable-valve-timing spark ignition engines. In *Proc. of the European Control Conference*, 2009

[55] T. Leroy, J. Chauvin, and N. Petit. Transient burned gas rate control on VVA equipped Diesel engines. In *Proc. of International Federation of Automatic Control (IFAC) Symposium on Advances in Automotive Control*, 2010, Submitted

E.2 Journal contributions

[49] T. Leroy, J. Chauvin, F. Le Berr, A. Duparchy, and G. Alix. Modeling fresh air charge and residual gas fraction on a dual independant variable valve timing SI engine. *SAE International Journal of Engines*, 1(1):627–635, 2009

[53] T. Leroy, J. Chauvin, and N. Petit. Motion planning for experimental air path control of a variable-valve-timing spark ignition engine. *Control Engineering Practice*, 17(12):1432–1439, 2009

[54] T. Leroy, J. Chauvin, and N. Petit. Coordinated transient control of turbocharged variable-valve-timing spark-ignition engines. *IEEE Transactions on Control Systems Technology*, 2009, Submitted

E.3 Patent

[47] T. Leroy and J. Chauvin. Procédé pour contrôler la masse de gaz enfermée dans un cylindre d'un moteur essence à distribution variable. Patent EN. 09/00264, 2009

Bibliography

[1] *Automotive Engineering International Magazine*, 99(10), 1991.

[2] A. Albrecht, O. Grondin, J. Schmitt, L. Malbec, B. Youssef, G. Font, P. Gautier, and P. Moulin. Simulation support for control issues in the context of modern Diesel air path systems. *Oil & Gas Science and Technology*, 64(3):381–405, 2008.

[3] P. Andersson and L. Eriksson. Air-to-cylinder observer on a turbocharged SI-engine with wastegate. In *Proc. of the Society of Automotive Engineering World Congress*, number 2001-01-0262, 2001.

[4] T. Asmus. Perspectives on applications of variable valve timing. In *Proc. of the Society of Automotive Engineering World Congress*, number 910445, 1991.

[5] G. Bression, P. Pacaud, D. Soleri, J. Cessou, D. Azoulay, N. Lawrence, L. Doradoux, and N. Guerrassi. Comparative study in LTC combustion between a short HP EGR loop without cooler and a variable lift and duration system. In *17th Aachen Colloquium*, 2008.

[6] N. Cavina, C. Siviero, and R. Suglia. Residual gas fraction estimation: Application to a GDI engine with variable valve timing and EGR. *SAE Transactions*, 113(4):1774–1782, 2004.

[7] J. Chauvin, G. Corde, N. Petit, and P. Rouchon. Motion planning for experimental airpath control of a Diesel homogeneous charge-compression ignition engine. *Control Engineering Practice*, 16:1081–1091, 2008.

[8] J. Chauvin and N. Petit. Experimental control of variable cam timing actuators. In *Proc. of International Federation of Automatic Control (IFAC) Symposium on Advances in Automotive Control*, volume 5, 2007.

[9] J. Chauvin, N. Petit, P. Rouchon, G. Corde, and C. Vigild. Air path estimation on Diesel HCCI engine. In *Proc. of the Society of Automotive Engineering World Congress*, number 2006-01-1085, 2006.

[10] A. Chevalier, M. Müller, and E. Hendricks. On the validity of mean value engine models during transient operation. In *Proc. of the Society of Automotive Engineering World Congress*, number 2000-01-1261, 2000.

[11] A. Chevalier, C. Vigild, and E. Hendricks. Predicting the port air mass flow of SI engines in air/fuel ratio control applications. In *Proc. of the Society of Automotive Engineering World Congress*, number 2000-01-0260, 2000.

[12] C. Chiang, A. Stefanopoulou, and M. Jankovic. Nonlinear observer-based control of load transitions in homogeneous charge compression ignition engines. *IEEE Transactions on Control Systems Technology*, 15(3):403–598, 2007.

[13] G. Colin, G. Bloch, Y. Chamaillard, and F. Anstett. Two air path observers for turbocharged SI engines with VCT. *Control Engineering Practice*, 17(5):571–578, 2009.

[14] G. Colin, Y. Chamaillard, G. Bloch, and G. Corde. Neural control of fast nonlinear systems-application to a turbocharged SI engine with VCT. *IEEE Transactions on Neural Networks*, 18(4):1101–1114, 2007.

[15] L. Eriksson and I. Andersson. An analytic model for cylinder pressure in a four-stroke SI engine. *SAE Transactions*, 111(3):726–733, 2002.

[16] L. Eriksson, L. Nielsen, J. Brugård, J. Bergström, F. Pettersson, and P. Andersson. Modeling of a turbocharged SI engine. *Annual Reviews in Control*, 26(1):129–137, 2002.

[17] J. Fox, W. Cheng, and J. Heywood. A model for predicting residual gas fraction in spark-ignition engines. In *Proc. of the Society of Automotive Engineering World Congress*, number 931025, 1993.

[18] A. Genç, K. Glover, and R. Ford. Nonlinear control of hydraulic actuators in variable cam timing engines. In *International IFAC Workshop on Modeling, Emissions and Control in Automotive Engines*, 2001.

[19] C. Gray. A review of variable engine valve timing. *SAE Transactions*, 97(6):631–641, 1989.

[20] J. Grizzle, J. Cook, and W. Milam. Improved cylinder air charge estimation for transient air fuel ratio control. In *Proc. of the American Control Conference*, volume 2, pages 1568–1573, 1994.

[21] L. Guzzella and C. Onder. *Introduction to Modeling and Control of Internal Combustion Engine Systems.* Springer, 2004.

[22] L. Guzzella, M. Simons, and H. Geering. Feedback linearizing air/fuel-ratio controller. *Control Engineering Practice*, 5(8):1101–1105, 1997.

[23] K. Hatano, K. Iida, H. Higashi, and S. Murata. Development of a new multi-mode variable valve timing engine. In *Proc. of the Society of Automotive Engineering World Congress*, number 930878, 1993.

[24] J. Heywood. *Internal Combustion Engine Fundamentals.* McGraw-Hill, Inc, 1988.

[25] S. Hsieh, A. Stefanopoulou, J. Freudenberg, and K. Butts. Emission and drivability tradeoffs in a variable cam timing siengine with electronic throttle. In *Proc. of the American Control Conference*, volume 1, pages 284–288, 1997.

[26] M. Jankovic. Nonlinear control in automotive engine applications. In *Proc. of 15th International Symposium on Mathematical Theory of Networks and Systems*, 2002.

[27] M. Jankovic, F. Frischmuth, A. Stefanopoulou, and J. Cook. Torque management of engines with variable cam timing. *IEEE Control Systems*, 18(5):34–42, 1998.

[28] M. Jankovic and I. Kolmanovsky. Robust nonlinear controller for turbocharged Diesel engines. In *Proc. of the American Control Conference*, volume 3, pages 1389–1394, 1998.

[29] M. Jankovic and S. Magner. Cylinder air-charge estimation for advanced intake valve operation in variable cam timing engines. *JSAE Review*, 22(4):445–452, 2001.

[30] M. Jankovic, S. Magner, S. Hsieh, and J. Konesol. Transient effects and torque control of engines with variable cam timing. In *Proc. of the American Control Conference*, volume 1, pages 50–54, 2000.

[31] Z. Jiang and Y. Wang. Input-to-state stability for discrete-time nonlinear systems. *Automatica*, 37(6):857–869, 2001.

[32] Z.-P. Jiang, A. Teel, and L. Praly. Small-gain theorem for ISS systems and applications. *Mathematics of Control, Signals and Systems*, 7(2):95–120, 1994.

[33] A. Karnik, J. Buckland, J. Freudenberg, et al. Electronic throttle and wastegate control for turbocharged gasoline engines. In *Proc. of the American Control Conference*, volume 7, pages 4434–4439, 2005.

[34] H. Khalil. *Nonlinear Systems, third edition.* Prentice-Hall, Inc., 1992.

[35] D. Khiar, J. Lauber, T. Floquet, G. Colin, T. Guerra, and Y. Chamaillard. Robust takagi–sugeno fuzzy control of a spark ignition engine. *Control Engineering Practice*, 15(12):1446–1456, 2007.

[36] U. Kiencke and L. Nielsen. *Automotive Control Systems.* Springer, 2001.

[37] H. Kleeberg, D. Tomazic, O. Lang, and K. Habermann. Future potential and development methods for high output turbocharged direct injected gasoline engines. In *Proc. of the Society of Automotive Engineering World Congress*, number 2006-01-0046, 2006.

[38] P. Kreuter, P. Heuser, J. Reinicke-Murmann, R. Erz, U. Peter, and O. B "ocker. Variable valve actuation: Switchable and continuously variable valve lifts. *SAE Transactions*, 112(3):112–123, 2003.

[39] N. Ladommatos, S. Abdelhalim, H. Zhao, and Z. Hu. The dilution, chemical, and thermal effects of exhaust gas recirculation on Diesel engine emissions - Part 3. Effects of water vapour. *SP - Society of Automotive Engineers*, 1275:221–232, 1997.

[40] T. Lancefield, N. Lawrence, A. Ahmed, and H. Ben Hadj Hamouda. VLD a flexible, modular cam operated VVA system giving variable valve lift and duration and controlled secondary valve openings. In *SIA-IFP*, 2006.

[41] O. Lang, J. Geiger, K. Habermann, and M. Wittler. Boosting and direct injection - synergies for future gasoline engines. In *Proc. of the Society of Automotive Engineering World Congress*, number 2005-01-1144, 2005.

[42] F. Le Berr, M. Miche, G. Le Solliec, F.-A. Lafossas, and G. Colin. Modelling of a turbocharged SI engine with variable camshaft timing for engine control purposes. In *Proc. of the Society of Automotive Engineering World Congress*, number 2006-01-3264, 2006.

[43] G. Le Solliec, F. Le Berr, G. Colin, G. Corde, and Y. Chamaillard. Engine control of a downsized spark ignited engine: from simulation to vehicle. *Oil & Gas Science and Technology*, 62(4):555–572, 2007.

[44] B. Lecointe and G. Monnier. Downsizing a gasoline engine using turbocharging with direct injection. In *Proc. of the Society of Automotive Engineering World Congress*, number 2003-01-0542, 2003.

[45] T. Leone, E. Christenson, and R. Stein. Comparison of variable camshaft timing strategies at part load. *SAE Transactions*, 105(3):664–682, 1996.

[46] T. Leroy, M. Bitauld, J. Chauvin, and N. Petit. In-cylinder burned gas rate estimation and control on VVA Diesel engines. In *Proc. of the Society of Automotive Engineering World Congress*, number 2009-01-0366, 2009.

[47] T. Leroy and J. Chauvin. Procédé pour contrôler la masse de gaz enfermée dans un cylindre d'un moteur essence à distribution variable. Patent EN. 09/00264, 2009.

[48] T. Leroy, J. Chauvin, F. Le Berr, A. Duparchy, and G. Alix. Modeling fresh air charge and residual gas fraction on a dual independant variable valve timing SI engine. In *Proc. of the Society of Automotive Engineering World Congress*, number 2008-01-0983, 2008.

[49] T. Leroy, J. Chauvin, F. Le Berr, A. Duparchy, and G. Alix. Modeling fresh air charge and residual gas fraction on a dual independant variable valve timing SI engine. *SAE International Journal of Engines*, 1(1):627–635, 2009.

[50] T. Leroy, J. Chauvin, and N. Petit. Airpath control of a SI engine with variable valve timing actuators. In *Proc. of the American Control Conference*, 2008.

[51] T. Leroy, J. Chauvin, and N. Petit. Controlling air and burned gas masses of turbocharged VVT SI engines. In *Proc. of the 47th IEEE Conference on Decision and Control*, 2008.

[52] T. Leroy, J. Chauvin, and N. Petit. Controlling in-cylinder composition on turbocharged variable-valve-timing spark ignition engines. In *Proc. of the European Control Conference*, 2009.

[53] T. Leroy, J. Chauvin, and N. Petit. Motion planning for experimental air path control of a variable-valve-timing spark ignition engine. *Control Engineering Practice*, 17(12):1432–1439, 2009.

[54] T. Leroy, J. Chauvin, and N. Petit. Coordinated transient control of turbocharged variable-valve-timing spark-ignition engines. *IEEE Transactions on Control Systems Technology*, 2009, Submitted.

[55] T. Leroy, J. Chauvin, and N. Petit. Transient burned gas rate control on VVA equipped Diesel engines. In *Proc. of International Federation of Automatic Control (IFAC) Symposium on Advances in Automotive Control*, 2010, Submitted.

[56] T. Leroy, J. Chauvin, N. Petit, and G. Corde. Motion planning control of the airpath of an SI engine with valve timing actuators. In *Proc. of International Federation of Automatic Control (IFAC) Symposium on Advances in Automotive Control*, volume 5, 2007.

[57] A. Loría and E. Panteley. Uniform exponential stability of linear time-varying systems : revisited. *Systems & Control Letters*, 47(1):13–24, 2002.

[58] X. Lü, W. Chen, and Z. Huang. A fundamental study on the control of the HCCI combustion and emissions by fuel design concept combined with controllable EGR. Part 1. The basic characteristics of HCCI combustion. *Fuel*, 84(9):1074–1083, 2005.

[59] M. Mladek and C. Onder. A model for the estimation of inducted air mass and the residual gas fraction using cylinder pressure measurements. In *Proc. of the Society of Automotive Engineering World Congress*, number 2000-01-0958, 2000.

[60] P. Moulin and J. Chauvin. Modelling and control of the air system of a turbocharged gasoline engine. *Control Engineering Practice*, 2009, doi:10.1016/j.conengprac.2009.11.006.

[61] T. Nogi, T. Shiraishi, M. Oshuga, Y. Nagayama, and N. Tokuyasu. Internal combustion engine and control apparatus and method thereof. Patent US 2005/0034706, 2005.

[62] P. Öberg and L. Eriksson. Control oriented gas exchange models for CVCP engines and their transient sensitivity. *Oil & Gas Science and Technology*, 62(4):573–584, 2007.

[63] D. Petitjean, L. Bernardini, C. Middlemass, and S. Shahed. Advanced gasoline engine turbocharging technology for fuel economy improvements. *SAE Transactions*, 113(4):521–529, 2004.

[64] F. Ponti, J. Pianai, and R. Suglia. Residual gas model for on-line estimation for inlet and exhaust continous VVT engine configuration. In *IFAC World Congress*, 2004.

[65] A. Ranini and G. Monnier. Turbocharging a gasoline direct injection engine. In *Proc. of the Society of Automotive Engineering World Congress*, number 2001-01-0736, 2001.

[66] V. Rauch, R. Nikoukhah, M. Sorine, and H. Jreij. Procédé de commande d'un moteur à combustion interne. Patent FR2790516 (B1), 1999.

[67] D. Rausen, A. Stefanopoulou, J. Kang, J. Eng, and T. Kuo. A mean-value model for control of homogeneous charge compression ignition (HCCI) engines. *Journal of Dynamic Systems, Measurement, and Control*, 127(3):355–367, 2005.

[68] H. Sandquist, J. Wallesten, K. Enwald, and S. Stromberg. Influence of valve overlap strategies on residual gas fraction and combustion in a spark-ignition engine at idle. In *Proc. of the Society of Automotive Engineering World Congress*, number 972936, 1997.

[69] D. Schwarzmann, R. Nitsche, and J. Lunze. Diesel boost pressure control using flatness-based internal model control. In *Proc. of the Society of Automotive Engineering World Congress*, number 2006-01-0855, 2006.

[70] L. Shi, Y. Cui, K. Deng, H. Peng, and Y. Chen. Study of low emission homogeneous charge compression ignition (HCCI) engine using combined internal and external exhaust gas recirculation (EGR). *Energy*, 31(14):2665–2676, 2006.

[71] H. Shimizu. Intake control apparatus for internal combustion engine and method thereof. Patent US 2005/0205055, 2005.

[72] E. Sontag. Input to state stability: Basic concepts and results. *Lecture notes in mathematics*, 1932:163–220, 2008.

[73] A. Stefanopoulou, A. Cook, J. Grizzle, and J. S. Freudenberg. Control-oriented model of a dual equal variable cam timing spark ignition engine. *Journal of dynamic systems, measurement, and control*, 120:257–266, 1998.

[74] A. Stefanopoulou and I. Kolmanovsky. Dynamic scheduling of internal exhaust gas recirculation systems. In *Proc. of the IMECE*, volume 61, pages 671–678, 1997.

[75] A. Stefanopoulou and I. Kolmanovsky. Analysis and control of transient torque response in engines with internal exhaust gas recirculation. *IEEE Transactions on Control Systems Technology*, 7(5):555–566, 1999.

[76] A. Stefanopoulou, I. Kolmanovsky, and J. Freudenberg. Control of variable geometry turbocharged Diesel engines for reduced emissions. *IEEE Transactions on Control Systems Technology*, 8:733–745, 2000.

[77] R. Stein, K. Galietti, and T. Leone. Dual equal VCT: a variable camshaft timing strategy for improved fuel economy and emissions. In *Proc. of the Society of Automotive Engineering World Congress*, number 950975, 1995.

[78] A. Stotsky and I. Kolmanovsky. Application of input estimation techniques to charge estimation and control in automotive engines. *Control Engineering Practice*, 10(12):1371–1383, 2002.

[79] H. Streib and B. H. Electronic throttle control (ETC): A cost effective system for improved emissions, fuel economy, and driveability. In *Proc. of the Society of Automotive Engineering World Congress*, number 960338, 1996.

[80] K. Takao and A. Masahiro. Valve timing control for engine. Patent EP 1 104 844 A2, 2001.

[81] T.-C. Tseng and W. Cheng. An adaptive air/fuel ratio controller for si engine throttle transients. In *Proc. of the Society of Automotive Engineering World Congress*, number 1999-01-0552, 1999.

[82] R. Turin, R. Zhang, and M. Chang. Volumetric efficiency model for variable camphasing and variable valve lift applications. In *Proc. of the Society of Automotive Engineering World Congress*, number 2008-01-0995, 2008.

[83] M. Van Nieuwstadt, I. Kolmanovsky, P. Moraal, A. Stefanopoulou, and M. Jankovic. Experimental comparison of EGR-VGT control schemes for a high speed Diesel engine. *Control System Magazine*, 20:63–79, 2000.

[84] J. Wang. Air fraction estimation for multiple combustion mode Diesel engines with dual-loop EGR systems. *Control Engineering Practice*, 16(12):1479–1486, 2008.

[85] B. Wu, Z. Filipi, D. Assanis, D. Kramer, G. Ohl, M. Prucka, and E. DiValentin. Using artificial neural networks for representing the air flow rate through a 2.4 liter VVT engine. In *Proc. of the Society of Automotive Engineering World Congress*, number 2004-01-3054, 2004.

Contrôle du Remplissage des Moteurs à Combustion Interne équipés de Systèmes de Distribution Variable

RÉSUMÉ :

Nous étudions la production de couple et de polluants de moteurs à combustion interne à distribution variable d'un type fréquemment répandu dans l'industrie automobile (moteurs Diesel ou essence). Les systèmes de distribution variable (VVA pour Variable Valve Actuation) ont été introduits dans les moteurs pour optimiser l'efficacité du fonctionnement global sur des plages très larges de points de fonctionnement, considérés à l'équilibre.

A tout instant, les résultats de la combustion dépendent du remplissage en air/gaz brûlés du cylindre, qui lui même dépend de la position des actionneurs VVA et des conditions dans le collecteur d'admission. Ces deux sous-systèmes ont des temps de réponse différents, ce qui conduit, pendant les transitoires, à des pertes d'efficacité du moteur. Dans cette thèse, nous proposons une solution a ce problème, qui prend la forme de boucle de coordination entre les sous-systèmes de contrôle de bas-niveau. Cette coordination s'effectue par l'intermédiaire d'un modèle de remplissage développé dans ce manuscrit. Des résultats expérimentaux établissent qu'il est possible d'améliorer la production de couple et de réduire les polluants.

Mots clés : Moteur à combustion interne, Distribution variable, Contrôle moteur, Remplissage, Coordination dynamique

Cylinder Filling Control of Variable-Valve-Actuation equipped Internal Combustion Engines

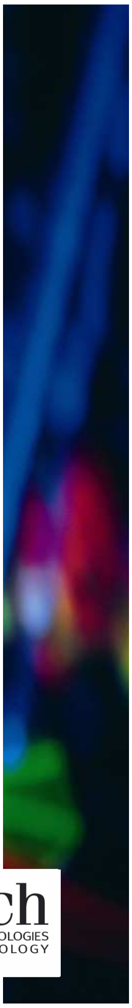

ABSTRACT :

The production of torque and pollutants of Variable Valve Actuation equipped internal combustion engines found in the automotive industry (both Diesel and gasoline engines) is studied. Variable Valve Actuation (VVA) is a technology which has been introduced to optimize engine efficiency at steady-states covering a wide range of operating conditions.

In more details, the outcome of the internal combustion engine (torque and pollutant) depends on the cylinder filling at each stroke which, itself, depends on the VVA positions and the engine intake manifold conditions. These two subsystems have inconsistent response times which results in efficiency losses during transient operations. In this manuscript, a remedy for this issue which takes the form of coordination loops of low-level controllers is proposed. This coordination uses a cylinder filling model, designed in the thesis. Experimental results prove that torque production and pollutant emissions can be improved.

Keywords : Internal combustion engine, Variable Valve Actuation, Engine control, Cylinder filling, Dynamical Coordination

MINES ParisTech

ParisTech
INSTITUT DES SCIENCES ET TECHNOLOGIES
PARIS INSTITUTE OF TECHNOLOGY